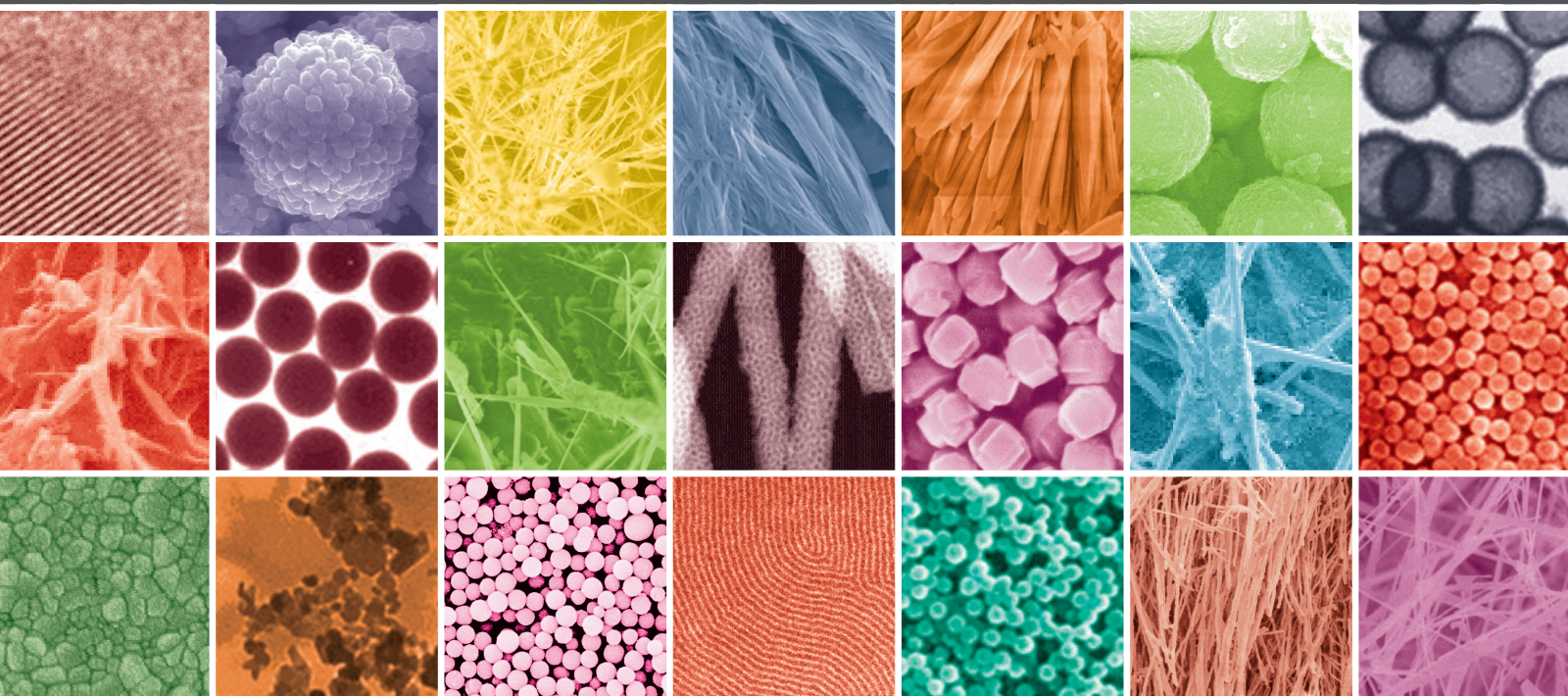


# Advanced Green Energy Nanomaterials for Optoelectronic Devices: Synthesis, Processing, Characterization, and Applications

Guest Editors: Wei-Chun Chen, Shou-Yi Kuo, Ying-Lung Daniel Ho,  
Kaushik Balakrishnan, and Wei-Heng Shih



---

# **Advanced Green Energy Nanomaterials for Optoelectronic Devices: Synthesis, Processing, Characterization, and Applications**

## **Advanced Green Energy Nanomaterials for Optoelectronic Devices: Synthesis, Processing, Characterization, and Applications**

Guest Editors: Wei-Chun Chen, Shou-Yi Kuo,  
Ying-Lung Daniel Ho, Kaushik Balakrishnan,  
and Wei-Heng Shih



Copyright © 2016 Hindawi Publishing Corporation. All rights reserved.

This is a special issue published in "Journal of Nanomaterials." All articles are open access articles distributed under the Creative Commons Attribution License, which permits unrestricted use, distribution, and reproduction in any medium, provided the original work is properly cited.

## Editorial Board

Domenico Acierno, Italy	Ovidiu Ersen, France	Ed Ma, USA
Katerina Aifantis, USA	Claude Estournès, France	Laura M. Maestro, Spain
Nageh K. Allam, USA	Andrea Falqui, KSA	Gaurav Mago, USA
Margarida Amaral, Portugal	Matteo Ferroni, Italy	Muhamamd A. Malik, UK
Martin Andersson, Sweden	Ilaria Fratoddi, Italy	Devanesan Mangalaraj, India
Raul Arenal, Spain	Alan Fuchs, USA	Sanjay R. Mathur, Germany
Ilaria Armentano, Italy	Miguel A. Garcia, Spain	Tony McNally, UK
Vincenzo Baglio, Italy	Siddhartha Ghosh, Singapore	Yogendra Mishra, Germany
Lavinia Balan, France	P. K. Giri, India	Paulo Cesar Morais, Brazil
Thierry Baron, France	Russell E. Gorga, USA	Paul Munroe, Australia
Andrew R. Barron, USA	Jihua Gou, USA	Jae-Min Myoung, Republic of Korea
Hongbin Bei, USA	Jean M. Greeneche, France	Rajesh R. Naik, USA
Daniel Bellet, France	Smrati Gupta, Germany	Albert Nasibulin, Russia
Stefano Bellucci, Italy	Kimberly Hamad-Schifferli, USA	Toshiaki Natsuki, Japan
Enrico Bergamaschi, Italy	Simo-Pekka Hannula, Finland	Koichi Niihara, Japan
Samuel Bernard, France	Michael Harris, USA	Natalia Noginova, USA
D. Bhattacharyya, New Zealand	Yasuhiko Hayashi, Japan	Sherine Obare, USA
Sergio Bietti, Italy	F. Hernandez-Ramirez, Spain	Won-Chun Oh, Republic of Korea
Giovanni Bongiovanni, Italy	Michael Z. Hu, USA	Atsuto Okamoto, Japan
Theodorian Borca-Tasciuc, USA	Nay Ming Huang, Malaysia	Abdelwahab Omri, Canada
Mohamed Bououdina, Bahrain	Shaoming Huang, China	Ungyu Paik, Republic of Korea
Torsten Brezesinski, Germany	Zafar Iqbal, USA	Piersandro Pallavicini, Italy
C. Jeffrey Brinker, USA	Balachandran Jeyadevan, Japan	Edward A. Payzant, USA
Christian Brosseau, France	Xin Jiang, Germany	Alessandro Pegoretti, Italy
Philippe Caroff, Australia	Rakesh Joshi, Australia	Ton Peijs, UK
Victor M. Castaño, Mexico	Jeong-won Kang, Republic of Korea	Oscar Perales-Pérez, Puerto Rico
Albano Cavaleiro, Portugal	Hassan Karimi-Maleh, Iran	Jorge Pérez-Juste, Spain
Bhanu P. S. Chauhan, USA	Antonios Kelarakis, UK	Alexey P. Popov, Finland
Shafiq Chowdhury, USA	Alireza Khataee, Iran	Philip D. Rack, USA
Jin-Ho Choy, Republic of Korea	Ali Khorsand Zak, Iran	Peter Reiss, France
Kwang-Leong Choy, UK	Philippe Knauth, France	Orlando Rojas, USA
Yu-Lun Chueh, Taiwan	Ralph Krupke, Germany	Marco Rossi, Italy
Elisabetta Comini, Italy	Christian Kübel, Germany	Ilker S. Bayer, Italy
Giuseppe Compagnini, Italy	Prashant Kumar, UK	Cengiz S. Ozkan, USA
David Cornu, France	Eric Le Bourhis, France	Sudipta Seal, USA
Miguel Correa-Duarte, Spain	Jun Li, Singapore	Shu Seki, Japan
P. Davide Cozzoli, Italy	Meiyong Liao, Japan	Vladimir Šepelák, Germany
Shadi A. Dayeh, USA	Shijun Liao, China	Huaiyu Shao, Japan
Luca Deseri, USA	Silvia Licoccia, Italy	Prashant Sharma, USA
Yong Ding, USA	Wei Lin, USA	Donglu Shi, USA
Philippe Dubois, Belgium	Nathan C. Lindquist, USA	Bhanu P. Singh, India
Zehra Durmus, Turkey	Zainovia Lockman, Malaysia	Surinder Singh, USA
Joydeep Dutta, Oman	Nico Lovergne, Italy	Vladimir Sivakov, Germany
Ali Eftekhari, USA	Jim Low, Australia	Adolfo Speghini, Italy
Samy El-Shall, USA	Jue Lu, USA	Marinella Striccoli, Italy

Xuping Sun, KSA	Tamer Uyar, Turkey	Ping Xiao, UK
Ashok K. Sundramoorthy, USA	Bala Vaidhyanathan, UK	Zhi Li Xiao, USA
Angelo Taglietti, Italy	Luca Valentini, Italy	Yangchuan Xing, USA
Bo Tan, Canada	Rajender S. Varma, USA	Doron Yadlovker, Israel
Leander Tapfer, Italy	Ester Vazquez, Spain	Yoke K. Yap, USA
Valeri P. Tolstoy, Russia	Ajayan Vinu, Australia	Kui Yu, Canada
Muhammet S. Toprak, Sweden	Ruibing Wang, Macau	William Yu, USA
R. Torrecillas, Spain	Shiren Wang, USA	Michele Zappalorto, Italy
Achim Trampert, Germany	Yong Wang, USA	Renyun Zhang, Sweden
Takuya Tsuzuki, Australia	Magnus Willander, Sweden	

## Contents

### **Advanced Green Energy Nanomaterials for Optoelectronic Devices: Synthesis, Processing, Characterization, and Applications**

Wei-Chun Chen, Shou-Yi Kuo, Ying-Lung Daniel Ho, Kaushik Balakrishnan, and Wei-Heng Shih  
Volume 2016, Article ID 3804765, 1 page

### **Effect of O<sub>2</sub>/Ar Gas Flow Ratios on Properties of Cathodic Vacuum Arc Deposited ZnO Thin Films on Polyethylene Terephthalate Substrate**

Chien-Wei Huang, Ru-Yuan Yang, Cheng-Tang Pan, and Min-Hang Weng  
Volume 2016, Article ID 6479812, 6 pages

### **Effect of Top-Region Area of Flat-Top Pyramid Patterned Sapphire Substrate on the Optoelectronic Performance of GaN-Based Light-Emitting Diodes**

Hsu-Hung Hsueh, Sin-Liang Ou, Yu-Che Peng, Chiao-Yang Cheng, Dong-Sing Wuu, and Ray-Hua Horng  
Volume 2016, Article ID 2701028, 8 pages

### **Characterization of Al-Doped ZnO Transparent Conducting Thin Film Prepared by Off-Axis Magnetron Sputtering**

Sin-Liang Ou, Feng-Min Lai, Lun-Wei Yuan, Da-Long Cheng, and Kuo-Sheng Kao  
Volume 2016, Article ID 6250640, 6 pages

### **Thermal Stresses Analysis and Optimized TTP Processes to Achieved CNT-Based Diaphragm for Thin Panel Speakers**

Feng-Min Lai and Chang-Yi Peng  
Volume 2016, Article ID 8243605, 10 pages

### **Structure and Properties of Nanocrystalline (TiZr)<sub>x</sub>N<sub>1-x</sub> Thin Films Deposited by DC Unbalanced Magnetron Sputtering**

Yu-Wei Lin, Chia-Wei Lu, Ge-Ping Yu, and Jia-Hong Huang  
Volume 2016, Article ID 2982184, 12 pages

## Editorial

# Advanced Green Energy Nanomaterials for Optoelectronic Devices: Synthesis, Processing, Characterization, and Applications

**Wei-Chun Chen,<sup>1</sup> Shou-Yi Kuo,<sup>2,3</sup> Ying-Lung Daniel Ho,<sup>4</sup>  
Kaushik Balakrishnan,<sup>5</sup> and Wei-Heng Shih<sup>6</sup>**

<sup>1</sup>Instrument Technology Research Center, National Applied Research Laboratories, Hsinchu City, Taiwan

<sup>2</sup>Department of Electronic Engineering, Chang Gung University, Taoyuan, Taiwan

<sup>3</sup>Department of Nuclear Medicine, Chang Gung Memorial Hospital, Taoyuan, Taiwan

<sup>4</sup>Department of Electrical and Electronic Engineering, University of Bristol, Bristol, UK

<sup>5</sup>College of Optical Sciences, University of Arizona, Tucson, AZ, USA

<sup>6</sup>Department of Materials Science and Engineering, Drexel University, Philadelphia, PA, USA

Correspondence should be addressed to Wei-Chun Chen; [weichun@narlabs.org.tw](mailto:weichun@narlabs.org.tw)

Received 1 September 2016; Accepted 1 September 2016

Copyright © 2016 Wei-Chun Chen et al. This is an open access article distributed under the Creative Commons Attribution License, which permits unrestricted use, distribution, and reproduction in any medium, provided the original work is properly cited.

Advanced green energy nanomaterials in the applied science fields have received increasing attentions because of their unique physical and chemical properties. Their dominant roles are established in our science and society and their applications penetrate into our daily life and the influence impact is significant. This special issue aims at identifying the current status and anticipating future directions in this emerging field via fusions of civil engineering, environmental science, chemistry, and materials science and antiecotoxic technologies. With the unique structures and novel properties of the nanomaterials, the applications cover a wide range of key components or products, such as light-emitting diodes (LED), solar cell devices, nanocomposites, optical materials, functional materials, and other related advanced nanomaterials.

Five research articles were accepted in this special issue, including papers on synthesis of functional nanomaterials and analysis, synthesis of nitride for LEDs, optimized TTP processes to CNT-based materials, and nanocrystalline nitrides growth. For synthesis of nanomaterials, the papers indicated that the properties of the nanocrystalline TiZrN thin films changed with nitrogen flow rate above 1.0 sccm because the films contained a stable single phase (TiZrN).

For thin films growth, the papers are about the thin films and their physical properties. One tried to describe how AZO

films can be used as the transparent conducting oxide thin films. In addition, ZnO thin films were deposited by CVAD at room temperature for flexible devices. For the optoelectronic performance of GaN-based light-emitting diodes devices, fabrication of FTP-PSSs is helpful in improving the crystal quality of GaN epilayer.

We hope that this special issue provides the readers with an overview of the recent progress achieved and the future developing directions in the advanced green energy nanomaterials synthesis technology. This special issue will be a valuable reference and a perspective for the research community working in this exciting field and can inspire more engineers and scientists.

Wei-Chun Chen  
Shou-Yi Kuo  
Ying-Lung Daniel Ho  
Kaushik Balakrishnan  
Wei-Heng Shih

## Research Article

# Effect of O<sub>2</sub>/Ar Gas Flow Ratios on Properties of Cathodic Vacuum Arc Deposited ZnO Thin Films on Polyethylene Terephthalate Substrate

Chien-Wei Huang,<sup>1</sup> Ru-Yuan Yang,<sup>2</sup> Cheng-Tang Pan,<sup>1</sup> and Min-Hang Weng<sup>3</sup>

<sup>1</sup>Department of Mechanical and Electron-Mechanical Engineering, National Sun Yat-Sen University, Kaohsiung 804, Taiwan

<sup>2</sup>Graduate Institute of Materials Engineering, National Pingtung University of Science and Technology, Pingtung County 912, Taiwan

<sup>3</sup>Medical Devices and Optoelectronics Equipment Department, Metal Industries Research & Development Center, Kaohsiung 821, Taiwan

Correspondence should be addressed to Ru-Yuan Yang; [ryyang@mail.npust.edu.tw](mailto:ryyang@mail.npust.edu.tw)

Received 30 March 2016; Revised 23 May 2016; Accepted 1 June 2016

Academic Editor: Ying-Lung D. Ho

Copyright © 2016 Chien-Wei Huang et al. This is an open access article distributed under the Creative Commons Attribution License, which permits unrestricted use, distribution, and reproduction in any medium, provided the original work is properly cited.

Cathodic vacuum arc deposition (CVAD) can obtain a good quality thin film with a low growth temperature and a high deposition rate, thus matching the requirement of film deposition on flexible electronics. This paper reported the room-temperature deposition of zinc oxide (ZnO) thin films deposited by CVAD on polyethylene terephthalate (PET) substrate. Microstructure, optical, and electrical measurements of the deposited ZnO thin films were investigated with various O<sub>2</sub>/Ar gas flow ratios from 6 : 1 to 10 : 1. The films showed hexagonal wurtzite crystal structure. With increasing the O<sub>2</sub>/Ar gas flow ratios, the *c*-axis (002) oriented intensity decreased. The crystal sizes were around 16.03 nm to 23.42 nm. The average transmittance values in the visible range of all deposited ZnO films were higher than 83% and the calculated band gaps from the absorption data were found to be around 3.1 to 3.2 eV. The resistivity had a minimum value in the  $3.65 \times 10^{-3}$  Ω·cm under the O<sub>2</sub>/Ar gas flow ratio of 8 : 1. The luminescence mechanisms of the deposited film were also investigated to understand the defect types of room-temperature grown ZnO films.

## 1. Introduction

During the last few decades, flexible electronics such as thin-film transistors, solar cells, and light-emitting diodes have been studied intensively owing to their advantages of light weight and low cost over present rigid electronics [1]. Transparent conductive oxide (TCO) thin film is usually an important role to obtain the required performances of such flexible electronic devices. Typically, indium tin oxide (ITO), tin dioxide (SnO<sub>2</sub>), and zinc oxide (ZnO) are most popular transparent conductive thin films [2]. Moreover, the high polymer flexible substrate, such as polyethylene terephthalate (PET), polycarbonate (PC), polyethersulfone (PES), polyethylene naphthalate (PEN), or polyimide (PI) [3–5] are commonly used for the above flexible applications. However, deposition of such TCO films on the plastic substrates requires a low-temperature technique since most of polymer substrates

could not be used above 200°C. Thus, low temperature deposition becomes the most important issue for growing high quality TCO films on flexible polymer substrates [1].

In the past, many techniques were used to obtain high quality TCO thin film, such as physical vapor deposition and chemical vapor deposition [6]. In the above techniques, cathodic vacuum arc deposition (CVAD) method has many advantages, such as high degree of ionization in the plasma (80~100%) and high ion energy (50~150 eV) [7–13]. Therefore it can achieve good quality dense coating with a low growth temperature and a high deposition rate (~10 nm/s) [9]. In addition, ZnO film is a well-known II–VI compound semiconducting material with excellent optical, electrical, and piezoelectric properties [2]. Moreover, ZnO film has some advantages such as nontoxicity, wide band gap (3.3 eV), high thermal energy at 300 K (26 meV), and an excitation binding energy of 60 meV. ZnO has a high transmittance in the visible

spectrum and a low electrical resistivity under the relative low-temperature deposition [1]. Therefore, it is desired to grow high quality ZnO film on plastic substrate at a low temperature using CVAD system. The deposition parameters of CVAD technology typically include gas flow ratio, substrate temperature, arc current, and bias voltage [9, 10]. In previous works, ZnO films were successfully deposited onto PET substrates using CVAD technique. Effect of various arc currents (40, 45, 50, and 55 A) [11] and effect of film thicknesses (150, 250, 350, 450, and 550 nm) [12] on microstructure, optical, and electrical properties were investigated. It is known that the oxygen flow rate plays an important role in the properties of the grown ZnO films under different physical vapor deposition, especially in the electrical property of pure ZnO film, since the oxygen flow rate normally affects the defect types of pure ZnO films deposited at a low temperature. However, there is no report regarding the issue.

In this paper, we reported a detailed investigation on the effects of various O<sub>2</sub>/Ar gas flow ratios on properties of pure ZnO films deposited by using CVAD on the PET substrate at a room temperature and investigated the relation between the microstructure, optical, and electrical properties by using X-ray diffraction (XRD), ultraviolet-visible spectroscopy (UV-VIS), Hall measurement, a four-point probe, and photoluminescence (PL).

## 2. Experimental Procedure

Figure 1 shows the flow chart of the experiment for this study. Before deposition, PET substrates with a thickness of 0.1 mm were cleaned with isopropyl alcohol and blown dry with nitrogen. The metal Zn target with a diameter of 100 mm and purity of 99.99% as a cathode target was held in an alumina ceramic tube; oxygen and argon gas with high purity of 99.99% were used as the reactant gas. The PET substrates were loaded into the CVAD chamber with a substrate-anode distance of approximately 21 cm, and the chamber was evacuated to 10<sup>-5</sup> Torr by a rotary and diffusion pump arrangement in the depositions of ZnO films. The system used a relatively low DC voltage to trigger and sustain a metal arc plasma. The O<sub>2</sub>/Ar gas flow ratios (6 : 1 to 10 : 1) in cathodic vacuum arc deposition system were experimental variables. Substrate rotation of 2 r.p.m., discharge current in 80 A, and working pressure in 10<sup>-3</sup> Torr were kept constant during the deposition work. No extra heating was provided to the depositions of ZnO films; namely, deposition was performed at room temperature. In the study, Ar was in 20 sccm and O<sub>2</sub> were in 120, 140, 160, 180, and 200 sccm; namely, the O<sub>2</sub>/Ar gas flow ratios were 6 : 1, 7 : 1, 8 : 1, 9 : 1, and 10 : 1.

For the microstructure characterization, X-ray diffraction (XRD, BRUKER D8 ADVANCE) equipped with CuK $\alpha$  radiation of average wavelength 1.5406 Å was used to specify the existent phases, the orientation, and the stress of ZnO thin films. X-ray patterns were taken 2θ between 20° and 60° and scan speed of 4.5°/min. For the optical characterization, UV-VIS spectrometer (Thermo Evolution-300) was used to measure the optical properties of ZnO films in the wavelength range of 200–800 nm. Moreover, the absorption coefficient  $\alpha$  could be determined from absorption spectra to further

obtain the optical bandgap of the deposited films. For the electrical characterization, the four-point probe was acquired at room temperature to measure the resistivity and Hall measurement was used to determine the carrier concentration and mobility of the deposited films. Moreover, the photoluminescence (PL) spectra measurement (Jasco FP-6600) via optical excitation by a Xe lamp with an excitation wavelength of 325 nm was used to measure the defect types of the deposited films from the PL data acquired in the wavelength range of 350–800 nm.

## 3. Result and Discussion

**3.1. Microstructure.** Figure 2 shows the XRD patterns of the deposited ZnO films on PET substrate with various O<sub>2</sub>/Ar gas flow ratios. Since the PET substrate is amorphous, the crystallographic structure of the substrate would not affect the film crystal orientation [2]. It is clearly observed that the deposited films show hexagonal wurtzite crystal structure and has a (002) peak which is close to that of the standard ZnO crystal (34.45°), indicating that the film has a preferred orientation with the *c*-axis perpendicular to the substrate [11]. However, it is observed that with O<sub>2</sub>/Ar gas flow ratio of 6 : 1, a small broad peak (103) in 62° also appeared, showing the deposited film is polycrystalline. Namely, the grains in the film are not completely perpendicular to the substrate surface. Typically, three energy types appeared in the deposited film on a substrate, such as surface energy of the film and interface energy between film/substrate and the strain energy in the film. Among the various low index ZnO planes, the *c*-axis plane has the lowest surface energy. In general, the films are grown to achieve a minimized total energy [7]. Thus, crystal orientation of the growing film is formed from a self-ordering effect because of the minimization of the crystal surface free energy as well as the interaction between the deposited film and the substrate [10]. However, if the films are not deposited under the preferred range of the deposition parameters, *c*-axis orientation would be deteriorated and other orientations then appeared [11]. Moreover, the *c*-axis (002) oriented intensity decreases with increasing the O<sub>2</sub>/Ar gas flow ratios from 6 : 1 to 10 : 1. This behavior reveals that with increased oxygen flow the crystallinity of the deposited ZnO films is firstly improved and then decreased. The appropriate O<sub>2</sub>/Ar gas flow ratio is required to grow oriented crystalline ZnO film [12].

To further investigate the crystallographic quality, the film properties obtained from the XRD data are summarized in Table 1, such as the full width at half maximum (FWHM), crystallite size ( $D$ ), crystal lattice constant ( $c$ ), interplanar distance ( $d$ ), and film stress ( $\sigma$ ). The crystallite sizes of the grown films are estimated using the Scherrer formula [13]:

$$D = \frac{0.9\lambda}{\beta \cos \theta}, \quad (1)$$

where  $\lambda = 1.541$  Å is the wavelength of X-ray,  $\theta$  is the angle between the incoming X-ray and the normal of the diffracting plane, and  $\beta$  is FWHM form the broadening of the (002) diffraction line. The crystallite sizes are obtained as 17.3 nm, 22.2 nm, 22.8 nm, 23.4 nm, 18.3 nm, and 16.0 with the O<sub>2</sub>/Ar

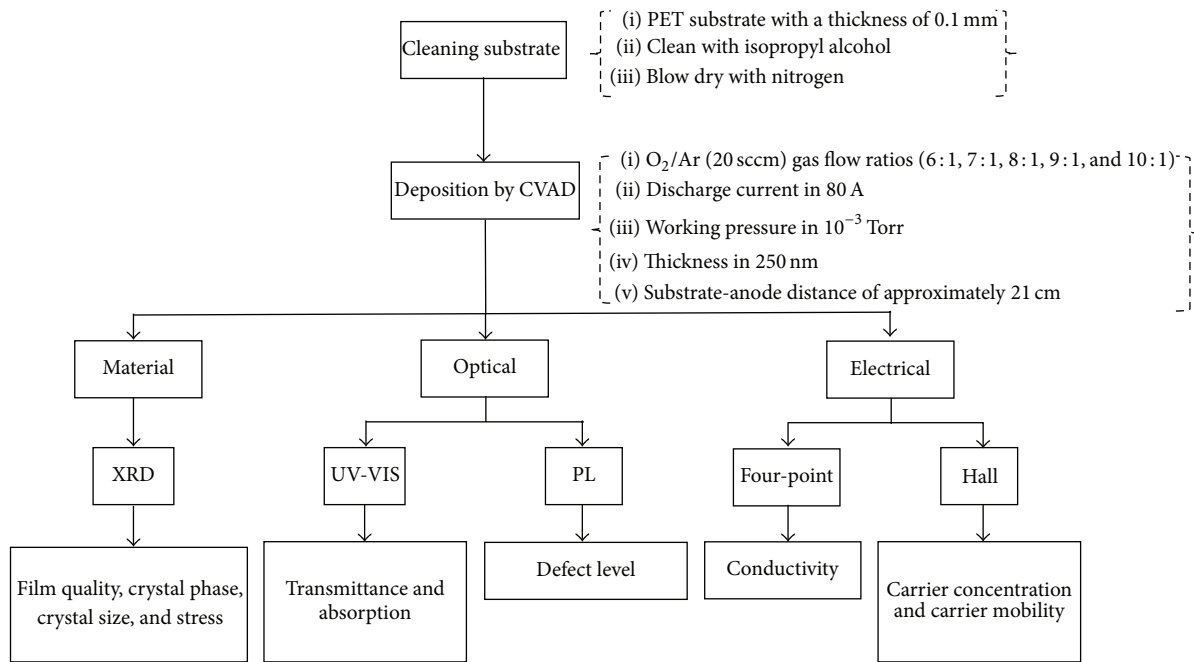
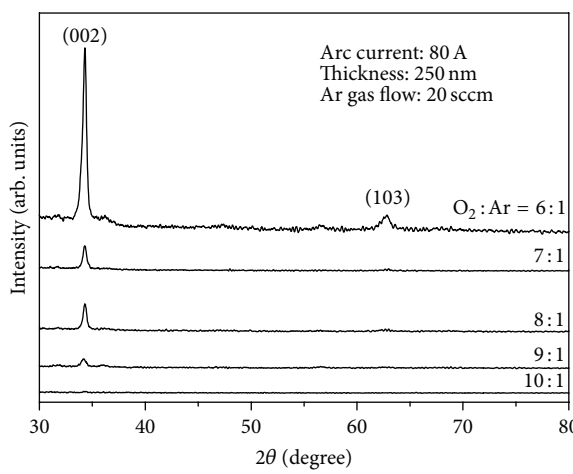


FIGURE 1: The flow chart of fabrication of the research.

TABLE 1: Material properties of the room-temperature deposited ZnO films on the PET substrate with various O<sub>2</sub>/Ar gas flow ratios.

O <sub>2</sub> /Ar	6:1	7:1	8:1	9:1	10:1
Intensity of (002) (a.u.)	620	87	87	27	3
2θ (°)	34.31	34.28	34.28	34.22	34.19
FWHM	0.38	0.37	0.36	0.51	0.526
D (nm)	22.2	22.8	23.4	16.5	16.0
d (nm)	0.2615	0.2613	0.2611	0.2612	0.2612
c (nm)	0.523038	0.522668	0.522299	0.522476	0.5243
σ (Pa)	-2.11E + 09	-1.79E + 09	-1.47E + 09	-3.20E + 09	-3.62E + 09

FIGURE 2: The XRD patterns of the room-temperature deposited ZnO films on the PET substrate with various O<sub>2</sub>/Ar gas flow ratios.

gas flow ratios of 6:1, 7:1, 8:1, 9:1, and 10:1, respectively. The crystallite size increases first and then decreases when

the O<sub>2</sub> flow increases. This result may be attributed to the reasons. First, desired introduction of oxygen in plasma generates high-energy oxygen neutral atoms and accelerates grain growth in the deposited films under the O<sub>2</sub>/Ar gas flow ratios from 6:1 to 8:1. With more and more oxygen gas introduction, attack of high-energy neutral oxygen atoms would increase and then change the surface topology of the deposited film at the early phase during the film growth, causing the decrease of the grain aggregation [1, 7].

The c value and the d value are identified using the Bragg equation  $n\lambda = 2d \sin \theta$ , where n is the order of the diffracted beam. The calculation of the film stress is based on the biaxial strain model and the stress in the plane of ZnO film with a hexagonal crystal structure can be expressed as [2]

$$\sigma = 4.5 \times 10^{11} \left( \frac{C_{\text{film}} - C_{\text{bulk}}}{C_{\text{bulk}}} \right), \quad (2)$$

where  $C_{\text{film}}$  and  $C_{\text{bulk}}$  are the lattice parameters of film and the strain-free lattice parameter of ZnO thin films, respectively. The stress is -2.11, -1.79, -1.47, -3.2, and -3.26 GPa when the O<sub>2</sub>/Ar gas flow ratio is 6:1, 7:1, 8:1, 9:1, and 10:1, respectively. The result indicates the compressive stress in the film

also decreases first and then increases with increasing O<sub>2</sub>/Ar flow ratio. The energetic bombardment of the deposited film is usually compressive because of the atomic peening during the CVAD process [8].

**3.2. Optical Properties.** Figure 3 shows transmittance of the room-temperature deposited ZnO films on the PET substrate with various O<sub>2</sub>/Ar gas flow ratios. The transmittance of pure PET substrate is also measured as the data reference. The average transmittance of PET substrate is in 93.32% in the visible range. The average transmittances of all the films in the visible range are over 83%, and the maximum transmittance is 86.38% as the O<sub>2</sub>/Ar gas flow ratio is 8:1. Therefore, the average transmittances of the ZnO thin films deposited on the PET substrate were slightly lower than data reference of PET substrate and it is reasonably concluded that a better crystallinity reaches a higher transmittance [13]. However, the average transmittances of the ZnO thin films deposited on the PET still match the transmittance requirement of most device applications.

The absorption spectra are typically used to evaluate the optical energy band gap of the ZnO film. In the direct transition semiconductor, the relation between optical absorption coefficient ( $\alpha$ ) and the optical energy band gap (Eg) is expressed as [13]

$$(\alpha h\nu)^2 = A (h\nu - Eg), \quad (3)$$

where  $\alpha$  is estimated from the transmittance data and  $A$  is a constant depending on the materials properties.  $(\alpha h\nu)^2$  is a function of  $h\nu$ ,  $h$  is Planck's constant, and  $\nu$  is the angular frequency of the incident photon. Figure 4 shows the plot of  $(\alpha h\nu)^2$  as function of the incident photon energy. The Eg is obtained from intercept of the extrapolated linear part of the curve. The optical band gaps of the room-temperature deposited ZnO films on the PET substrate with various O<sub>2</sub>/Ar gas flow ratios of 6:1, 7:1, 8:1, 9:1, and 10:1 are 3.16, 3.17, 3.21, 3.20, and 3.17 eV, respectively. It was reported that as the O<sub>2</sub> flow rate increased, the subband gap absorption at wavelengths longer than 400 nm caused by metallic Zn clusters embedded in the ZnO film would decrease notably and thus the deposited film became more transparent.

**3.3. Electrical Properties.** Figure 5 shows the electrical resistivity ( $\rho$ ), Hall mobility ( $\mu$ ), and carrier concentration ( $n$ ) of the deposited ZnO films. The Hall mobility ( $\mu$ ) is in the range from 3 to 4 cm<sup>2</sup>/s·V and increases slightly and then decreases with increasing O<sub>2</sub>/Ar gas flow ratios. The trend of the Hall mobility ( $\mu$ ) is similar to the crystal size. The different O<sub>2</sub>/Ar gas flow ratios affect crystal size and thus affect the electrical properties. It is suggested that carriers are scattered essentially by grain boundaries as well as the intrinsic defects in an undoped film, and thus increase of crystal size would reduce the boundary and then reduce the carrier scattering, thus improving the Hall mobility ( $\mu$ ) [11]. The carrier concentration ( $n$ ) also increases first and then decreases with increasing O<sub>2</sub>/Ar gas flow ratios, indicating that the carrier concentration in the ZnO film can be tuned by adjusting the O<sub>2</sub> flow rate during the deposition. All

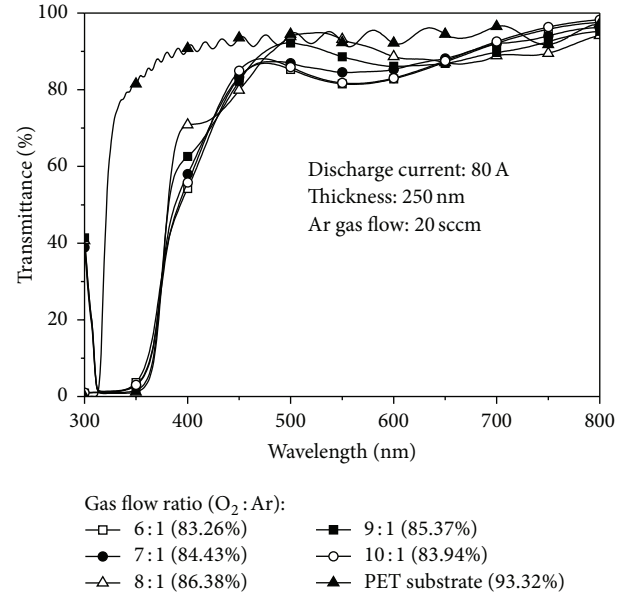


FIGURE 3: Transmittance of the room-temperature deposited ZnO films on the PET substrate with various O<sub>2</sub>/Ar gas flow ratios.

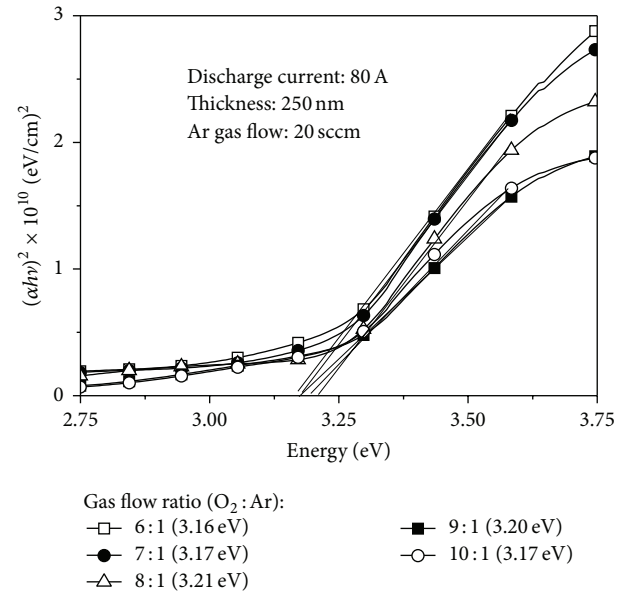


FIGURE 4: Absorption spectra of the room-temperature deposited ZnO films on the PET substrate with various O<sub>2</sub>/Ar gas flow ratios.

the deposited films are shown as n-type conduction. The resistivity has a minimum value in the  $3.65 \times 10^{-3}$  Ω·cm, with a mobility of  $4.8 \text{ cm}^2/\text{V}\cdot\text{s}$  and a carrier concentration of  $5.89 \times 10^{20} \text{ cm}^{-3}$  under the O<sub>2</sub>/Ar gas flow ratio of 8:1.

To consider the applications of the deposited thin films, the sheet resistance shall be known first. The sheet resistance is calculated by using the measured resistivity and the film thickness. Since all the film thickness is around 250 nm, the sheet resistivities of the deposited ZnO films are about 146 to 200 Ω/□. It is suggested that the deposited ZnO thin films on

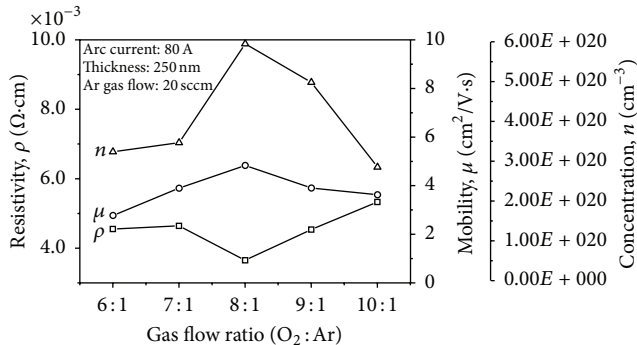


FIGURE 5: The resistivity ( $\rho$ ), mobility ( $\mu$ ), and concentration ( $n$ ) of the room-temperature deposited ZnO films on the PET substrate with various  $O_2/Ar$  gas flow ratios.

PET substrate are considered to be suitable for the use of the flexible resistive touch panel. Moreover, if the ZnO thin films want to be used in the former electrode of solar cells, the sheet resistivities of the deposited ZnO films shall be lower since the lower sheet resistivities make lower series resistance, thus improving the output short current of the solar cell.

**3.4. Defect Types.** Figure 6 displays PL spectra of the ZnO thin films as functions of various  $O_2/Ar$  gas flow ratios. The result shows an obvious near ultraviolet (UV) emission peak from 380 nm to 450 nm, a broad blue-green emission peak from 450 nm to 570 nm, and a weak red emission peak from 750 nm to 800 nm. The intensity of the luminescent band is varied with the  $O_2/Ar$  gas flow ratios and has strongest UV emission intensity when  $O_2/Ar$  gas flow ratio is 8:1.

It is known that the oxygen flow rate typically affects the defect types of pure ZnO films deposited at a low temperature. Figure 7 shows typical PL spectra of the deposited ZnO thin film with  $O_2/Ar$  gas flow ratio of 8:1 and its Gaussian fit band. The peaks of five main Gaussian fit bands are at 387, 411, 451, 550, and 775 nm.

The near UV emission at approximately 387 nm typically resulted from an exciton transition related near band edge emission (NBE) of the wide band gap ZnO [1, 14]. The other visible peaks are generally correlated to the luminescence of defects. The blue-green emission mainly resulted from oxygen vacancies ( $V_O$ ), zinc vacancies ( $V_{Zn}$ ), oxygen interstitials ( $O_i$ ), zinc interstitials ( $Zn_i$ ), and oxygen displacement zinc [2]. The emission at 411 nm (e.g., 3.01 eV) in the blue emission is due to the defects from zinc interstitial ( $Zn_i$ ) in the ZnO film [15]. It was reported that the formation of zinc interstitial in the ZnO film resulted from the energetic zinc particles in the cathodic plasma and low substrate temperature [6]. The optical energy for the emission at 451 nm (e.g., 2.79 eV) is close to the energy interval (2.65 eV) between the level of the zinc interstitial ( $Zn_i$ ) and the level of zinc vacancy ( $V_{Zn}$ ) [15]. Moreover, the luminescence mechanisms of other defect emissions at 550 nm (e.g., 2.25 eVm) and at 775 nm (e.g., 1.6 eV) in the red emission may result from the defects of oxygen interstitial ( $O_i$ ) and oxygen vacancy ( $V_O$ ) in the ZnO film, respectively [1, 14]. It is verified that the conductive property of the pure ZnO film is attributed to the intrinsic

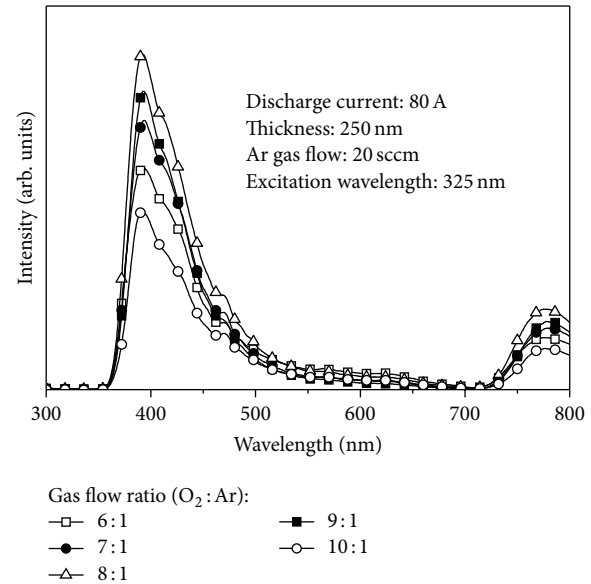


FIGURE 6: PL spectra of the room-temperature deposited ZnO films on the PET substrate with various  $O_2/Ar$  gas flow ratios.

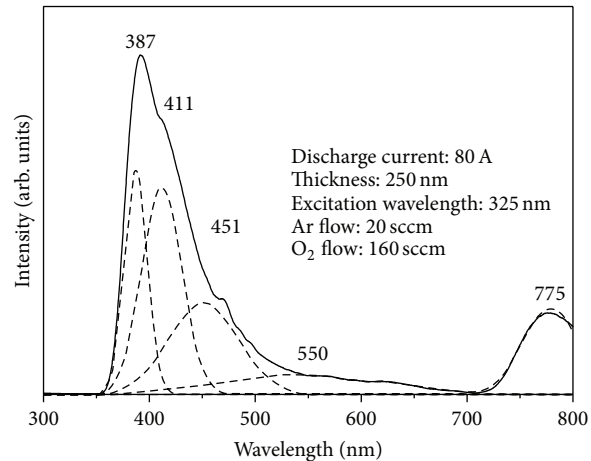


FIGURE 7: Typical PL spectra of the deposited ZnO thin film with  $O_2/Ar$  gas flow ratio of 8:1 and its Gaussian fit band.

defects such as oxygen vacancy ( $V_O$ ) and zinc interstitial ( $Zn_i$ ), resulting in the origin of deep-level-emission (DLE) band [7].

#### 4. Conclusion

We have deposited pure ZnO thin film on PET substrate using the CVAD system at different  $O_2/Ar$  gas flow ratios at a room temperature. The crystalline as well as crystal sizes are increased with adjusting  $O_2/Ar$  gas flow ratio in the optimum value of 8:1. The mobility and carrier concentration increased with  $O_2/Ar$  gas flow ratios and dominated by the grain boundary scattering due to the increased crystal size. The average transmittance values in the visible range of the deposited ZnO films were all higher than 83% and the calculated band gaps from the absorption data were found

to be around 3.1 to 3.2 eV. The conductive property of the deposited ZnO film resulted from the origin of deep-level-emission (DLE) band, attributed to the intrinsic defects such as oxygen vacancy ( $V_O$ ) and zinc interstitial ( $Zn_i$ ), and showed a minimum value in  $3.65 \times 10^{-3} \Omega\text{-cm}$ , with a mobility of  $4.8 \text{ cm}^2/\text{V}\cdot\text{s}$  and a carrier concentration of  $5.89 \times 10^{20} \text{ cm}^{-3}$  under the  $O_2/\text{Ar}$  gas flow ratio of 8 : 1. For the future work, the mechanical properties of the CVAD ZnO films shall be investigated to verify the usability on the flexible electronics.

## Competing Interests

The authors declare that they have no competing interests.

## Acknowledgments

The authors would like to thank the funding support from the Ministry of Science and Technology, Taiwan, under Contract NSC 101-2628-E-020-002-MY3. The authors would also like to thank the National Nano Device Laboratories and the Precision Instrument Center of National Pingtung University of Science and Technology for the support through the experimental equipment.

## References

- [1] K. Ellmer, A. Klein, and B. Rech, *Transparent Conductive Zinc Oxide*, Springer, Berlin, Germany, 2008.
- [2] H. Morkoc and U. Ozgur, *Zinc Oxide: Fundamentals, Materials and Device Technology*, John Wiley & Sons, New York, NY, USA, 2009.
- [3] Ü. Özgür, Y. I. Alivov, C. Liu et al., "A comprehensive review of ZnO materials and devices," *Journal of Applied Physics*, vol. 98, Article ID 041301, 2005.
- [4] A. N. Banerjeea, C. K. Ghosha, K. K. Chattopadhyaya et al., "Low-temperature deposition of ZnO thin films on PET and glass substrates by DC-sputtering technique," *Thin Solid Films*, vol. 496, no. 1, pp. 112–116, 2006.
- [5] J.-C. Hwang, M.-C. Choi, Y. Ha et al., "Effect of side groups in polynorbornene films for transparent conductive substrates," *Journal of Nanoscience and Nanotechnology*, vol. 11, no. 1, pp. 550–554, 2011.
- [6] X. L. Zhang, K. N. Hui, K. S. Hui, and J. Singh, "Structural and optical characterization of high-quality ZnO thin films deposited by reactive RF magnetron sputtering," *Materials Research Bulletin*, vol. 48, no. 3, pp. 1093–1098, 2013.
- [7] Y. G. Wang, S. P. Lau, H. W. Lee et al., "Comprehensive study of ZnO films prepared by filtered cathodic vacuum arc at room temperature," *Journal of Applied Physics*, vol. 94, no. 3, pp. 1597–1604, 2003.
- [8] H. W. Lee, S. P. Lau, Y. G. Wang, K. Y. Tse, H. H. Hng, and B. K. Tay, "Structural, electrical and optical properties of Al-doped ZnO thin films prepared by filtered cathodic vacuum arc technique," *Journal of Crystal Growth*, vol. 268, no. 3-4, pp. 596–601, 2004.
- [9] B. K. Tay, Z. W. Zhao, and D. H. C. Chua, "Review of metal oxide films deposited by filtered cathodic vacuum arc technique," *Materials Science and Engineering R: Reports*, vol. 52, no. 1–3, pp. 1–48, 2006.
- [10] C. Li, X. C. Li, P. X. Yan et al., "Research on the properties of ZnO thin films deposited by using filtered cathodic arc plasma technique on glass substrate under different flow rate of  $O_2$ ," *Applied Surface Science*, vol. 253, no. 8, pp. 4000–4005, 2007.
- [11] C.-T. Pan, R.-Y. Yang, M.-H. Weng, and C.-W. Huang, "Properties of low-temperature deposited ZnO thin films prepared by cathodic vacuum arc technology on different flexible substrates," *Thin Solid Films*, vol. 539, pp. 290–293, 2013.
- [12] M.-H. Weng, C.-T. Pan, R.-Y. Yang, and C.-C. Huang, "Structure, optical and electrical properties of ZnO thin films on the flexible substrate by cathodic vacuum arc technology with different arc currents," *Ceramics International*, vol. 37, no. 8, pp. 3077–3082, 2011.
- [13] R.-Y. Yang, M.-H. Weng, C.-T. Pan, C.-M. Hsiung, and C.-C. Huang, "Low-temperature deposited ZnO thin films on the flexible substrate by cathodic vacuum arc technology," *Applied Surface Science*, vol. 257, no. 16, pp. 7119–7122, 2011.
- [14] K. Yim, H. Kim, and C. Lee, "Effects of the  $O_2/\text{Ar}$  gas flow ratio on the electrical and transmittance properties of ZnO:Al films deposited by RF magnetron sputtering," *Journal of Electroceramics*, vol. 17, no. 2"4, pp. 875–877, 2006.
- [15] A. B. Djurišić, Y. H. Leung, K. H. Tam et al., "Green, yellow, and orange defect emission from ZnO nanostructures: influence of excitation wavelength," *Applied Physics Letters*, vol. 88, no. 10, Article ID 103107, 2006.

## Research Article

# Effect of Top-Region Area of Flat-Top Pyramid Patterned Sapphire Substrate on the Optoelectronic Performance of GaN-Based Light-Emitting Diodes

**Hsu-Hung Hsueh,<sup>1</sup> Sin-Liang Ou,<sup>2</sup> Yu-Che Peng,<sup>1</sup> Chiao-Yang Cheng,<sup>3</sup> Dong-Sing Wuu,<sup>2,4</sup> and Ray-Hua Horng<sup>1,5</sup>**

<sup>1</sup>Graduate Institute of Precision Engineering, National Chung Hsing University, Taichung 402, Taiwan

<sup>2</sup>Department of Materials Science and Engineering, Da-Yeh University, Changhua 515, Taiwan

<sup>3</sup>Wafer Works Corporation, Taoyuan 32542, Taiwan

<sup>4</sup>Department of Materials Science and Engineering, National Chung Hsing University, Taichung 402, Taiwan

<sup>5</sup>Department of Electronics Engineering, National Chiao Tung University, Hsinchu 300, Taiwan

Correspondence should be addressed to Ray-Hua Horng; [rhh@nctu.edu.tw](mailto:rhh@nctu.edu.tw)

Received 31 March 2016; Accepted 16 June 2016

Academic Editor: Wei-Heng Shih

Copyright © 2016 Hsu-Hung Hsueh et al. This is an open access article distributed under the Creative Commons Attribution License, which permits unrestricted use, distribution, and reproduction in any medium, provided the original work is properly cited.

The flat-top pyramid patterned sapphire substrates (FTP-PSSs) have been prepared for the growth of GaN epilayers and the fabrication of lateral-type light-emitting diodes (LEDs) with an emission wavelength of approximately 470 nm. Three kinds of FTP-PSSs, which were denoted as FTP-PSS-A, FTP-PSS-B, and FTP-PSS-C, respectively, were formed through the sequential wet etching processes. The diameters of circle areas on the top regions of these three FTP-PSSs were 1, 2, and 3  $\mu\text{m}$ , respectively. Based on the X-ray diffraction results, the full-width at half-maximum values of rocking curves at (002) plane for the GaN epilayers grown on conventional sapphire substrate (CSS), FTP-PSS-A, FTP-PSS-B, and FTP-PSS-C were 412, 238, 346, and 357 arcsec, while these values at (102) plane were 593, 327, 352, and 372 arcsec, respectively. The SpeCLED-Ratio simulation results reveal that the LED prepared on FTP-PSS-A has the highest light extraction efficiency than that of the other devices. At an injection current of 350 mA, the output powers of LEDs fabricated on CSS, FTP-PSS-A, FTP-PSS-B, and FTP-PSS-C were 157, 254, 241, and 233 mW, respectively. The results indicate that both the crystal quality of GaN epilayer and the light extraction of LED can be improved via the use of FTP-PSS, especially for the FTP-PSS-A.

## 1. Introduction

Recently, GaN-based materials have received a lot of attention for many optoelectronic applications consisting of light-emitting diodes (LEDs), laser diodes, and high-power devices [1–3]. Because the price of bulk GaN substrate is very high, the GaN-based epilayers should be prepared on foreign substrates, such as sapphire and silicon carbide. At present, sapphire is the most common substrate for the epitaxial growth of GaN-based LEDs. However, owing to the large mismatch in lattice constant between GaN and sapphire, a large number of threading dislocations (TDs) generated during the epitaxial growth process would lead to a serious

degradation of the GaN crystal quality. For the fabrication of GaN-based LEDs, the deterioration of epitaxial quality will obviously limit their optoelectronic performances including internal quantum efficiency (IQE), electron mobility, and device lifetime.

Thus, to reduce the TD density of GaN epitaxial film, several techniques have been presented [4–6]. Among these techniques, the epitaxial lateral overgrowth (ELOG) employing the stripe-mask patterns on the GaN epilayer is a useful method to obstruct the propagation of TDs efficiently, resulting in a significant reduction of TD density [4]. Nevertheless, when the ELOG is performed, the growth interruption caused by the mask deposition is inevitable. Additionally,

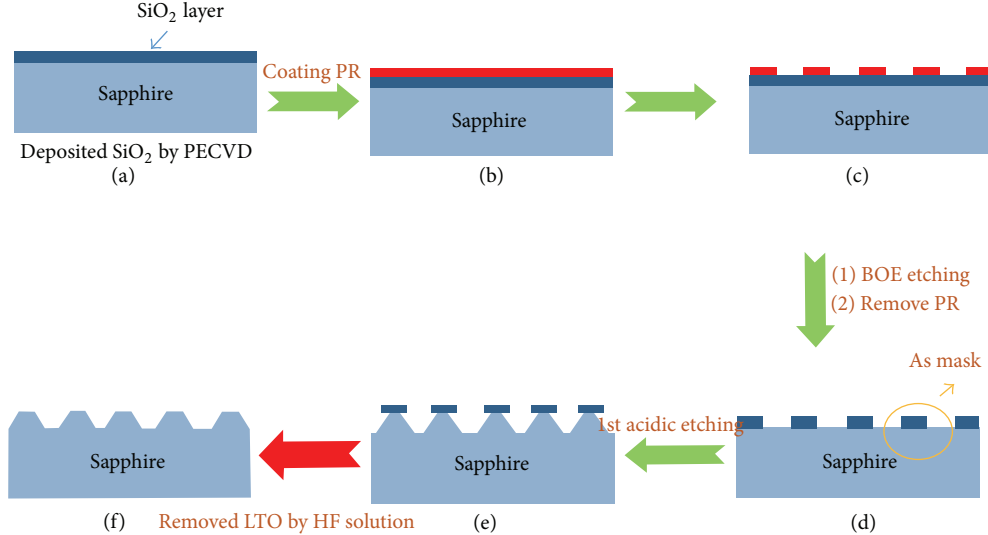


FIGURE 1: Fabrication processes of FTP-PSS: (a) growth of a  $\text{SiO}_2$  layer on the  $c$ -plane sapphire by PECVD, (b) preparation of a thick PR on the  $\text{SiO}_2$  layer by spin-coating, (c) performing the photolithography technique to open the PR mask, (d) formation of the round-shaped  $\text{SiO}_2$  layer via the buffered oxide etching and removal of the PR mask, (e) wet etching to the sapphire substrate using a mixed  $\text{H}_2\text{SO}_4 : \text{H}_3\text{PO}_4$  (3 : 1) solution at 250°C for 30 min, and (f) removal of the  $\text{SiO}_2$  mask layer using a HF solution.

the formation of mask could also induce the impurity contamination in the subsequent epilayers. To overcome these mask-related drawbacks, the mask-free patterned sapphire substrate (PSS) technology has been proposed and becomes very promising for the growth of high-quality GaN epilayer [7–10]. Except for the improvement in the IQE, the use of PSS also can increase the light extraction efficiency (LEE) of LEDs due to the nonplanar interface between sapphire and GaN.

In previous researches, the InGaN/GaN film with high crystal quality can be achieved using metalorganic chemical vapor deposition (MOCVD) on the flat-top pyramidal PSS (FTP-PSS) [8–10]. These researches confirm that the FTP-PSSs are indeed helpful to enhance the performance of LEDs. However, the influence of pattern size of the FTP-PSS on the device characteristics is seldom studied. In our work, three FTP-PSSs were fabricated to serve as the substrates for the growth of GaN-based epitaxial structures. In these three FTP-PSSs, the heights of patterns are equal to each other. Meanwhile, the diameters of circle areas on both the top and the bottom regions of the flat-top pyramidal patterns in these FTP-PSSs are modified. The effect of the flat-top region area of FTP-PSS on the device performance was investigated.

## 2. Experimental

The fabrications of PSSs with the flat-top pyramid patterns were completed through the wet etching processes sequentially, as described in Figure 1. As shown in Figure 1(a), the  $\text{SiO}_2$  layer with a thickness of 250 nm was firstly prepared on the  $c$ -plane sapphire by plasma enhanced chemical vapor deposition (PECVD). Then, a thick photoresist (PR) was grown on the  $\text{SiO}_2$  layer as a mask by spin-coating (Figure 1(b)). To open the PR mask, the photolithography technique was performed on the PR layer (Figure 1(c)). In

Figure 1(d), the round-shaped  $\text{SiO}_2$  layer was prepared using a buffered oxide etch (BOE) solution to serve as a mask for the fabrication of PSS, and the PR mask was removed. As shown in Figure 1(e), the sapphire substrate with the  $\text{SiO}_2$  mask was etched using a mixed  $\text{H}_2\text{SO}_4 : \text{H}_3\text{PO}_4$  (3 : 1) solution at 250°C for 30 min. In this research, three different diameters (1, 2, and 3  $\mu\text{m}$ ) of round shape were designed for the  $\text{SiO}_2$  mask layers. Thus, after removing the  $\text{SiO}_2$  mask layer using a HF solution (Figure 1(f)), the FTP-PSSs with three different top-region areas can be formed.

Except for the FTP-PSSs used to fabricate the LEDs, the LED on the conventional sapphire substrate (CSS) was also prepared as the contrasted sample. The LED epitaxial structures grown on FTP-PSSs and CSS were performed by low-pressure MOCVD at the same growth conditions. The LED epitaxial structure consisted of a 3  $\mu\text{m}$  thick undoped GaN (u-GaN) layer, a 2  $\mu\text{m}$  thick n-type GaN:Si layer, 11 periods of InGaN/GaN multiple quantum wells (MQW), a 100 nm thick p-type AlGaN layer, and a 0.2  $\mu\text{m}$  thick p-type GaN:Mg layer. At the beginning of epitaxial growth, it is noted that a 30 nm thick GaN buffer layer was prepared at low temperature (530°C), and then a 3  $\mu\text{m}$  thick u-GaN layer was deposited at high temperature (1150°C). After growing these epilayers, the device processes for lateral-type LED were carried out subsequently. Firstly, a mesa pattern with the size of 45 mil  $\times$  45 mil was defined and prepared via the standard photolithography and dry etching processes. Then, the ITO film was grown on the p-type GaN layer to serve as a transparent conducting layer. The ITO film was deposited by E-beam evaporation at 270°C, and its thickness was 200 nm. Finally, the Ti/Al/Ti/Au (15/2000/25/60 nm) metal layers grown on the sample by thermal evaporation were adopted as both n-pad and p-pad electrodes. These LEDs all possess the emission wavelength approximately 470 nm.

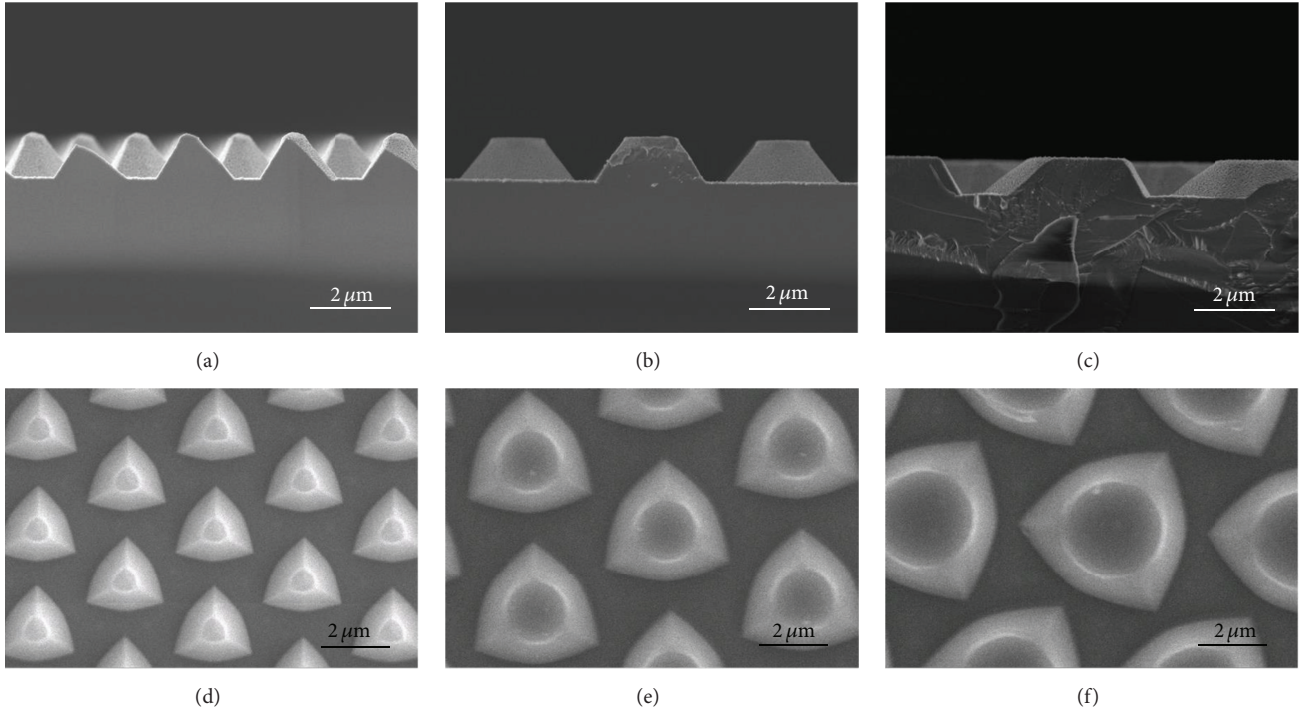


FIGURE 2: Cross-sectional SEM image of (a) FTP-PSS-A, (b) FTP-PSS-B, and (c) FTP-PSS-C. Top-view SEM images of (d) FTP-PSS-A, (e) FTP-PSS-B, and (f) FTP-PSS-C.

Crystal quality of the u-GaN epilayer was determined by X-ray diffraction (XRD, Philips X'Pert MRD). Here, the analyses of (002) and (102) planes for the u-GaN epilayer were both performed. The surface morphology of the FTP-PSS was observed by scanning electron microscopy (SEM, JEOL JSM-7001F). Current-voltage ( $I-V$ ) characteristics of these LEDs were investigated by a semiconductor parameter analyzer (Keithley, 2400 SourceMeter), and the output powers were measured with a calibrated integrating sphere. To quantitatively characterize the light extraction efficiency of LEDs on these sapphires, the simulation of photon trajectory was performed by SpeCLED-Retro software (commercial light-simulation software based on geometrical optics).

### 3. Results and Discussion

As mentioned above, during the fabrication process of FTP-PSSs, three  $\text{SiO}_2$  mask layers with various diameters of 1, 2, and  $3\ \mu\text{m}$  of round shape were prepared. Then, three various FTP-PSSs, that were denoted as FTP-PSS-A, FTP-PSS-B, and FTP-PSS-C, respectively, were formed via the sequential wet etching processes. Figures 2(a), 2(b), and 2(c) show the cross-sectional SEM images of FTP-PSS-A, FTP-PSS-B, and FTP-PSS-C, respectively. We can observe that the heights of patterns of these three FTP-PSSs were all fixed at  $1.4\ \mu\text{m}$ . Figures 2(d) and 2(e) show the top-view SEM images of these three FTP-PSSs, respectively. The diameters of circle areas on the top and bottom regions of FTP-PSS-A, FTP-PSS-B, and FTP-PSS-C were  $1$  and  $2.4\ \mu\text{m}$ ,  $2$  and  $3.8\ \mu\text{m}$ , and  $3$  and  $5.2\ \mu\text{m}$ , respectively. Meanwhile, the distances between patterns of these three FTP-PSSs were  $0.85$ ,  $0.85$ , and  $0.75\ \mu\text{m}$ ,

respectively. Obviously, the area of flat-top region for these three FTP-PSSs decreased in the following order: FTP-PSS-C > FTP-PSS-B > FTP-PSS-A. This indicates that the FTP-PSS-C has the largest  $c$ -plane area of flat-top region, while the FTP-PSS-A possesses the smallest one among these three samples.

The crystal qualities of the u-GaN epilayers grown on CSS and FTP-PSSs were estimated by measuring the full-width at half-maximum (FWHM) values derived from the XRD rocking curves. The XRD rocking curves obtained for the symmetric GaN(002) plane and the asymmetric GaN(102) plane of these four samples are presented in Figures 3(a) and 3(b), respectively. By growing the u-GaN epilayer on the CSS, the FWHM value at the (002) plane was  $412$  arcsec, while the FWHM value at the (102) plane was  $593$  arcsec. Noted that the FWHMs at (002) and (102) of CSS have a little large as compared with those of previously reports [11, 12]. It is well known that the crystal quality of the epilayer is dependent on the MOCVD system. In this study, the growth parameters of CSS have been optimized. On the other hand, the FWHM values at the (002) plane for the u-GaN epilayers grown on FTP-PSS-A, FTP-PSS-B, and FTP-PSS-C were  $238$ ,  $346$ , and  $357$  arcsec, respectively. Additionally, the FWHM values at the (102) plane for the u-GaN epilayers prepared on these three FTP-PSSs were measured to be  $327$ ,  $352$ , and  $372$  arcsec, respectively. It is well known that crystal quality of the (002) plane was influenced by screw and mixed dislocations, while the crystal quality of (102) plane was influenced by edge, screw, and mixed dislocations [13]. It is clear that the crystallinity of u-GaN epilayer grown on the FTP-PSS is much higher than that on the CSS. This can be attributed to the reduction in the dislocation density of GaN epilayer

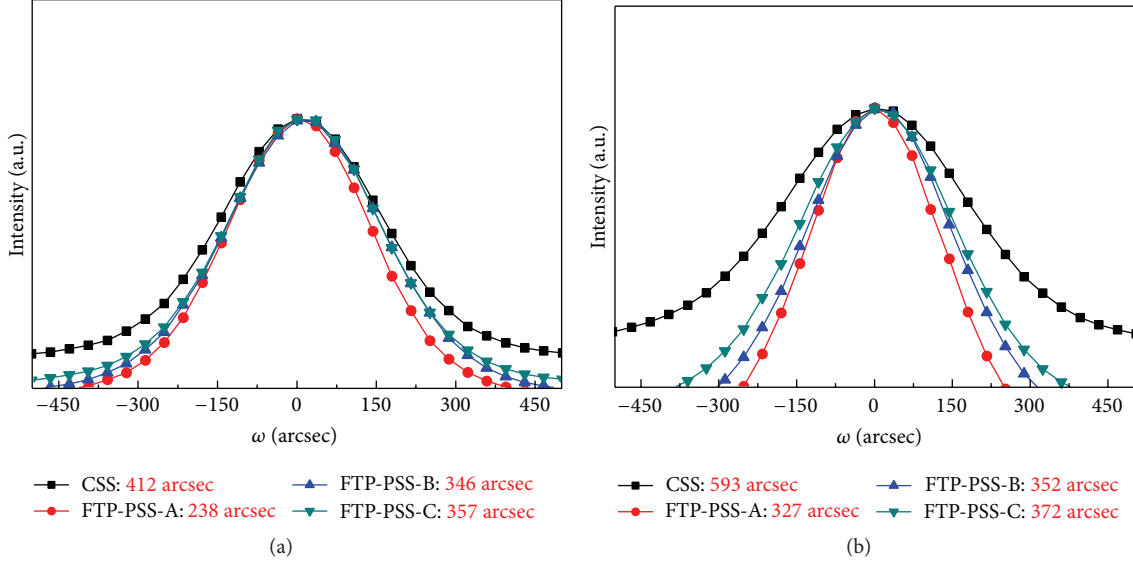


FIGURE 3: XRD rocking curves obtained for (a) the symmetric GaN(002) plane and (b) the asymmetric GaN(102) plane of GaN epilayers grown on CSS and various FTP-PSSs.

grown on the FTP-PSS. Obviously, the fabrication of FTP-PSS is useful to enhance the crystal quality of GaN epilayer.

Except for the XRD FWHM value, the evaluation of dislocation density also can be used to analyze the crystal quality of u-GaN epilayer. The TD characteristics in u-GaN films on CSS and FTP-PSSs were investigated by etch-pit-density (EPD) measurements. The etching process was performed by soaking the samples into the  $\text{H}_2\text{SO}_4 : \text{H}_3\text{PO}_4$  (3:1) mixed solution at 250°C for 10 min. Figures 4(a), 4(b), 4(c), and 4(d) display the SEM images for the TDs of u-GaN epilayers on CSS, FTP-PSS-A, FTP-PSS-B, and FTP-PSS-C, respectively. It can be found that the EPDs of these four samples were estimated to be  $3.25 \times 10^7$ ,  $1.39 \times 10^6$ ,  $2.31 \times 10^6$ , and  $5.17 \times 10^6 \text{ cm}^{-2}$ , respectively. As marked in Figures 4(a) and 4(b), the feature of the screw dislocation is a well-defined hexagonal shape with a large black core, while the mixed dislocation has an unclear hexagonal shape with a small black core. Besides, the edge dislocation shows an unclear polygon [12, 14]. It was obvious that three various types of TDs all can be identified in the GaN epilayer on the CSS (Figure 4(a)). After growing the GaN epilayer on the FTP-PSS, the formation of these three types of TDs reduced efficiently. Moreover, the suppressions of screw and mixed TDs are more obvious than that of edge TDs. Based on XRD and EPD results, the dislocation density of GaN epilayer on the FTP-PSS can be decreased apparently as compared with that on CSS. As the FTP-PSSs were used, the GaN growth could primarily occur in the bottom and flat-top regions (they are both *c*-plane), and the epitaxial lateral overgrowth generated to merge the GaN films [15, 16], resulting in the decrease in the dislocation density.

Figures 5(a)–5(c) display the schematics of initial GaN growth modes on FTP-PSS-A, FTP-PSS-B, and FTP-PSS-C, respectively [17]. As discussed in Figure 2, the FTP-PSS-C possessed a largest pattern size, while the FTP-PSS-A had a smallest pattern size. Moreover, the distances between

patterns of these three FTP-PSSs were similar to each other. These reveal that the number of patterns per unit area reduced in the following order: FTP-PSS-A > FTP-PSS-B > FTP-PSS-C. In other words, the area of inclined region in these three PSSs per unit area also decreased in the following order: FTP-PSS-A > FTP-PSS-B > FTP-PSS-C. As described above, a 30 nm thick GaN buffer layer was grown at 530°C, and then the growth temperature was increased to 1150°C. During the heating process, the thin GaN film was gradually transferred to GaN grains. When the subsequent growth was performed at high temperature (1150°C), the GaN epilayer was easily deposited from these GaN grains. Because the FTP-PSS-A possessed the largest area of inclined region (per unit area) compared to that of the other two PSSs, the GaN grains were easily formed in the inclined regions during the heating process. Therefore, the GaN epilayer was easily grown on the inclined regions compared to the bottom *c*-plane regions, as shown in Figure 5(a). However, as shown in Figures 5(b) and 5(c), when the area of inclined region (per unit area) became smaller in FTP-PSS-B and FTP-PSS-C, the initial GaN growth was gradually transferred to GaN on *c*-plane region mode. On the other hand, in the initial growth, the GaN epilayer was also formed on the flat-top region of PSS. Since the FTP-PSS-C had the largest flat-top region area, the GaN film was easily grown on its flat-top regions. On the contrary, the GaN film was more difficultly formed on the flat-top regions of FTP-PSS-A.

The schematics of dislocation behaviors in the GaN epilayers grown on FTP-PSS-A, FTP-PSS-B, and FTP-PSS-C were shown in Figures 5(d)–5(f), respectively [17]. As discussed above, the heights of patterns for these three FTP-PSSs were the same. Meanwhile, the distances between patterns in these three FTP-PSSs were similar to each other. Therefore, the difference in the crystal quality of GaN epilayers grown on FTP-PSS-A, FTP-PSS-B, and FTP-PSS-C could be influenced

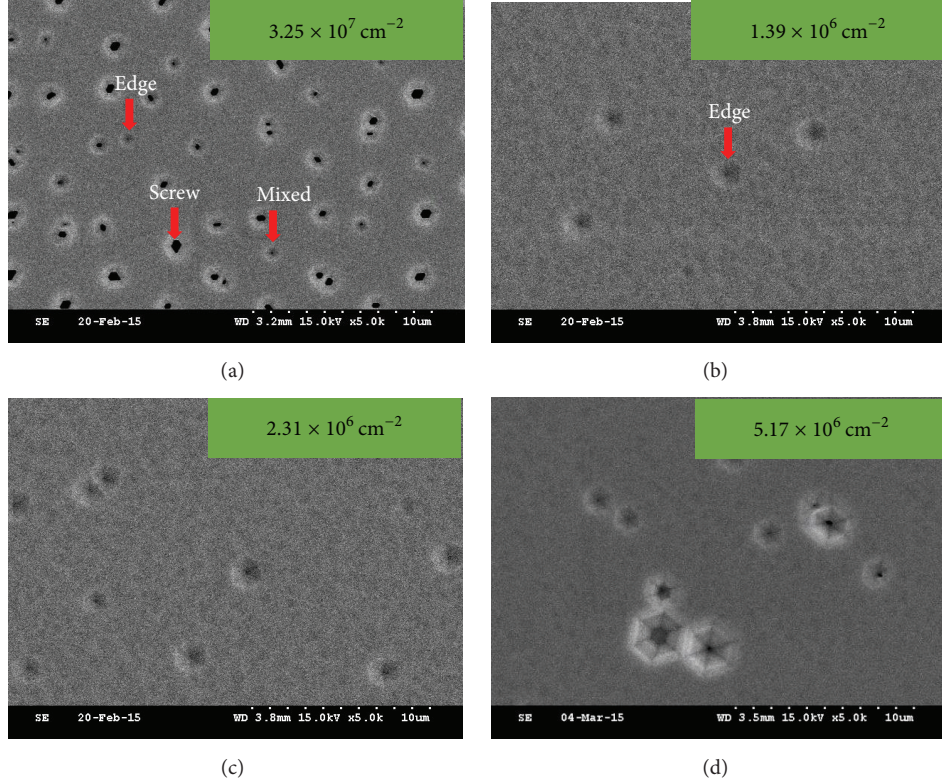


FIGURE 4: SEM images of u-GaN epilayers grown on (a) CSS, (b) FTP-PSS-A, (c) FTP-PSS-B, and (d) FTP-PSS-C after soaking the samples into the  $\text{H}_2\text{SO}_4 : \text{H}_3\text{PO}_4$  (3:1) mixed solution at 250°C for 10 min.

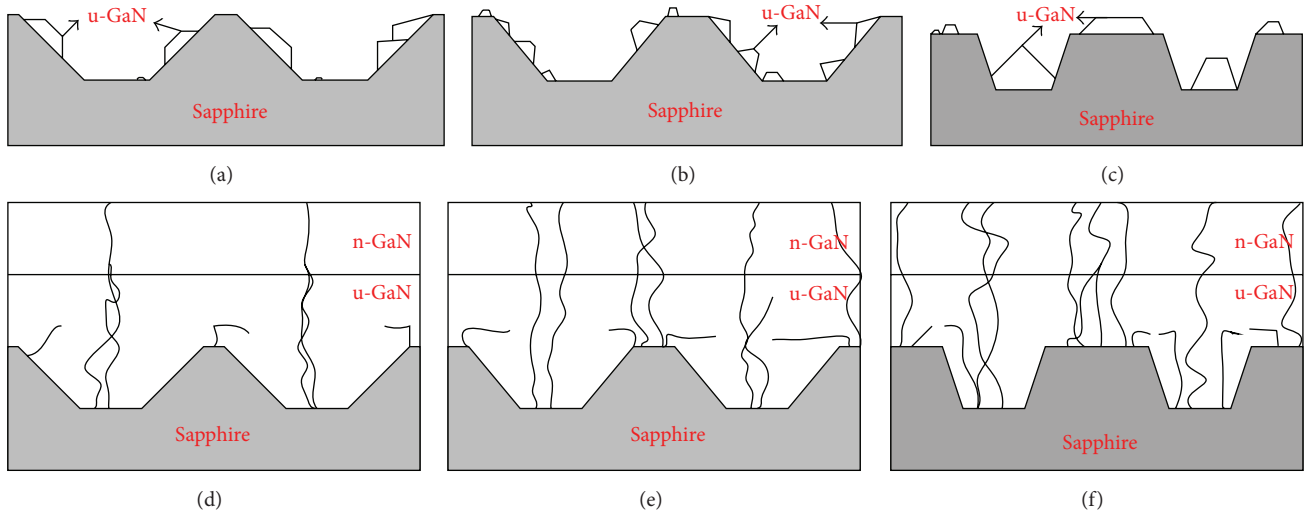


FIGURE 5: Schematic illustrations of the initial GaN growth modes on (a) FTP-PSS-A, (b) FTP-PSS-B, and (c) FTP-PSS-C. Schematic of the evolutions of dislocation behaviors in the GaN epilayers grown on (d) FTP-PSS-A, (e) FTP-PSS-B, and (f) FTP-PSS-C.

by the flat-top region area. Because the FTP-PSS-A possesses the smallest *c*-plane area of flat-top region, the number of dislocations formed at the initial stage is the least, causing the highest crystal quality of GaN epilayer grown on this PSS. On the contrary, due to the largest *c*-plane area of flat-top region formed in the FTP-PSS-C, the GaN epilayer prepared on this

PSS has a relatively low crystal quality as compared with that on the other PSSs.

Figure 6 shows the SpeCLED-Ratro simulation results for the LEDs. During the simulation, a 350 mW power was used to emit randomly from the MQW region. As shown in Figure 6(a), the simulated output power and LEE of the LED

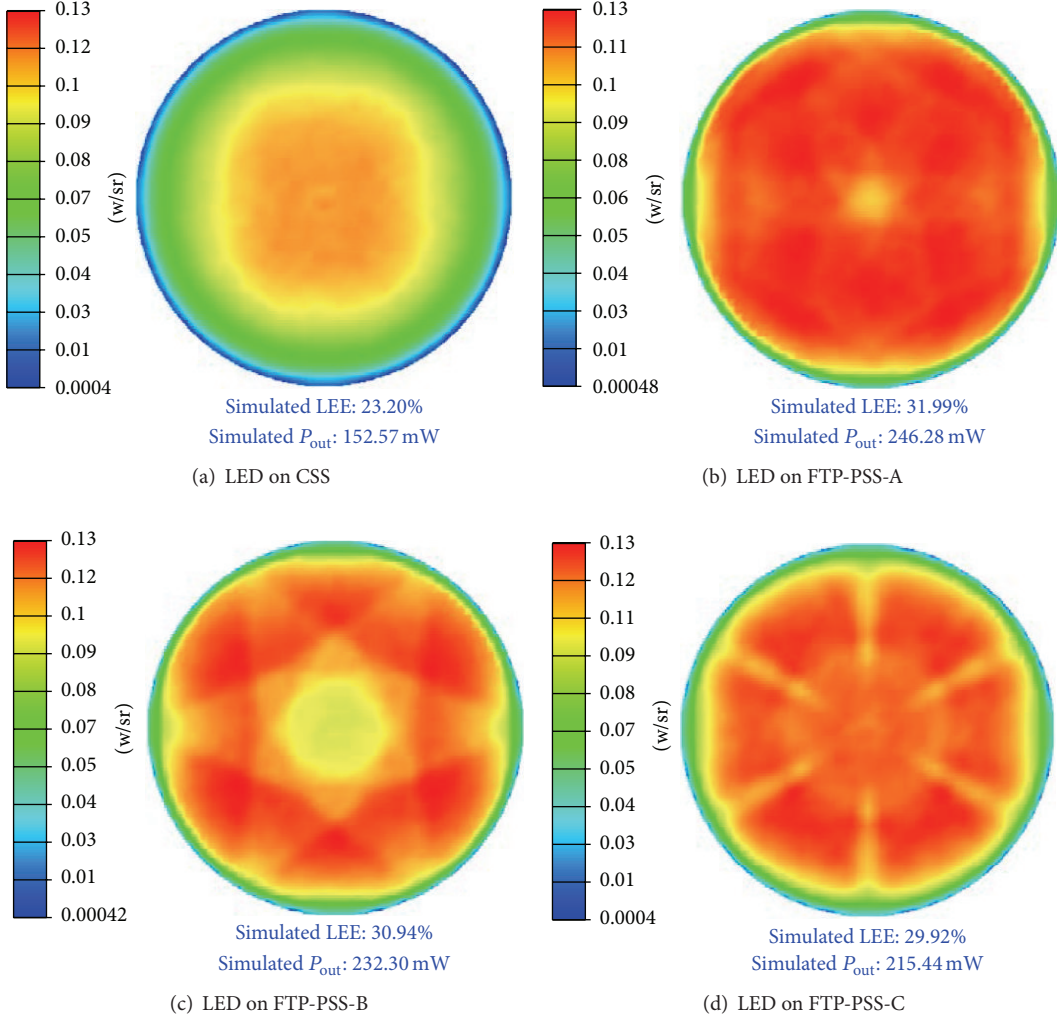


FIGURE 6: SpeCLED-Ratio simulation results for the LEDs fabricated on (a) CSS, (b) FTP-PSS-A, (c) FTP-PSS-B, and (d) FTP-PSS-C.

on CSS were 153 mW and 23.2%, respectively. The simulation results for the LEDs prepared on various FTP-PSSs are shown in Figures 6(b)–6(d). We can observe that the simulated output powers of LEDs on FTP-PSS-A, FTP-PSS-B, and FTP-PSS-C were increased to 246, 232, and 215 mW; meanwhile, the simulated LEEs of these LEDs were enhanced to 32.0%, 30.9%, and 29.9%, respectively. The results present that the LED prepared on the FTP-PSS-A possesses the highest LEE than that of the other samples.

Figure 7 displays the  $I$ - $V$  characteristics of the LEDs fabricated on CSS, FTP-PSS-A, FTP-PSS-B, and FTP-PSS-C. Although the forward voltages of these four devices measured at the whole injection currents (0–1050 mA) are similar to each other, there is a slight difference in the forward voltages of LEDs fabricated on CSS and FTP-PSSs. At an injection current of 350 mA, the forward voltages of the LEDs prepared on the CSS, FTP-PSS-A, FTP-PSS-B, and FTP-PSS-C are measured to be 3.27, 3.22, 3.25, and 3.27 V, respectively. Further increasing the injection current to 1050 mA, the forward voltages of these four devices were 4.30, 4.19, 4.26,

and 4.28 V, respectively. This indicates that the crystal quality of GaN epilayer also affects the  $I$ - $V$  characteristic of LED. Apparently, the higher the crystal quality is obtained in the GaN epilayer, the lower the forward voltage can be achieved in the LED.

Figure 8 shows the light output powers as a function of injection current for these four LED samples fabricated on the CSS and various FTP-PSSs. The light emission images (at 20 mA) of these four LEDs are shown in the inset. Obviously, the light emission intensity of LED on FTP-PSS is much higher than that on CSS. The output powers (at 350 mA) of LEDs prepared on CSS, FTP-PSS-A, FTP-PSS-B, and FTP-PSS-C were 157, 254, 241, and 233 mW, respectively. In comparison to the LED on CSS, there are 61.8%, 53.5%, and 48.4% enhancements in the output power (at 350 mA) for the devices on FTP-PSS-A, FTP-PSS-B, and FTP-PSS-C, respectively. As the injection current was increased to 1050 mA, the output powers of these four LEDs were 371, 581, 543, and 505 mW, respectively. Based on the above-mentioned results, the use of FTP-PSS can both enhance the

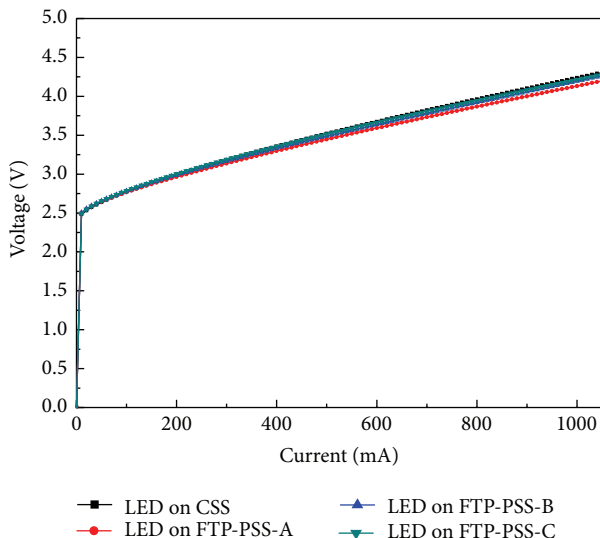


FIGURE 7: *I-V* characteristics of the LEDs fabricated on CSS and various FTP-PSSs.

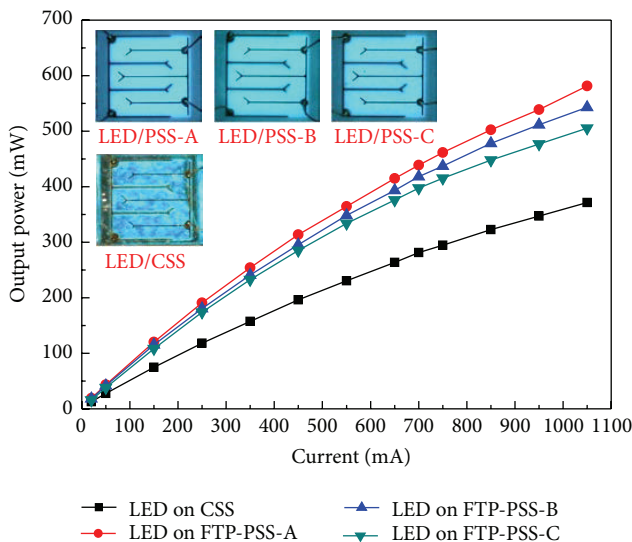


FIGURE 8: Light output powers as a function of injection current for the LEDs fabricated on CSS and various FTP-PSSs.

epilayer quality and increase the light extraction of LED. In particular, for the LED fabricated on FTP-PSS-A, it reveals that this device has better optoelectronic performances.

#### 4. Conclusion

In summary, by performing the sequential wet etching processes, the FTP-PSSs have been prepared for the fabrication of GaN-based blue LEDs. The influence of the flat-top region area of FTP-PSS on the LED performance was analyzed. After fabricating the LEDs on FTP-PSSs, the optoelectronic performance of device was enhanced remarkably as compared with that prepared on CSS. Particularly, for the use of FTP-PSS-A, the crystal quality of GaN epilayer and the light extraction in the LED were both improved most obviously. At an injection

current of 350 mA, the output power of LEDs prepared on CSS was measured to be 157 mW. Additionally, as the LEDs fabricated on FTP-PSS-A, FTP-PSS-B, and FTP-PSS-C, the output powers (at 350 mA) were increased to 254, 241, and 233 mW, respectively. Compared with the LED on CSS, there is 61.8% increment in the output power (at 350 mA) for the devices on FTP-PSS-A.

#### Competing Interests

The authors declare that they have no competing interests.

#### Acknowledgments

This work was supported by the Ministry of Science and Technology of Taiwan under Grant no. 102-2221-E-009-196-MY3, Ministry of Economic Affairs under Contract no. 100-EC-17-A-07-SI-158, 102-E0605, and Hsinchu Science Park under Contracts nos. 103A13 and 104A23.

#### References

- [1] S.-L. Jeng, C.-C. Wu, and W.-H. Chieng, "Gallium nitride electrical characteristics extraction and uniformity sorting," *Journal of Nanomaterials*, vol. 2015, Article ID 478375, 15 pages, 2015.
- [2] G. Wang, X. Duan, and W. Chen, "Barrier thickness and hydrostatic pressure effects on hydrogenic impurity states in wurtzite GaN/ $\text{Al}_x\text{Ga}_{1-x}\text{N}$  strained quantum dots," *Journal of Nanomaterials*, vol. 2015, Article ID 937310, 9 pages, 2015.
- [3] P. C. Chang, K. H. Lee, Z. H. Wang, and S. J. Chang, "AlGaN/GaN high electron mobility transistors with multi- $\text{Mg}_x\text{N}_y/\text{GaN}$  Buffer," *Journal of Nanomaterials*, vol. 2014, Article ID 623043, 4 pages, 2014.
- [4] J. Han, M. H. Crawford, R. J. Shul et al., "AlGaN/GaN quantum well ultraviolet light emitting diodes," *Applied Physics Letters*, vol. 73, no. 12, pp. 1688–1690, 1998.
- [5] A. Y. Polyakov, N. B. Smirnov, E. B. Yakimov, I.-H. Lee, and S. J. Pearton, "Electrical, luminescent, and deep trap properties of Si doped n-GaN grown by pendo epitaxy," *Journal of Applied Physics*, vol. 119, no. 1, Article ID 015103, 2016.
- [6] K. Hiramatsu, K. Nishiyama, M. Onishi et al., "Fabrication and characterization of low defect density GaN using facet-controlled epitaxial lateral overgrowth (FACELO)," *Journal of Crystal Growth*, vol. 221, no. 1–4, pp. 316–326, 2000.
- [7] C.-C. Kao, Y.-K. Su, C.-L. Lin, and J.-J. Chen, "The aspect ratio effects on the performances of GaN-based light-emitting diodes with nanopatterned sapphire substrates," *Applied Physics Letters*, vol. 97, no. 2, Article ID 023111, 2010.
- [8] R.-M. Lin, Y.-C. Lu, S.-F. Yu et al., "Enhanced extraction and efficiency of blue light-emitting diodes prepared using two-step-etched patterned sapphire substrates," *Journal of the Electrochemical Society*, vol. 156, no. 11, pp. H874–H876, 2009.
- [9] J.-H. Cheng, Y. S. Wu, W.-C. Liao, and B.-W. Lin, "Improved crystal quality and performance of GaN-based light-emitting diodes by decreasing the slanted angle of patterned sapphire," *Applied Physics Letters*, vol. 96, no. 5, Article ID 051109, 2010.
- [10] H. Gao, F. Yan, Y. Zhang, J. Li, Y. Zeng, and G. Wang, "Improvement of the performance of GaN-based LEDs grown on sapphire substrates patterned by wet and ICP etching," *Solid-State Electronics*, vol. 52, no. 6, pp. 962–967, 2008.

- [11] D. S. Wuu, W. K. Wang, K. S. Wen et al., "Defect reduction and efficiency improvement of near-ultraviolet emitters via laterally overgrown GaN on a GaN/patterned sapphire template," *Applied Physics Letters*, vol. 89, no. 16, Article ID 161105, 2006.
- [12] J.-H. Lee, J. T. Oh, Y. C. Kim, and J.-H. Lee, "Stress reduction and enhanced extraction efficiency of GaN-based LED grown on cone-shape-patterned sapphire," *IEEE Photonics Technology Letters*, vol. 20, no. 18, pp. 1563–1565, 2008.
- [13] B. Heying, X. H. Wu, S. Keller et al., "Role of threading dislocation structure on the x-ray diffraction peak widths in epitaxial GaN films," *Applied Physics Letters*, vol. 68, no. 5, pp. 643–645, 1996.
- [14] T. Hino, S. Tomiya, T. Miyajima, K. Yanashima, S. Hashimoto, and M. Ikeda, "Characterization of threading dislocations in GaN epitaxial layers," *Applied Physics Letters*, vol. 76, no. 23, pp. 3421–3423, 2000.
- [15] L. Lu, Z. Y. Gao, B. Shen et al., "Microstructure and origin of dislocation etch pits in GaN epilayers grown by metal organic chemical vapor deposition," *Journal of Applied Physics*, vol. 104, no. 12, Article ID 123525, 2008.
- [16] H. Lahreche, P. Vennégùès, B. Beaumont, and P. Gibart, "Growth of high-quality GaN by low-pressure metal-organic vapour phase epitaxy (LP-MOVPE) from 3D islands and lateral overgrowth," *Journal of Crystal Growth*, vol. 205, no. 3, pp. 245–252, 1999.
- [17] H.-C. Lin, H.-H. Liu, G.-Y. Lee et al., "Effects of lens shape on GaN grown on microlens patterned sapphire substrates by metallorganic chemical vapor deposition," *Journal of the Electrochemical Society*, vol. 157, no. 3, pp. H304–H307, 2010.

## Research Article

# Characterization of Al-Doped ZnO Transparent Conducting Thin Film Prepared by Off-Axis Magnetron Sputtering

**Sin-Liang Ou,<sup>1</sup> Feng-Min Lai,<sup>1</sup> Lun-Wei Yuan,<sup>2</sup> Da-Long Cheng,<sup>2</sup> and Kuo-Sheng Kao<sup>2</sup>**

<sup>1</sup>*Department of Materials Science and Engineering, Da-Yeh University, Changhua 515, Taiwan*

<sup>2</sup>*Department of Computer and Communication, SHU-TE University, Kaohsiung 824, Taiwan*

Correspondence should be addressed to Kuo-Sheng Kao; kks@stu.edu.tw

Received 31 March 2016; Revised 21 June 2016; Accepted 14 July 2016

Academic Editor: Ying-Lung D. Ho

Copyright © 2016 Sin-Liang Ou et al. This is an open access article distributed under the Creative Commons Attribution License, which permits unrestricted use, distribution, and reproduction in any medium, provided the original work is properly cited.

The off-axis sputtering technique was used to deposit Al-doped ZnO (AZO) films on glass substrates at room temperature. For the illustration of the sample position in the sputtering chamber, the value of  $R/r$  is introduced. Here,  $r$  is the radius of AZO target and  $R$  is the distance between the sample and the center of substrate holder. A systematic study for the effect of deposition parameters on structural, optical, and electrical properties of AZO films has been investigated in detail. As the sample position of  $R/r$  is fixed at 1.8, it is found that the as-deposited AZO film has relatively low resistivity of  $2.67 \times 10^{-3} \Omega\text{-cm}$  and high transmittance above 80% in the visible region. Additionally, after rapid thermal annealing (RTA) at  $600^\circ\text{C}$  with  $\text{N}_2$  atmosphere, the resistivity of this AZO film can be further reduced to  $1.19 \times 10^{-3} \Omega\text{-cm}$ . This indicates the AZO films prepared by off-axis magnetron sputtering and treated via the appropriate RTA process have great potential in optoelectronic applications.

## 1. Introduction

Recently, transparent conducting oxides (TCOs) are commonly used for a wide range of applications consisting of solar cells, flat panel displays, touch panels, and light-emitting diodes. Among many TCO materials, ZnO has gained a lot of attention owing to its advantages including nontoxicity, low cost, and highly thermal stability [1, 2]. However, regarding to the above-mentioned applications, the conductivity of ZnO is not good enough and requires improving. To solve this problem, there have been several researches focused on the doping into ZnO, and it confirms that the conductivity of ZnO is indeed enhanced by doping with various elements such as F, Al, and Ga [3–5]. Particularly, among these ZnO-based materials, Al-doped ZnO (AZO) thin films have attracted more interest because of their relatively low electrical resistivity and high optical transmittance [6]. On the other hand, ZnO-based films can be grown by many deposition techniques consisting of sputtering [7], evaporation [8], chemical vapor deposition [9], spin coating [10], sol-gel [11], spray pyrolysis [12], and so on. Among these methods, sputtering is widely employed because the

deposited films usually possess plenty of advantages, such as good adhesion, high uniformity in thickness, and high film density. Nevertheless, the bombardment formed on the film is a serious drawback of sputtering technique. At present, to reduce the effect of bombardment during the film deposition, the off-axis sputtering technique has been proposed [13, 14].

In this study, the off-axis sputtering was used to grow AZO thin films. In the off-axis sputtering system, the value of  $R/r$  was defined to depict the sample position in the chamber. By investigating the effect of  $R/r$  value on the characteristics of AZO films, a more suitable sample position for the AZO deposition was obtained. Moreover, the AZO films were further treated by rapid thermal annealing (RTA). Via the modifications of the sample position and the annealing conditions, the AZO films prepared with the optimal parameters can possess better optoelectronic characteristics.

## 2. Experimental Procedure

In our work, the AZO thin films were deposited by radio frequency magnetron sputtering on Corning 1737 glass substrates at room temperature. During the deposition process,

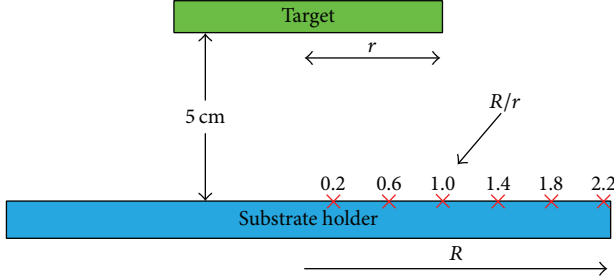


FIGURE 1: Schematic illustration of the sample position in the sputtering chamber.

a homemade AZO ceramic target (98 wt.% ZnO and 2 wt.% Al<sub>2</sub>O<sub>3</sub>) of 2-inch diameter was used. The vertical distance between the target and the substrate holder was fixed at 5 cm. In order to illustrate the sample position, we defined the value of  $R/r$  in the sputtering chamber, where  $r$  is the radius of AZO target and  $R$  is the distance between the sample and the center of substrate holder, as shown in Figure 1. When the off-axis sputtering technique was used to grow the AZO films, the substrates were placed at six positions with various  $R/r$  values of 0.2, 0.6, 1.0, 1.4, 1.8, and 2.2, respectively. By varying the value of  $R/r$ , the influence of the geometry inside the chamber on the AZO properties can be realized. As the base pressure was less than  $7.5 \times 10^{-5}$  Pa, the 60 sccm pure Ar gas was introduced into the sputtering chamber, and the working pressure for the AZO growth was kept at  $7 \times 10^{-1}$  Pa. The sputtering power of AZO target and the deposition time were maintained at 100 W and 60 min, respectively. Except for the sample position in the chamber, the annealing conditions including the temperature and the ambient atmosphere also can be changed to reach better characteristics of AZO films. In the annealing process, the RTA equipment with a heating rate of 5°C/s was used. The as-deposited AZO films were annealed at various temperatures ranging from 200 to 600°C for 1 min. In addition, three ambient atmospheres consisting of air, N<sub>2</sub>, and vacuum were adopted in the annealing process.

Structural, optical, electrical, and morphological properties of the AZO films prepared with various parameters were characterized. The growth orientation of the AZO film was analyzed by X-ray diffraction (XRD, Philips X'PertMRD). Scanning electron microscopy (SEM, JEOL JSM-7001F) was employed to investigate the film's morphology and thickness. The electrical properties such as resistivity, mobility, and carrier concentration of AZO samples were characterized in Van Der Pauw configuration by a Hall analyzer (Accent HL5500/5580). The transmittance spectra of AZO films were measured by an UV-Vis-NIR spectrometer (V-570, JASCO).

### 3. Results and Discussion

The crystal structures of AZO films deposited on glass substrates were examined by XRD. Figure 2 shows the results of XRD  $\theta$ - $2\theta$  scan for AZO films placed at various positions with  $R/r$  values of 0.2–2.2, where  $2\theta$  is increased from 20° to 60°. It can be observed that there is no diffraction peak appearing in the XRD pattern for the sample at the position

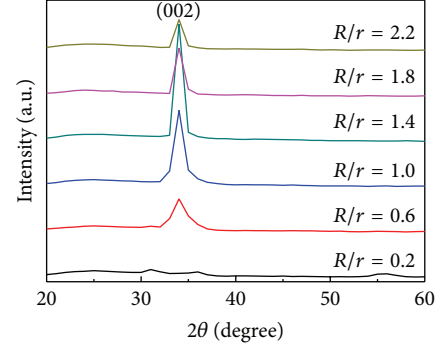


FIGURE 2: XRD patterns of AZO thin films prepared at various sample positions of  $R/r = 0.2$ –2.2.

of  $R/r = 0.2$ , indicating this AZO film possesses amorphous phase. Moreover, by changing the sample position of  $R/r$  from 0.6 to 2.2, only the ZnO(002) diffraction peak can appear in the patterns of these AZO films, which reveals the *c*-axis preferred orientation growth is dominated due to the self-texturing phenomenon [15]. Besides, when the sample positions of  $R/r$  were set at 1.0–1.8, the intensity of ZnO(002) diffraction peak of these AZO films is obviously higher than that of the others.

Figures 3(a)–3(f) display the plan-view SEM images of the sputtered AZO samples placed at the positions of  $R/r = 0.2$ , 0.6, 1.0, 1.4, 1.8, and 2.2, respectively. When the position of  $R/r$  was fixed at 1.4, it can be seen that the AZO film had the largest grain size. Based on Scherrer's formula, the full width at half maximum (FWHM) of XRD peak is corresponding to the crystalline grain size [16]. This indicates the thin film with the most intense XRD peak possesses the largest grain size. The results observed in the plan-view SEM images agree well with those of the XRD patterns, as shown in Figure 2. Figure 4 shows the cross-sectional SEM images of AZO films prepared by putting the samples at various positions ( $R/r = 0.2$ –2.2). According to our observation, as the sample positions of  $R/r$  are kept at 0.2, 0.6, 1.0, 1.4, 1.8, and 2.2, the thicknesses of AZO films are determined to be 631, 607, 506, 461, 336, and 263 nm, respectively. This reveals that the AZO film's thickness decreases with increasing the  $R/r$  value. When the  $R/r$  value is smaller, the moving distance of the ions generated from a target is relatively shorter, and more atoms can arrive at the substrate surface. Thus, this AZO film (at the smaller  $R/r$  value) is relatively thicker. On the contrary, at the larger  $R/r$  value, the AZO film becomes thinner, resulting from the arrival of less atoms at the substrate surface.

The transmittance of the AZO thin film was analyzed by UV-Vis-NIR spectrometer with a wavelength range from 200 to 2500 nm. Figure 5 shows the transmittance spectra of these AZO films prepared by putting the samples at various positions ( $R/r = 0.2$ –2.2). It is apparent that all AZO films exhibit high transmittance in the wavelength range of 400–1200 nm. As the measured wavelength is higher than 1200 nm, the transmittance spectra of these films all present a decreasing tendency. Even so, the high transmittance above 80% in the visible region still confirms that all AZO films are potentially useful in plenty of optoelectronic applications.

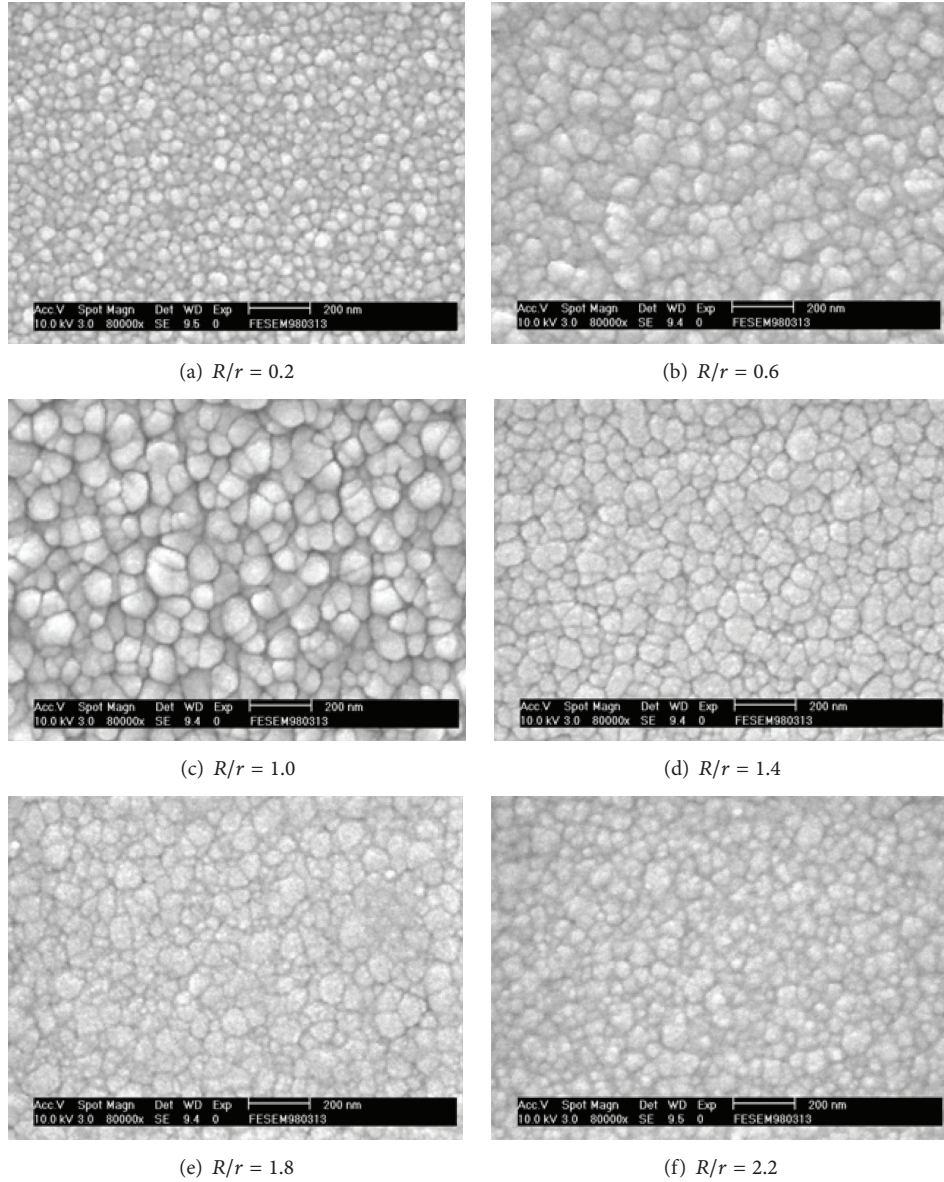


FIGURE 3: Plan-view SEM images of AZO thin films prepared at various sample positions ( $R/r$ ) of (a) 0.2, (b) 0.6, (c) 1.0, (d) 1.4, (e) 1.8, and (f) 2.2.

Figure 6 shows the variations in the resistivity, mobility, and carrier concentration of AZO thin films as a function of sample position ( $R/r$ ). When the  $R/r$  value was set to 0.6, a relatively higher resistivity ( $3.97 \Omega\text{-cm}$ ) of this AZO film was measured. By changing the sample position of  $R/r$  from 0.6 to 1.8, the resistivity of the AZO film gradually reduced. The lowest resistivity of  $2.67 \times 10^{-3} \Omega\text{-cm}$  can be achieved in the AZO film as the sample position of  $R/r$  was set to 1.8. From our observation, the decrease in the resistivity of AZO films can be mainly attributed to the increment in the carrier concentration. The other reason for the decreased resistivity is probably owing to the contribution of Al interstitial atoms in the AZO film. On the other hand, as mentioned above, the unwanted bombardment on the deposited films is a serious disadvantage of the sputtering

technique. The bombardment on ZnO-based films is mainly owing to the generations of energetic O atoms and  $O^-$  ions [17–20]. Tominaga et al. proposed that the bombardment from energetic O atoms or  $O^-$  ions was responsible for the high electrical resistivity of ZnO films [18]. Besides, Nguyen et al. reported that the formation of negative ions from the AZO target was attributed to the surface ionization, resulting from the surface absorption of Al atoms on the AZO target surface [20]. Fortunately, the use of off-axis sputtering technique can reduce the damage caused by negative-ion bombardment to the film growth, leading to an improvement in the electrical conductivity of AZO film. In our research, for the sample at the position of  $R/r = 1.8$ , a better electrical conductivity of AZO film can be achieved, which could also be due to the most efficient reduction in the negative-ion bombardment

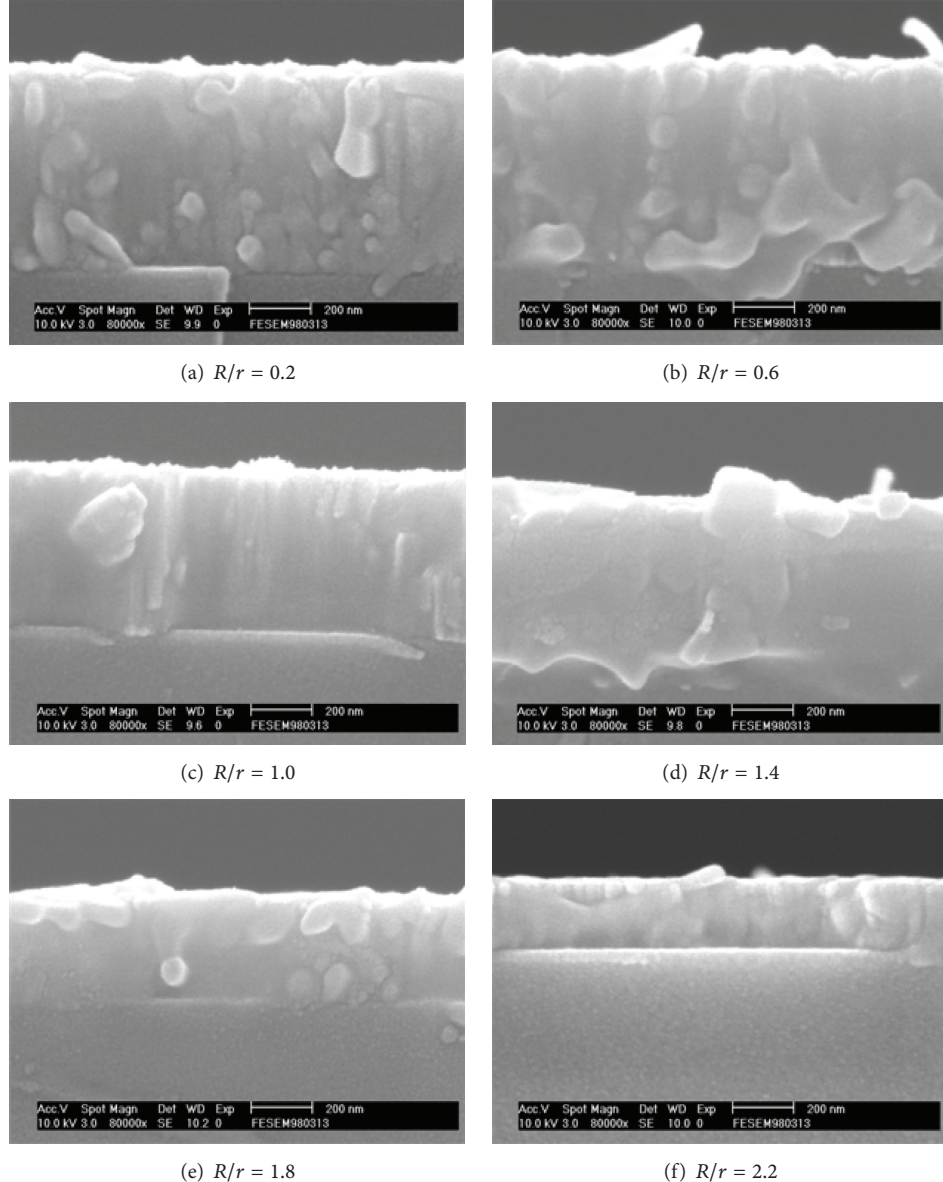


FIGURE 4: Cross-sectional SEM images of AZO thin films prepared at various sample positions ( $R/r$ ) of (a) 0.2, (b) 0.6, (c) 1.0, (d) 1.4, (e) 1.8, and (f) 2.2.

emitted from the AZO target surface. With further changing the sample position of  $R/r$  to 2.2, the resistivity of the AZO film was slightly increased to  $4.54 \times 10^{-3} \Omega\text{-cm}$ . In addition, when the samples were placed at the positions of  $R/r = 0.6$ , 1.0, 1.4, 1.8, and 2.2, the mobility of these AZO films was measured to be  $16.0, 0.1, 3.2, 3.5$ , and  $2.3 \text{ cm}^2/\text{Vs}$ , respectively. Except for the higher mobility of the AZO sample placed at the position of  $R/r = 0.6$  ( $16.0 \text{ cm}^2/\text{Vs}$ ), the other AZO films all exhibit the relatively lower mobility of  $0.1\text{--}3.5 \text{ cm}^2/\text{Vs}$ . The low mobility of these as-deposited AZO films (sample positions of  $R/r = 1.0\text{--}2.2$ ) can be attributed to the excess scattering center.

According to the above-mentioned results, the as-deposited AZO film prepared at the sample position of  $R/r =$

1.8 has a lower electrical resistivity in comparison to the other films. As a result, this AZO film was selected for the RTA annealing treatment. Figure 7 shows the resistivities of AZO films (sample position of  $R/r = 1.8$ ) annealed with various atmospheres consisting of air,  $\text{N}_2$ , and vacuum as a function of annealing temperature. Additionally, the annealing temperatures of 200, 300, 400, 500, and  $600^\circ\text{C}$  were chosen. For the AZO films annealed in the air atmosphere, a relatively lower resistivity of  $5.87 \times 10^{-3} \Omega\text{-cm}$  was obtained at the annealing temperature of  $200^\circ\text{C}$ . However, in comparison to the resistivity of as-deposited AZO film (as shown in Figure 6), it indicates that the resistivity cannot be reduced through the annealing process in the air atmosphere, which is similar to the result proposed in previous research [21].

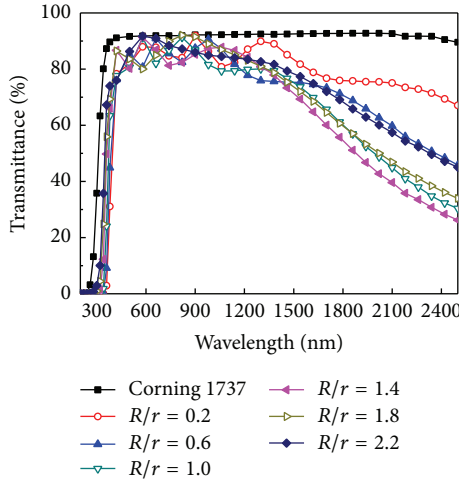


FIGURE 5: Transmittance spectra of AZO thin films prepared by putting the samples at various positions ( $R/r = 0.2\text{--}2.2$ ).

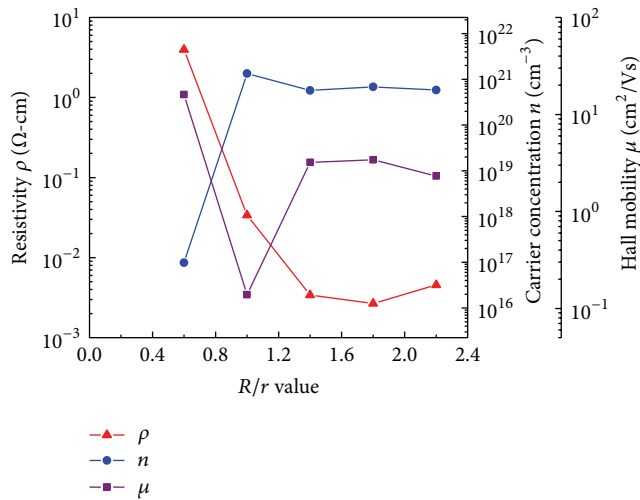


FIGURE 6: Variations in the resistivity, mobility, and carrier concentration of AZO thin films as a function of sample position ( $R/r$ ).

Moreover, as the atmospheres of  $\text{N}_2$  and vacuum were used in the annealing processes, the resistivity of the AZO film can be decreased efficiently, especially for  $600^\circ\text{C}$  annealed AZO films. The low resistivities of  $1.19 \times 10^{-3}$  and  $1.22 \times 10^{-3} \Omega\text{-cm}$  are achieved in  $600^\circ\text{C}$  annealed AZO films with the atmospheres of  $\text{N}_2$  and vacuum, respectively. The results reveal the atmospheres of  $\text{N}_2$  and vacuum are more useful for the improvement in the electrical property of AZO films. The enhancement in the electrical property may be attributed to the fact that the grain boundaries and the crystal lattice deficiencies of the AZO film are reduced with increasing the annealing temperature, leading to an increment in the mobility of the carriers. Additionally, for the ZnO-based materials, it is well known that the oxygen vacancies are mainly responsible for electrons in the conduction band [22]. During the annealing process with the atmosphere of  $\text{N}_2$ , it can be expected that the absorption of oxygen atoms on the

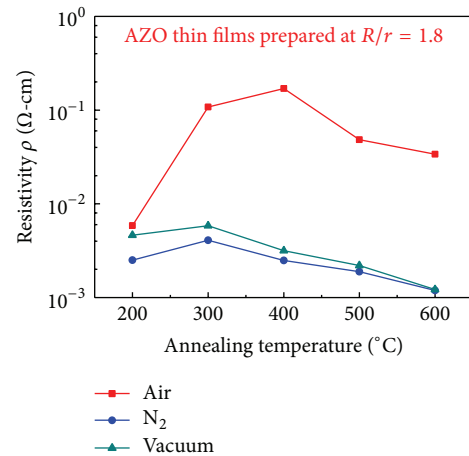


FIGURE 7: Resistivities of AZO thin films (sample position of  $R/r = 1.8$ ) annealed with various atmospheres including air,  $\text{N}_2$ , and vacuum as a function of annealing temperature.

film surface would be reduced, leading to an increment of the oxygen vacancy content. This can explain the better electrical conductivity of  $\text{N}_2$ -annealed AZO films. Based on the results mentioned above, it indicates the electrical conductivity of AZO films can be improved by placing the sample far away from the target, in particular for the sample position of  $R/r = 1.8$ . Furthermore, after RTA annealing at  $600^\circ\text{C}$  with the atmosphere of  $\text{N}_2$ , the optimal electrical property of the AZO film can be obtained. This implies the AZO films deposited by off-axis magnetron sputtering and then treated by RTA annealing in  $\text{N}_2$  atmosphere are highly feasible for applications in optoelectronic devices.

Actually, good electrical and optical properties of AZO films deposited by sputtering (this study) also could be obtained by low-cost chemical solution methods, such as sol-gel [11] and spray pyrolysis [12]. However, it should be mentioned that the sputtered AZO films possessed a higher crystal quality and a smoother surface than those grown by sol-gel and spray pyrolysis. Moreover, it is well known that the sputtering technique is highly compatible with the fabrication processes of modern electronic devices.

#### 4. Conclusion

In summary, the AZO thin films were grown by off-axis radio frequency magnetron sputtering. By changing the relative position of sample ( $R/r = 0.2\text{--}2.2$ ), better electrical conductivity of the AZO film was achieved when the  $R/r$  value was fixed at 1.8. As the atmospheres of  $\text{N}_2$  and vacuum were used in the RTA annealing processes, the electrical conductivity of AZO films can be further enhanced. For the as-deposited AZO film (sample position of  $R/r = 1.8$ ), its resistivity was measured to be  $2.67 \times 10^{-3} \Omega\text{-cm}$  and can be further reduced to  $1.19 \times 10^{-3} \Omega\text{-cm}$  after RTA annealing at  $600^\circ\text{C}$  with the atmosphere of  $\text{N}_2$ . Therefore, via the combination of the off-axis sputtering technique and the RTA annealing process in  $\text{N}_2$  atmosphere, the AZO films have high potential in the optoelectronic applications.

## Competing Interests

The authors declare that there are no competing interests regarding the publication of this paper.

## Acknowledgments

The authors gratefully acknowledge the financial support from the Ministry of Science and Technology, Taiwan (nos. MOST 103-2221-E-366-006, MOST 103-2632-E-366-001, and MOST 104-2632-E-366-001).

## References

- [1] F.-H. Wang, J.-C. Chao, H.-W. Liu, and T.-K. Kang, "Physical properties of ZnO thin films codoped with titanium and hydrogen prepared by RF magnetron sputtering with different substrate temperatures," *Journal of Nanomaterials*, vol. 2015, Article ID 936482, 11 pages, 2015.
- [2] Y. Liu, Y. Li, and H. Zeng, "ZnO-based transparent conductive thin films: doping, performance, and processing," *Journal of Nanomaterials*, vol. 2013, Article ID 196521, 9 pages, 2013.
- [3] H. Y. Xu, Y. C. Liu, R. Mu et al., "F-doping effects on electrical and optical properties of ZnO nanocrystalline films," *Applied Physics Letters*, vol. 86, no. 12, Article ID 123107, 2005.
- [4] P. Banerjee, W.-J. Lee, K.-R. Bae, S. B. Lee, and G. W. Rubloff, "Structural, electrical, and optical properties of atomic layer deposition Al-doped ZnO films," *Journal of Applied Physics*, vol. 108, no. 4, Article ID 043504, 2010.
- [5] T. Yamada, H. Makino, N. Yamamoto, and T. Yamamoto, "Ingrain and grain boundary scattering effects on electron mobility of transparent conducting polycrystalline Ga-doped ZnO films," *Journal of Applied Physics*, vol. 107, no. 12, Article ID 123534, 2010.
- [6] T. Minami, "Transparent conducting oxide semiconductors for transparent electrodes," *Semiconductor Science and Technology*, vol. 20, no. 4, pp. S35–S44, 2005.
- [7] R. Félix, M. Peres, S. Magalhães et al., "The role of edge dislocations on the red luminescence of ZnO films deposited by RF-sputtering," *Journal of Nanomaterials*, vol. 2015, Article ID 970545, 11 pages, 2015.
- [8] G. G. Rusu, A. P. Râmbu, V. E. Buta, M. Dobromir, D. Luca, and M. Rusu, "Structural and optical characterization of Al-doped ZnO films prepared by thermal oxidation of evaporated Zn/Al multilayered films," *Materials Chemistry and Physics*, vol. 123, no. 1, pp. 314–321, 2010.
- [9] N. G. Nguyen, V. T. T. Ho, and L.-S. Hong, "Low-resistivity, high-transmittance Ga:ZnO films prepared through metalorganic chemical vapor deposition using an inexpensive solution of diethylzinc in n-hexane as the Zn precursor," *Applied Physics Letters*, vol. 102, no. 18, Article ID 181912, 2013.
- [10] J. A. Alvarado, A. Maldonado, H. Juarez, and M. Pacio, "Synthesis of colloidal ZnO nanoparticles and deposit of thin films by spin coating technique," *Journal of Nanomaterials*, vol. 2013, Article ID 903191, 9 pages, 2013.
- [11] V. Musat, B. Teixeira, E. Fortunato, R. C. C. Monteiro, and P. Vilarinho, "Al-doped ZnO thin films by sol-gel method," *Surface and Coatings Technology*, vol. 180-181, pp. 659–662, 2004.
- [12] P. P. Sahay and R. K. Nath, "Al-doped ZnO thin films as methanol sensors," *Sensors and Actuators, B: Chemical*, vol. 134, no. 2, pp. 654–659, 2008.
- [13] J. Si, J. Zhao, G. Ding, and H. Wu, "Morphological evolution and growth mechanism of hierarchical structure of PbTe films grown by off-axis magnetron co-sputtering," *Applied Surface Science*, vol. 321, pp. 233–239, 2014.
- [14] Y. H. Kim, D. W. Shin, J. S. Kim et al., "Dielectric properties of composition spread  $\text{SiO}_2\text{-Al}_2\text{O}_3$  mixed phase thin films deposited at room temperature by off-axis RF magnetron sputtering," *Ceramics International*, vol. 38, no. 1, pp. S79–S82, 2012.
- [15] X. Jiang, C. L. Jia, and B. Szyszka, "Manufacture of specific structure of aluminum-doped zinc oxide films by patterning the substrate surface," *Applied Physics Letters*, vol. 80, no. 17, pp. 3090–3092, 2002.
- [16] K. L. Narasimhan, S. P. Pai, V. R. Palkar, and R. Pinto, "High quality zinc oxide films by pulsed laser ablation," *Thin Solid Films*, vol. 295, no. 1-2, pp. 104–106, 1997.
- [17] K. Tominaga, S. Iwamura, Y. Shintani, and O. Tada, "Energy analysis of high-energy neutral atoms in the sputtering of ZnO and  $\text{BaTiO}_3$ ," *Japanese Journal of Applied Physics*, vol. 21, no. 5, pp. 688–695, 1982.
- [18] K. Tominaga, T. Yuasa, M. Kume, and O. Tada, "Influence of energetic oxygen bombardment on conductive ZnO films," *Japanese Journal of Applied Physics*, vol. 24, no. 8, pp. 944–949, 1985.
- [19] G. A. Hirata, J. McKittrick, J. Siqueiros et al., "High transmittance-low resistivity ZnO:Ga films by laser ablation," *Journal of Vacuum Science & Technology A*, vol. 14, no. 3, pp. 791–794, 1996.
- [20] H. C. Nguyen, T. T. Trinh, T. Le et al., "The mechanisms of negative oxygen ion formation from Al-doped ZnO target and the improvements in electrical and optical properties of thin films using off-axis dc magnetron sputtering at low temperature," *Semiconductor Science and Technology*, vol. 26, no. 10, Article ID 105022, 2011.
- [21] G. Sanon, R. Rup, and A. Mansingh, "Growth and characterization of tin oxide films prepared by chemical vapour deposition," *Thin Solid Films*, vol. 190, no. 2, pp. 287–301, 1989.
- [22] X. Zhao, J. Li, H. Li, and S. Li, "Intrinsic and extrinsic defect relaxation behavior of ZnO ceramics," *Journal of Applied Physics*, vol. 111, no. 12, Article ID 124106, 2012.

## Research Article

# Thermal Stresses Analysis and Optimized TTP Processes to Achieved CNT-Based Diaphragm for Thin Panel Speakers

Feng-Min Lai and Chang-Yi Peng

Department of Materials Science and Engineering, Da-Yeh University, Changhua 51591, Taiwan

Correspondence should be addressed to Feng-Min Lai; fengmin@mail.dyu.edu.tw

Received 6 March 2016; Accepted 7 June 2016

Academic Editor: Ying-Lung D. Ho

Copyright © 2016 F.-M. Lai and C.-Y. Peng. This is an open access article distributed under the Creative Commons Attribution License, which permits unrestricted use, distribution, and reproduction in any medium, provided the original work is properly cited.

Industrial companies popularly used the powder coating, classing, and thermal transfer printing (TTP) technique to avoid oxidation on the metallic surface and stiffened speaker diaphragm. This study developed a TTP technique to fabricate a carbon nanotubes (CNTs) stiffened speaker diaphragm for thin panel speaker. The self-developed TTP stiffening technique did not require a high curing temperature that decreased the mechanical property of CNTs. In addition to increasing the stiffness of diaphragm substrate, this technique alleviated the middle and high frequency attenuation associated with the smoothing sound pressure curve of thin panel speaker. The advantage of TTP technique is less harmful to the ecology, but it causes thermal residual stresses and some unstable connections between printed plates. Thus, this study used the numerical analysis software (ANSYS) to analyze the stress and thermal of work piece which have not delaminated problems in transfer interface. The Taguchi quality engineering method was applied to identify the optimal manufacturing parameters. Finally, the optimal manufacturing parameters were employed to fabricate a CNT-based diaphragm, which was then assembled onto a speaker. The result indicated that the CNT-based diaphragm improved the sound pressure curve smoothness of the speaker, which produced a minimum high frequency dip difference ( $\Delta$ dB) value.

## 1. Introduction

The thermal transfer printing (TTP) technique is coating materials to combine on the metallic surface in high thermal environment. This study explores thermal stresses analysis of coating, to make the coating boundary have a good combination, especially. The research of thermal conduction in composite materials is various in the recent years. Ozisik indicated that the composite structures are formed by two or more plates; the connection between any two plates tends to have the problem of thermal resistance [1]. Previous studies have reported that the magnitude and distribution of thermal residual stress can be adjusted by selecting the appropriate material combination and controlling the compositional gradient. Shaw used the multilayer composite plates with different materials to form the elastic module and coating them on different plates and found that different coating thicknesses will influence the characteristics of thermal residual stresses [2]. Özel et al. used the finite element method (FEM) to

simulate various ceramic materials, which are analyzed by their thermal stresses under the very high temperature [3].

Current technological products, including speakers, are mostly lightweight. Speakers have become an integral part of people's everyday life and are prevalently applied in a variety of products such as television, computers, tablet computers, and mobile phones. To fulfill market demands and customer needs for thinner panel speakers with excellent sound quality, problems concerning middle and high frequency attenuation in thin panel speakers must be resolved. The diaphragm in thin panel speaker is the key component of a speaker. The mechanical property of a diaphragm directly influences crucial acoustic characteristics of the speaker (including the sound pressure level (SPL) and frequency range).

Typically, the major material of the diaphragm is coarse paper. However, the lack of stiffness produces unclear sound at middle and high frequency. Therefore, polyethylene naphthalate (PEN) pasted on coarse paper or Al foil pasted on form materials has been studied to enhance the stiffness. However,

poor adhesion and overweight problem occur and limit their application. It is reported that using CNTs as an additive can enhance the mechanical property of resin [4–6]. Compared with regular polymer, CNTs have lower expansion coefficient, which reduces the residual stress in laminated polymer composites. In addition, CNTs have favorable strength and stiffness and are capable of changing material properties such as electrical and thermal conductivity. However, past studies also have observed that mixing high-concentration CNTs with epoxy lowers the mechanical strength of the epoxy, which is primarily attributable to the aggregation of the CNTs and the formation of hollow pores in the epoxy [7, 8]. Regardless, the composite coating containing CNTs and epoxy has not been studied for using as the diaphragm in thin panel speaker.

In this study, we self-developed a TTP technique to prepare the diaphragm in thin panel speaker. TTP is a manufacture through which coatings are bonded to the surface of a transfer material at temperature from 80°C to 120°C [9]. The composite paste of CNTs and epoxy was first roller-pressed onto a polyethylene naphthalate (PEN) substrate to reinforce the PEN, after which the backside of the PEN was coated with hot melt adhesive (HMA). The fabricated TTP paper (CNTs+epoxy/PEN/HMA) was cut into adequate size and shape. Next, a TTP machine was used to locally or fully press TTP paper onto a coarse paper to manufacture a stiffened speaker diaphragm. Bian and Zhao reported that Young's moduli of CNTs decrease when the temperature of the environment exceeds 200°C [10]. In our study, the proposed TTP stiffening technique does not require a high curing temperature that decreases the mechanical property of CNTs, and the TTP technique can stiffen a localized area on a diaphragm substrate, thus increasing diaphragm stiffness without markedly raising diaphragm weight; hence, the inherent strength of CNTs was preserved. The resulting CNT-based diaphragm exhibited increased stiffness, which improved the bandwidth and sound quality of the speaker, thereby markedly improving the overall smoothness of the sound curve. Simultaneously, the weight was reduced and the adhesion was also improved while using the CNT-based diaphragm. Besides, in this study, the Taguchi quality engineering method [11, 12] was used to minimize the number of experimental trials. The paper is relationship among the manufacturing parameters including stiffening pattern, coating direction, transfer area, and transfer temperature of CNT-based diaphragm which have also been therefore investigated.

## 2. Analysis and Experimental Procedure

**2.1. Analysis on ANSYS.** The finite element method (FEM) is used in this study by the assistance of ANSYS PLANE-42 element (Figure 1). PLANE-42 element is used for 2D modeling for solid structures [13]. The element can be used either as a plane element or as an axisymmetric element. The element has plasticity, creep, swelling, stress stiffening, large deflection, and large strain capabilities. The following steps are used to construct our model.

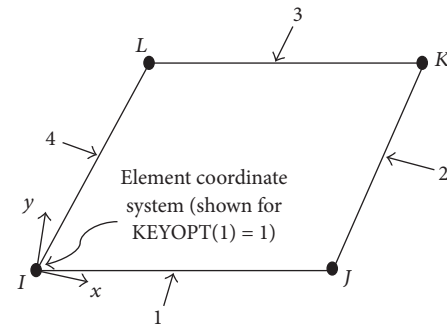


FIGURE 1: PLANE-42 element of ANSYS [13].

- Step 1.* Build the solid structure and the finite element model.
  - Step 2.* Apply loads and obtain the solution.
  - Step 3.* Review the stresses.
  - Step 4.* Perform a design for optimization analysis.

Eventually, PLANE-42 element is applying the 2D module to approximate the 3D module. It can effectively reduce the computation time and accurately analyze the stress values. The element is defined by four nodes having two degrees of freedom at each node and is translated in the nodal  $x$  and  $y$  directions. We can use these data to compute the shift, stress, and angles.

This study assumes that the stress is maximized along  $x$ -axis. First the element type and the property of material are defined to establish the finite element model. Second, the necessary boundary conditions are given and the stresses are resolved. Third,  $\sigma_x$  is maximized for the nodes, which are generated along the interface of the metallic material (base) and the coating material (coating). Finally, the study used ANSYS to analyzed the stress results for CNT-based diaphragm.

**2.2. Fabrication of TTP Paper and CNT-Based Diaphragm.** In this study, a PEN membrane was used as the substrate for fabricating TTP paper. The front and back of the PEN were, respectively, coated with CNT/epoxy and HMA to form the TTP paper. The fabricated TTP paper was then thermally transferred and printed onto a coarse paper to form a diaphragm. Subsequently, the effect of diaphragm fabrication on sound pressure curve smoothness was investigated, and Taguchi quality engineering method was applied to identify the optimal manufacturing parameters.

A PEN membrane was used as the substrate for fabricating TTP paper. We first mixed 2~3 wt% CNTs (CF182C, Advanced Nanopower Inc.) and epoxy (P859-1, Hong Guan R&D Co.) as the CNTs/epoxy composite paste. In fact, the CNTs with a density of  $1.3\sim1.4\text{ g/cm}^3$  (similar to the cotton) are very fluffy and its volume is quite large. Although we have also mixed 4~5 wt% CNTs and epoxy, the experiment result indicates that it requires a much longer mixing time, and the mixture has a high viscosity. This would lead to a

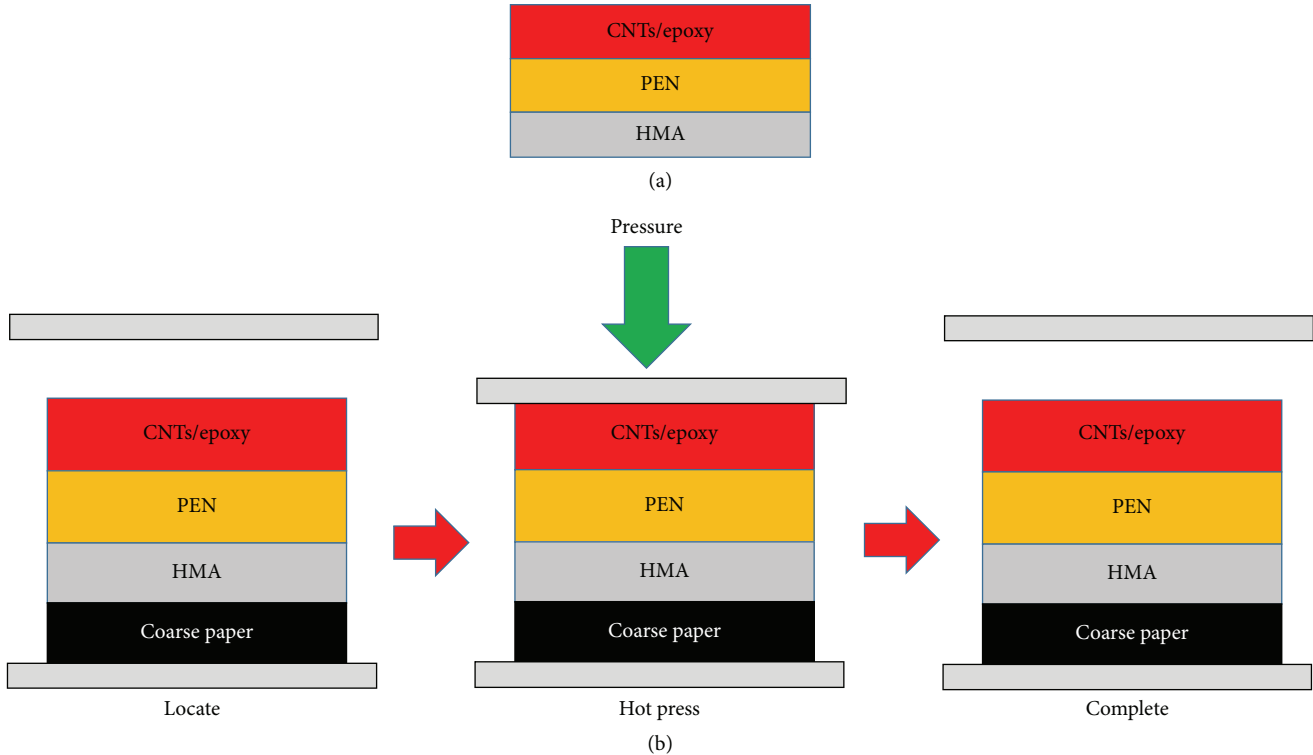


FIGURE 2: Schematic CNT-based diagram of the (a) TTP paper and (b) TTP processes.

nonuniform surface of the TTP paper. As shown in Figure ??, the TTP paper was fabricated by coating the front side of a PEN membrane with CNTs/epoxy paste and then drying it in an oven at 120°C for 15 min. After the CNTs/epoxy coating layer was dried, the backside of PEN was coated with HMA and was dried again in the oven at 80°C for 10 min to obtain a TTP paper. The CNTs/epoxy coating was used to adjust the thickness of TTP paper; in addition, manually roller-pressing the CNTs/epoxy coating onto the TTP paper enabled evenly spreading the coating onto the material surface.

After the fabrication of TTP paper, a TTP process was used to thermally transfer and print the TTP paper onto coarse paper to form a CNT-based diaphragm at an elevated temperature. In this study, as shown in Figure ??, the resulting TTP paper was first stacked onto the coarse paper diaphragm and then subjected to a TTP process in a TTP machine. The following steps of TTP process were illustrated in Figure ???. After pressing to 0.2 kg/cm<sup>2</sup> and heating at 80~120°C for 10 min, the fabrication of CNT-based diaphragm was complete. This study also adopted cold cathode field emission scanning electron microscope (FE-SEM; JEOL JSM-740F, Japan) to observe the cross sections of the CNT-based diaphragm.

**2.3. Material Properties for Test Specimens.** To obtain the properties and strengths of the coarse paper, TTP paper, and CNT-based diaphragm, three types of tensile specimen geometry will be employed. The test specimen dimensions are 12.5 mm × 100 mm. The material properties of laminated

composite face sheets and foam core were determined from experiments conducted in accordance with the relevant ASTM (D3039-79 and D3518-76) standards [14]. The specimens should be mounted and tested in a properly aligned and calibrated INSTRON-1332 test machine. Wedge action friction grips of hydraulic grips will be used. Set the crosshead rate at about 10 mm/min. The strains and load readings may be recorded continuously or at discrete load intervals. If the discrete data are taken, a sufficient number of data points must be recorded in order to reproduce the stress-strain relation. At least 25 data points are needed in the linear response region. Monitor all specimens to failure and then determine the ultimate strengths and strains. Plot the data for reduction. Establish the Young's modulus and Poisson's ratio by a least square fit of the linear region. For finding the mechanical properties and ultimate strengths (strains), some specimens are tested statically to failure. The stress-strain response of tensile coupon is monitored with electrical resistance strain gauge in order to find the intrinsic mechanical properties of the coarse paper, TTP paper, and CNT-based diaphragm. The material properties to be measured include (i) Young's modulus, (ii) Poisson's ratio, (iii) ultimate tensile stress (failure strength).

**2.4. Panel Speaker Assembly.** Figure 3(a) shows the Solid-Works explosion diagram of the panel speaker. After various speaker components were prepared and ready for assembly, the fabricated CNT-based diaphragm was adhered to the speaker surround, which was then assembled to the upper frame as shown in Figure 3(b). The surround material

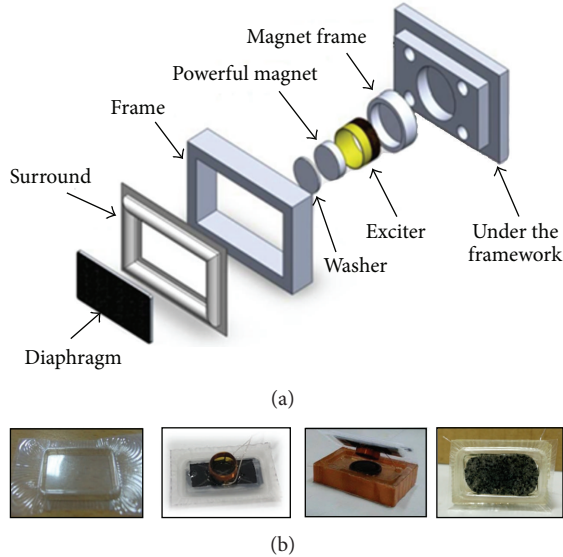


FIGURE 3: (a) SolidWorks explosion diagram of the thin panel speaker; (b) thin panel speaker assembly processes.

selected for our panel speaker was polyurethane (PU) with the actual specification which is  $30 \times 20 \times 10$  mm. PU was placed into a surround mold and heat pressed in an oven to form the speaker surround, which was then attached to the diaphragm and voice coil. Subsequently, the vibration exciter (voice coil) was attached at  $90^\circ$  perpendiculars to the diaphragm. As shown in Figures 3(a) and 3(b), the exciter was placed between the magnet and the magnet frame. The magnets were placed above the washer to increase the magnetic flux. The speaker gives sound through the diaphragm vibration that pushed by the voice coil. Most importantly, the vibration exciter (voice coil) must be attached to the central area of the diaphragm. Otherwise, sound distortion is easily incurred. Once all the steps have been completed, the adhesives were allowed to solidify for a day, after which the sound pressure curve of the speaker can be measured.

**2.5. Sound Pressure Curve Measurement and Analysis.** To avoid influencing the measurement results, sound pressure curve must be measured in an anechoic chamber insulated from external sources of noise; acoustical measurement system and CLIO software analysis were employed in measuring the sound pressure curve. In the CLIO software, the number of points, bandwidth, and voltage were defined. The measured bandwidth was 20 Hz~20 kHz audible to the human ear and was measured at a distance of 10 cm from the self-developed panel speaker. Subsequently, after the input voltage of the speaker was configured, the sound pressure curve and data were measured. In the sound pressure curve, the value difference ( $\Delta$ dB) between curve valley and sound pressure level (SPL) at 12~18 kHz, high frequency dip difference value ( $\Delta$ dB), was used to identify the quality of the sound. A minimum high frequency dip difference value ( $\Delta$ dB) gives a smooth sound pressure curve in the high frequency region and a better sound quality.

**2.6. Taguchi Quality Engineering.** Because stiffening the entire diaphragm may influence the overall sensitivity of the speaker, we attempted to circumvent this problem by performing optimization analysis using the Taguchi method. Through the Taguchi approach, the optimal product design objective or process can be determined to facilitate mitigating the effects of confounding factors [11, 12]. This study investigated the relationship among the manufacturing parameters of CNT-based diaphragm (stiffening pattern, coating layers, transfer area, and heat press temperature), and the Taguchi equations representing the smaller-the-better (see (1)) characteristics are shown as follows:

$$S/N = -10 \log_{10} \frac{\sum_{k=1}^n Y^2 i}{n}. \quad (1)$$

The selected manufacturing parameters of CNT-based diaphragm were aimed at having a minimum high frequency dip difference value ( $\Delta$ dB) in the sound pressure curve of a speaker, subsequently smoothing the sound pressure curve in the high frequency region. Figures 4 and 5 present the parameters obtained from the Taguchi method. Figures 4(a) and 4(b) show the top and side view of the transfer area of the TTP paper on coarse paper, respectively. Figure 5 illustrates the stiffening patterns on the TTP paper and the coating direction of 1 or 2 coating layers. Furthermore, the analysis of variance (ANOVA) was also used to find the dominant influence factors.

### 3. Results and Discussion

**3.1. Comparison of ANSYS and Related Papers for Numerical Example.** The manufacturing parameters of coating materials on a flat plate are the thickness of coating and the order of plates. We compared our ANSYS results with other similar researches. After that, we actually used the ANSYS model for simulation. The material properties of metals and coating materials are shown Table 1.

Shaw [2] indicated that the influencing factors of our analysis are the composition gradient, the elastic module, number of layers, thermal expansion coefficients, and so forth. Shaw used functionally graded materials (FGM) and multilayer composite material on thermal coating and analyzed the thermal residual stress. Since our study was similar to Shaw's results, we compared three materials of metal and ceramic with Shaw's results in Table 2.

Furthermore, Özal et al. [3] coated the advanced ceramic on the metallic plate and minimized the stress as his goal. We also use the stress objective proposed by Özal et al. as our programming goal in this study. And different coating materials,  $Si_3N_4$ ,  $Al_2O_3$ , and TiC are coated on the W metal plate by ANSYS methods so as to compare the thermal stresses with Özal et al.'s results in Table 3. The fluctuation between the analytic results from ANSYS method and published practical results fluctuated from 1.42% to 7.66% with a summarized average 4.31%. Therefore, the paper used the ANSYS method into coarse paper and TTP paper interface shear stress problem. Finally, we compare our ANSYS model

TABLE 1: Material properties of metals and coating materials.

Materials	Properties			
	Young's modulus $E$ (GPa)	Poisson's ratio $\nu$	Thermal conductivity, $K$ (W/m°C)	Coefficient of thermal expansion (CTE), $\alpha$ (1/°C)
Al	70	0.33	34	$2.3 \times 10^{-5}$
W	410	0.28	29	$4.5 \times 10^{-6}$
Diamond	1050	0.20	2	$1.75 \times 10^{-6}$
$\text{Si}_3\text{N}_4$	230	0.26	28	$3.5 \times 10^{-6}$
$\text{Al}_2\text{O}_3$	340	0.23	24	$8.1 \times 10^{-6}$
TiC	340	0.19	27	$7.1 \times 10^{-6}$
NiAl	103	0.17	5.3	$14.6 \times 10^{-6}$

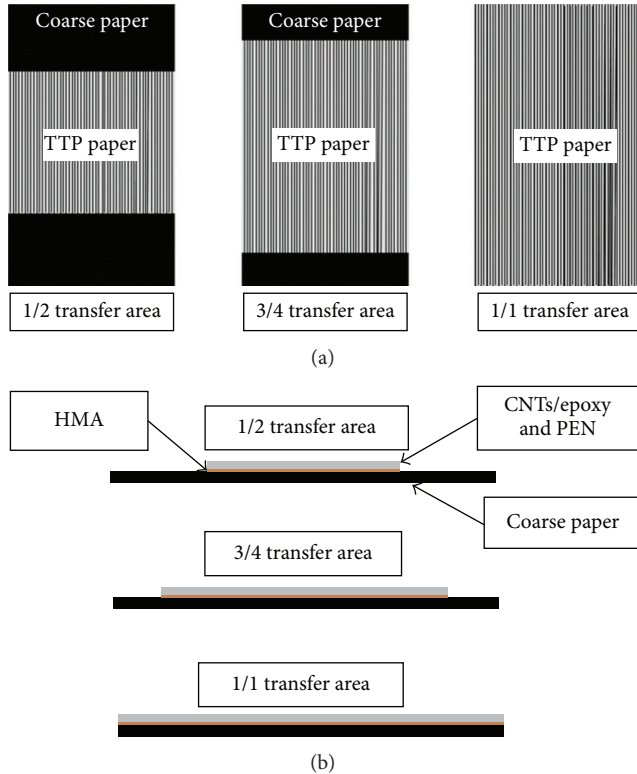


FIGURE 4: (a) Top view of three types of transfer area; (b) side view of three types of transfer area.

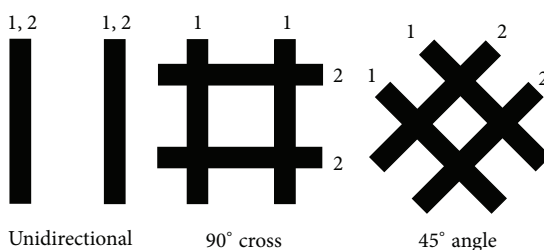


FIGURE 5: Three types of stiffening patterns of the TTP paper. Numbers present the coating direction of patterns containing 1 or 2 coating layers.

TABLE 2: Comparison of Shaw's results and ANSYS.

Material properties	Shaw [2] $\sigma_x (c_g)$	ANSYS method $\sigma_x (c_d)$	Differential $ c_g - c_d /c_g \times 100\%$
I (MPa)	1745	1951.3	11.82%
II (MPa)	1715	1749.1	1.98%
III (MPa)	996.5	914.4	8.23%

TABLE 3: Compare the stresses' decrease progressively with Özal et al.'s results and ANSYS method.

Material properties	Özel et al. [3] $\sigma_x (c_g)$	ANSYS method $\sigma_x (c_d)$	Differential $ c_g - c_d /c_g \times 100\%$
$\text{W} + \text{Si}_3\text{N}_4$	-92%	-95.56%	3.86%
$\text{W} + \text{Al}_2\text{O}_3$	-136%	-125.58%	7.66%
$\text{W} + \text{TiC}$	-121%	-119.27%	1.42%

TABLE 4: Comparing results with Han and Sun's study and ANSYS.

Stress	Methods			
	Han and Sun [15] $\sigma_x (c_g)$	ANSYS method $\sigma_x (c_d)$	Differential $ c_g - c_d /c_g \times 100\%$	
$\sigma_x$ (MPa)	37	41.68	12.64 %	

with Han and Sun's study in Table 4. Han and Sun [15] used the glass and alumini as his test base.

According to the aforementioned comparisons, we can say that our ANSYS model is adequate to approximate the actual thermal coating process. We also believe that the ANSYS model is able to simulate the actual behavior of TTP technology.

**3.2. ANSYS Analyzed the Stress Results for CNT-Based Diaphragm.** The specimens are used by INSTRON-1332 test machine to obtain Young's modulus and strengths of the coarse paper, TTP paper, and CNT-based diaphragm which are shown in Table 5. The study compared CNT-based

TABLE 5: Properties of coarse paper, TTP paper, and CNT-based diaphragm.

Materials	Thicknesses (mm)	Young's modulus $E$ (GPa)	Properties		
			Failure Strength (MPa)	Poisson's ratio $\nu$	CTE, $\alpha$ (1/°C)
Coarse paper ( $C_g$ )	0.210	2.14	32.51	0.28	$2.3 \times 10^{-6}$
TTP Paper	0.027	2.71	48.82	0.33	$25.1 \times 10^{-6}$
CNT-based diaphragm ( $C_d$ )	0.237	2.58	45.12	0.31	—
Differential $ c_g - c_d /c_g \times 100\%$	—	20.56%	26.48%	—	—

TABLE 6: Mechanical properties of CNT-based diaphragm with different TTP curing temperature.

Temperature	Thicknesses (mm)	Properties	
		Young's modulus $E$ (GPa)	Failure strength (MPa)
100°C	0.245	2.23	35.51
120°C	0.237	2.58	41.12
130°C	0.237	2.59	41.08
140°C	0.237	2.57	41.10

TABLE 7: Mechanical properties of TTP papers with different CNTs wt%.

Wt%	Thicknesses (mm)	Properties	
		Young's modulus $E$ (GPa)	Failure strength (MPa)
3 wt%	0.027	2.71	48.82
5 wt%	0.032	2.68	48.75

diaphragm with coarse paper mechanical properties which is increased 20.56% with Young's modulus results in Table 5. This study developed a TTP technique to fabricate a CNTs stiffened coarse paper which could be manufactured speaker diaphragm.

The thermosetting resins with a curing temperature of 120°C were used in this study. After curing at 120°C, a network structure was formed in the resin by intermolecular cross-linking. Moreover, the resin was not softened even though the reheating treatment was performed. Therefore, self-developed TTP stiffening technique does not require high curing temperature. The experiment results on mechanical properties of CNT-based diaphragm with different TTP curing temperature are shown in Table 6. It reveals that the CNT-based diaphragm with the 120°C curing temperature has good mechanical properties. Additionally, the mechanical properties of TTP papers with different CNTs wt% (3 wt% and 5 wt%) are summarized in Table 7. It is obvious that these two TTP papers have almost the same mechanical properties. Therefore, we used 3 wt% CNT/epoxy coating onto the TTP papers which could reduce the cost and has the uniform coating surface.

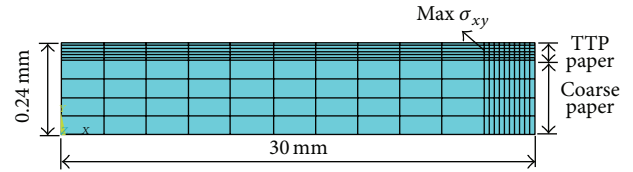


FIGURE 6: Module of finite element method (FEM) with structure of CNT-based diaphragm.

We also believe that the ANSYS model (see Figure 6) is able to simulate the actual behavior of CNT-based diaphragm (model's dimension is 30 × 0.24 mm) with TTP temperature at 80°C, and our simulated results are available in Table 8. The study compared shear stress result with coarse paper and TTP material which is safe in transfer interface. This study used the numerical analysis software (ANSYS) to analyzed the stress and thermal of work piece which have not been delaminated problems in transfer interface. The materials with the higher failure strength could allow the shear stress at high temperatures, which did not produce the peeling problem in the transfer interface.

**3.3. Microscopic Structure of CNT-Based Diaphragm.** Figure 7 presents the sectional images of the CNT-based diaphragm. For a conventional speaker diaphragm fabrication, a PEN pasted on the coarse paper directly. By using the TTP process, as shown in Figures 7(a) and 7(b), the hot melt layer diffuses into the coarse paper and gives an enhanced adhesion. Figure 7(b) shows the enlarged photo of Figure 7(a). On the images, arrows represent the material structure in various regions of the diaphragm. It was observed that CNTs/epoxy coating was evenly applied onto the diaphragm. The coated coarse paper presented more grooves and deeper grooves of uneven depth than the coated PEN paper did, primarily because the coarse paper contained a mixture of fibers. In addition, the FE-SEM images revealed that the CNTs/epoxy coatings on the coarse paper and PEN side of the paper were evenly distributed on the coating material, indicating that the coating was evenly and favorably dispersed. The sectional FE-SEM images show that the TTP paper is tightly bound to the coarse paper substrate, exhibiting an even thickness approximating 269.5 μm.

TABLE 8: Comparing results with ANSYS method and material failure strength.

Shear stress $\sigma_{xy}$ (MPa)	ANSYS analysis result ( $C_A$ )	Coarse paper failure strength ( $C_c$ )	Methods		
			TPP paper failure strength ( $C_T$ )	Differential $ c_c - c_A  / c_A \times 100\%$	Differential $ c_T - c_A  / c_A \times 100\%$
12.2		32.51	48.82	166.3%	299.8%

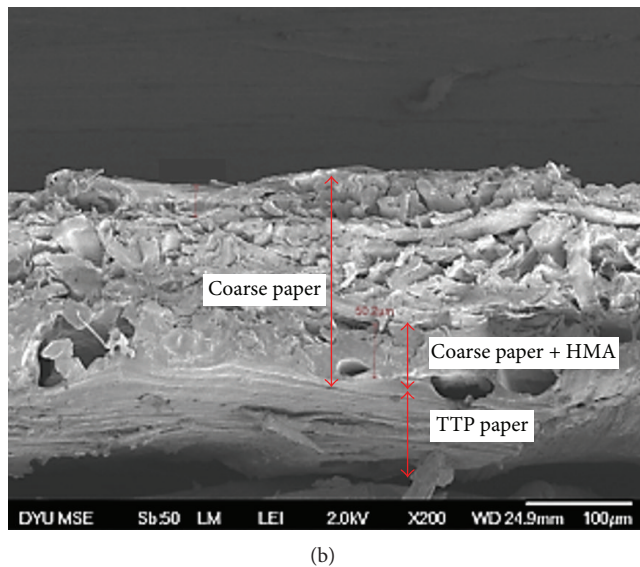
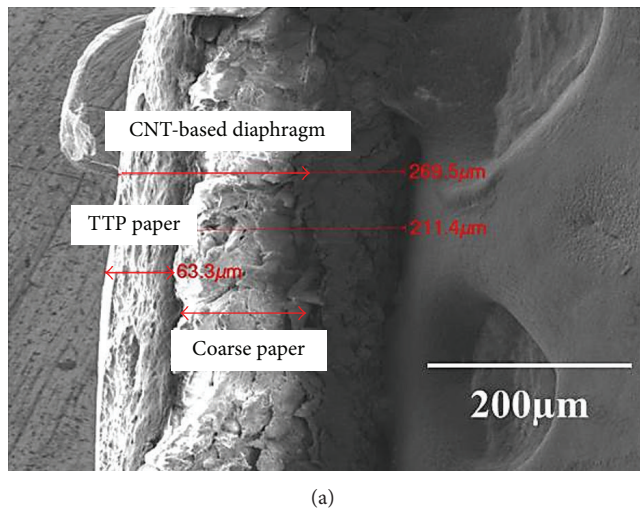
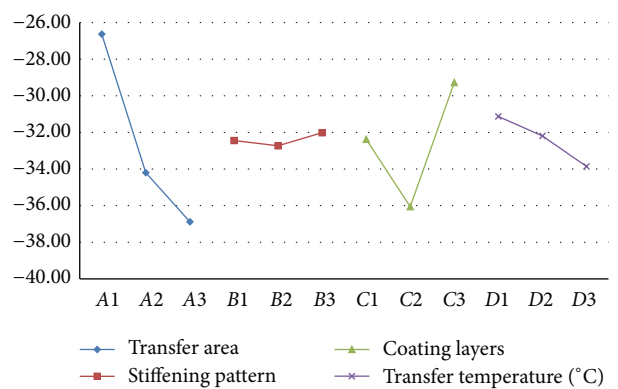


FIGURE 7: FE-SEM sectional images of (a) the self-developed speaker diaphragm. (b) is the enlarged photo of (a).

**3.4. Taguchi Quality Engineering: Optimal High Frequency Dip Difference Value ( $\Delta dB$ ).** This high frequency dip difference value primarily influences the smoothness and bandwidth of the curve; a small valley difference indicates large sound range, which increases the clarity of the speaker's midfrequency and high frequency sounds. Therefore, the minimal high frequency dip difference value is desirable. As shown in Table 9, the Taguchi quality engineering method was used to minimize the number of experimental trials, and the applicable orthogonal array was selected according to the

TABLE 9: Taguchi-selected factors.

	Factors	Level		
		1	2	3
A	Transfer area	1/2	3/4	1/1
B	Stiffening pattern	Unidirectional	90° cross	45° angle
C	Coating layers	No	1 layer	2 layers
D	Transfer temperature	80°C	100°C	120°C

FIGURE 8: Main effect diagram of the high frequency dip difference ( $\Delta dB$ ).

controllable factors and level numbers. To obtain a minimal difference value, the smaller-the-better characteristic was used to determine the optimal manufacturing parameters as listed in Table 10.

Table 11 presents the cause and effect table, showing the ranking of each experimental factor according to its level of contribution. As shown in Figure 8, the main effect diagram reveals that a factor with a steep slope critically influences the overall experimental results. The crucial factors influencing the high frequency dip difference in the sound pressure curve, in order from highest to lowest level of contribution, were transfer area, coating layers, transfer temperature, and stiffening pattern. By using the ANOVA analysis, significant manufacturing parameters can be easily obtained in this study. The criteria of significant manufacturing parameters are cumulating the contribution ratio to 99.8%. The ANOVA analysis for high frequency dip difference was listed in Table 12 and was plotted as in Figure 9. Specifically, the transfer area has the greatest influence (68.5%), followed by the coating layers (25.5%), transfer temperature (4.7%), and stiffening pattern (1.1%). As a result, to obtain the minimal high frequency dip difference value, transfer area and coating layers are the dominant parameters with contribution at 68.5 and 25.5%, respectively.

TABLE 10: Smaller-the-better L<sub>9</sub> orthogonal array.

Number	Factors			D	ΔdB values			SN
	A	B	C		Y <sub>1</sub>	Y <sub>2</sub>	Y <sub>3</sub>	
1	1/2	Unidirectional	No	80	2.62	2.67	2.66	-8.4652
2	1/2	90° cross	1 layer	100	3.19	3.15	3.11	-9.9667
3	1/2	45° angle	2 layers	120	2.59	2.5	2.62	-8.2004
4	3/4	Unidirectional	1 layer	120	4.39	4.42	4.51	-12.948
5	3/4	90° cross	2 layers	80	3.21	3.19	3.14	-10.0489
6	3/4	45° angle	No	100	3.61	3.66	3.62	-11.1983
7	1/1	Unidirectional	2 layers	100	3.56	3.53	3.59	-11.0292
8	1/1	90° cross	No	120	4.31	4.37	4.28	-12.7100
9	1/1	45° angle	1 layer	80	4.27	4.26	4.29	-12.6154

TABLE 11: Cause and effect table of the high frequency dip difference (ΔdB).

Level	Factors			
	A	B	C	D
Level 1	-26.6323	-32.4426	-32.3735	-31.6555
Level 2	-34.1954	-32.7256	-36.0563	-32.1942
Level 3	-36.8806	-32.0140	-29.2785	-33.8586
Influence quantity	10.2483	0.2829	6.7778	2.2031
Ranking	1	4	2	3

TABLE 12: Degree of influence of each factor in terms of percentages for the high frequency dip difference (ΔdB).

Factors	S <sub>k</sub>	V	Influence percentage	Progressive percentage
A Transfer area	18.8267	9.4133	68.5%	68.5%
C Coating layers	7.6756	3.8378	25.5%	94.0%
D Transfer temperature	0.8794	0.4397	4.7%	98.7%
B Stiffening pattern	0.0138	0.0069	1.1%	99.8%

As the optimal manufacturing parameters are not included in the L<sub>9</sub> orthogonal array, the optimal manufacturing parameters to attain a stiffened speaker diaphragm with minimal high frequency dip difference value was determined by selecting the maximum points from the main effect diagram of Figure 8. As a result, the optimal parameter combination obtained using the Taguchi method was 1/2 transfer area, 45° angle ply stiffening pattern, 2 coating layers, and 80°C HMA transfer temperature. The 45° angle ply stiffening pattern has the highest coating area on the PEN surface and leads to a better stiffness. Furthermore, only half area of the diaphragm was coated with CNTs/epoxy composite and the weight of the diaphragm was significantly reduced. Therefore, a CNT-based diaphragm was fabricated using the optimal parameter and named as number 10. Figure 10 compares the sound pressures curve of the speakers produced using two

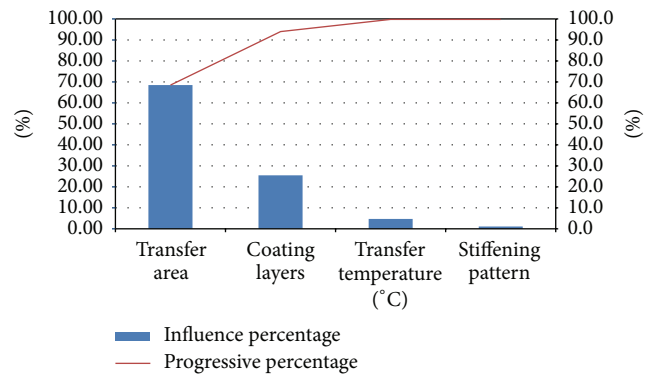


FIGURE 9: Pareto chart of the high frequency dip difference (ΔdB).

different CNT-based diaphragms, number 3 and number 10. The number 3 CNT-based diaphragm exhibits the smallest high frequency dip difference value of the sound pressure curve among the nine diaphragms fabricated form Table 10. The black and red dashed lines and arrows in Figure 10 indicate the high frequency dip difference of number 3 and number 10 diaphragms, respectively. The number 10 CNT-based diaphragm produced a high frequency dip difference (0.98 dB) smaller than that of number 3 diaphragm (2.56 dB), improving the high frequency dip difference by 61.72%. Except high frequency region, number 10 CNT-based diaphragm shows a smaller dip difference at high frequency. As shown in Figure 10, the blue dashed line and arrow indicates the dip difference of number 10 CNT-based diaphragm. As a result, at high frequency region, number 10 CNT-based diaphragm shows a small dip difference and a delayed peak frequency as compared to number 3 CNT-based diaphragm.

Actually, the medium-low frequency and high frequency of voices could be both controlled by Young's modulus and stiffness of CNT-based diaphragms and then show the powerful voices. For panel speakers, the CNT-based diaphragms with a high stiffness would result in clear and smooth sound pressure curve at the 20 Hz~20 kHz. However, the sound properties including the sound pressure curve and the frequency range could be not affected by the strength and the shear stress properties of CNT-based diaphragms.

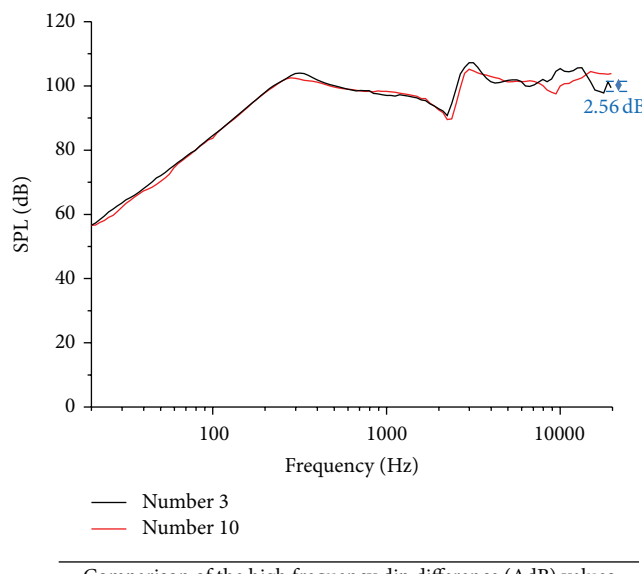


FIGURE 10: Comparison of high frequency dip difference values of the sound pressure curves.

## 4. Conclusion

This study uses laminate plate theory to analyze the thermal transfer printing technology by the assistance of ANSYS. The analytic results from ANSYS method are found to be superior to results from other studies, showing that the proposed hypothesis is valuable. The TTP paper is manufacturing CNT-based diaphragm which has not been delaminated problem in transfer interface for the analytic results from ANSYS method.

Following various experiments and measurements, sound pressure curves were analyzed using the Taguchi method to determine the crucial manufacturing parameters for a TTP technique. The results verified that the CNT-based diaphragm fabricated using the proposed TTP method improved the sound pressure curve smoothness of a panel speaker. Moreover, the Taguchi method was used to effectively identify the optimal manufacturing parameters and the most influential factors. The empirical experiments conducted in this study confirmed that the optimal manufacturing parameters can be used to obtain the minimal high frequency dip difference.

According to the ANOVA analysis, the significant contribution percentage for having the minimal high frequency dip difference was also investigated. For the high frequency dip difference, it was found the transfer area has the greatest influence (68.5%), followed by the coating layers (25.5%), transfer temperature (4.7%), and stiffening pattern (1.1%).

Using the Taguchi quality engineering method, the optimal manufacturing parameters combination for achieving minimum high frequency dip difference composed of a 1/2 transfer area, 45° angle-shaped stiffening pattern, 2 layers of coating, and a transfer temperature of 80°C. It was observed

that the CNT-based diaphragm and TTP technique improved the smoothness of the sound pressure curve, and the optimal manufacturing parameters enabled fabricating a speaker that produced a high frequency dip difference of 0.98 dB (improving the difference values by 61.72%).

## Competing Interests

The authors declare that there are no competing interests regarding the publication of this paper.

## Acknowledgments

The authors would like to thank the Ministry of Science and Technology in Taiwan for financially support of this research project under Grant no. 102-2221-E-212-006.

## References

- [1] M. N. Ozisik, *Heat Conduction*, John Wiley & Sons, New York, NY, USA, 1980.
- [2] L. L. Shaw, "Thermal residual stresses in plates and coatings composed of multi-layered and functionally graded materials," *Composites Part B: Engineering*, vol. 29, no. 3, pp. 199–210, 1998.
- [3] A. Özel, V. Ucar, A. Mimaroglu, and I. Calli, "Comparison of the thermal stresses developed in diamond and advanced ceramic coating systems under thermal loading," *Materials and Design*, vol. 21, no. 5, pp. 437–440, 2000.
- [4] F. Gardea and D. C. Lagoudas, "Characterization of electrical and thermal properties of carbon nanotube/epoxy composites," *Composites Part B: Engineering*, vol. 56, pp. 611–620, 2014.
- [5] A. Montazeri, J. Javadpour, A. Khavandi, A. Tcharkhtchi, and A. Mohajeri, "Mechanical properties of multi-walled carbon nanotube/epoxy composites," *Materials and Design*, vol. 31, no. 9, pp. 4202–4208, 2010.
- [6] S. M. Park and M. Y. Shon, "Effects of multi-walled carbon nano tubes on corrosion protection of zinc rich epoxy resin coating," *Journal of Industrial and Engineering Chemistry*, vol. 21, pp. 1258–1264, 2015.
- [7] J. M. Wernik and S. A. Meguid, "On the mechanical characterization of carbon nanotube reinforced epoxy adhesives," *Materials and Design*, vol. 59, pp. 19–32, 2014.
- [8] M. M. Shokrieh, A. Daneshvar, and S. Akbari, "Reduction of thermal residual stresses of laminated polymer composites by addition of carbon nanotubes," *Materials and Design*, vol. 53, pp. 209–216, 2014.
- [9] F. M. Lai, "Using ant colony optimization for process variables of thermal transfer printing technology," in *Proceedings of the Asian-Pacific Conference on Aerospace Technology and Science*, vol. 6, pp. 219–227, 2013.
- [10] L. Bian and H. Zhao, "Elastic properties of a single-walled carbon nanotube under a thermal environment," *Composite Structures*, vol. 121, pp. 337–343, 2015.
- [11] K. Z. K. Ahmad, S. H. Ahmad, M. A. Tarawneh, and P. R. Apte, "Evaluation of mechanical properties of epoxy/nanoclay/multi-walled carbon nanotube nanocomposites using taguchi method," *Procedia Chemistry*, vol. 4, pp. 80–86, 2012.
- [12] R. Azadi and Y. Rostamiyan, "Experimental and analytical study of buckling strength of new quaternary hybrid nanocomposite

- using Taguchi method for optimization,” *Construction and Building Materials*, vol. 88, pp. 212–224, 2015.
- [13] ANSYS Mechanical APDL Modeling and Meshing Guide, ANSYS Inc, 2011.
- [14] ASTM, *Astm Standards and Literature References for Composite Materials*, Astm International, West Conshohocken, Pa, USA, 2nd edition, 1990.
- [15] C. Han and C. T. Sun, “A study of pre-stress effect on static and dynamic contact failure of brittle materials,” *International Journal of Impact Engineering*, vol. 24, no. 6-7, pp. 597–611, 2000.

## Research Article

# Structure and Properties of Nanocrystalline $(\text{TiZr})_x\text{N}_{1-x}$ Thin Films Deposited by DC Unbalanced Magnetron Sputtering

Yu-Wei Lin,<sup>1,2</sup> Chia-Wei Lu,<sup>2</sup> Ge-Ping Yu,<sup>2,3</sup> and Jia-Hong Huang<sup>2</sup>

<sup>1</sup>Instrument Technology Research Center, National Applied Research Laboratories, No. 20, R&D Road VI, Hsinchu Science-Based Industrial Park, Hsinchu 300, Taiwan

<sup>2</sup>Department of Engineering and System Science, National Tsing Hua University, Hsinchu 300, Taiwan

<sup>3</sup>Institute of Nuclear Engineering and Science, National Tsing Hua University, Hsinchu 300, Taiwan

Correspondence should be addressed to Yu-Wei Lin; [james722@itrc.narl.org.tw](mailto:james722@itrc.narl.org.tw)

Received 11 November 2015; Revised 1 February 2016; Accepted 11 February 2016

Academic Editor: Ying-Lung D. Ho

Copyright © 2016 Yu-Wei Lin et al. This is an open access article distributed under the Creative Commons Attribution License, which permits unrestricted use, distribution, and reproduction in any medium, provided the original work is properly cited.

This study aims to investigate the effects of nitrogen flow rate (0–2.5 sccm) on the structure and properties of TiZrN films. Nanocrystalline TiZrN thin films were deposited on Si (001) substrates by unbalanced magnetron sputtering. The major effects of the nitrogen flow rate were on the phase, texture, N/(Ti + Zr) ratio, thickness, hardness, residual stress, and resistivity of the TiZrN films. The nitrogen content played an important role in the phase transition. With increasing nitrogen flow rate, the phase changed from mixed TiZr and TiZrN phases to a single TiZrN phase. The X-ray diffraction results indicated that (111) was the preferred orientation for all TiZrN specimens. The N/(Ti + Zr) ratio of the TiZrN films first increased with increasing nitrogen flow rate and then stabilized when the flow rate further increased. When the nitrogen flow rate increased from 0.4 to 1.0 sccm, the hardness and residual stress of the TiZrN thin film increased, whereas the electrical resistivity decreased. None of the properties of the TiZrN thin films changed with nitrogen flow rate above 1.0 sccm because the films contained a stable single phase (TiZrN). At high nitrogen flow rates (1.0–2.5 sccm), the average hardness and resistivity of the TiZrN thin films were approximately 36 GPa and 36.5  $\mu\Omega\cdot\text{cm}$ , respectively.

## 1. Introduction

Since the 1980s, transition metal nitride coatings produced by physical vapor deposition have been widely studied. Binary transition metal nitride films such as TiN and ZrN are often used as protective coatings to enhance the properties of substrate materials. Due to their high hardness and better wear and corrosion resistance, binary transition metal nitride films are widely used in industry. Additionally, transition metal nitrides are used as diffusion barriers in the semiconductor industry [1, 2].

With the rapid development of technology, demands for high-quality films are increasing. Therefore, development of multifunctional ternary transition metal nitride films has begun. Under equivalent deposition conditions, TiZrN coatings not only exhibit corrosion resistance and superior mechanical properties such as lower resistivity, higher adhesion, and lower friction coefficient but also show enhanced

hardness and wear resistance. Due to solid-solution strengthening, these films generally reach maximum hardness when ternary  $\text{Ti}_x\text{Zr}_y\text{N}$  contains 60 at.% Ti [3, 4].

Although preliminary studies on TiZrN films have been conducted in recent years, the properties of TiZrN films have not yet been fully developed; thus, the film properties can be improved by unbalanced magnetron sputtering. DC unbalanced magnetron (UBM) sputtering systems are popular coating systems used to deposit high-quality films of various materials. UBM can reduce the cost of the deposition process [5]. Furthermore, the effect of nitrogen flow rate on the phase transition in TiZrN thin films is worth studying because the phase transformation may change some film properties. Herein, a relatively broad range of process parameters was employed to deposit TiZrN thin films with stable properties. This study primarily aims to investigate the effects of nitrogen flow rate on the structure and properties of TiZrN film depositing using DC unbalanced magnetron sputtering.

TABLE 1: Deposition conditions of TiZrN thin films.

Precoating conditions	
Base vacuum pressure	$6.7 \times 10^{-4}$ Pa ( $5 \times 10^{-6}$ torr)
Bombardment voltage	-1000 V
Bombardment time	5 min
Coating conditions	
Current density	Ti: 0.24 A Zr: 0.24 A
Working pressure	0.17 Pa ( $1.3 \times 10^{-3}$ torr)
Substrate bias	-80 V
Coating temperature	400°C
Deposition time	40 min
Ar flow rate	30 sccm
N <sub>2</sub> flow rate	0~2.5 sccm

## 2. Experiments

TiZrN thin films were deposited on Si substrates using a DC unbalanced magnetron sputtering system. Prior to deposition, the substrate was presputtered in argon atmosphere for 5 min to remove the surface oxide layer. The substrate was subjected to a bias of -1000 V using a power supply, and the argon flow rate was fixed at 50 sccm to clean the substrate surface. The target-to-substrate distance was adjusted to 10 cm. The power supplies of the two targets were operated at 0.24 A. High-purity working and reactive gases were introduced, and mass flow controllers were used to adjust both gases. The flow rate of argon gas (99.9995%) was fixed at 30 sccm with a maximum gas flow rate of 50 sccm. The flow rate of nitrogen gas (99.9995%) was varied from 0 to 2.5 sccm with a maximum gas flow rate of 5 sccm. The negative substrate bias voltage was maintained at -80 V. The coating temperature was 400°C. The deposition conditions for nine samples are listed in Table 1.

The crystal structures of the TiZrN films were determined by X-ray diffraction (XRD) using Cu-K $\alpha$  radiation, and the cross-sectional microstructures of the TiZrN thin films were observed by field-emission gun-scanning electron microscopy (FEG-SEM). The surface compositions of TiZrN thin films were determined by X-ray photoelectron spectroscopy under a vacuum of  $10^{-10}$  torr. The electrical resistivities of the TiZrN film were measured using a four-point probe, and the hardness values were determined by nanoindentation. The residual stress of the specimen deposited on silicon was determined by a laser curvature measurement system that measured the curvatures of a specimen before and after film deposition. The colorations of the TiZrN thin films were examined at room temperature using a Hunterlab MiniScan XE Plus spectrophotometer (Model 4000VSAV).

## 3. Results and Discussion

**3.1. Structure.** The chemical compositions, crystal structures, residual stresses, and mechanical properties of the TiZrN thin films are summarized in Tables 2 and 3.

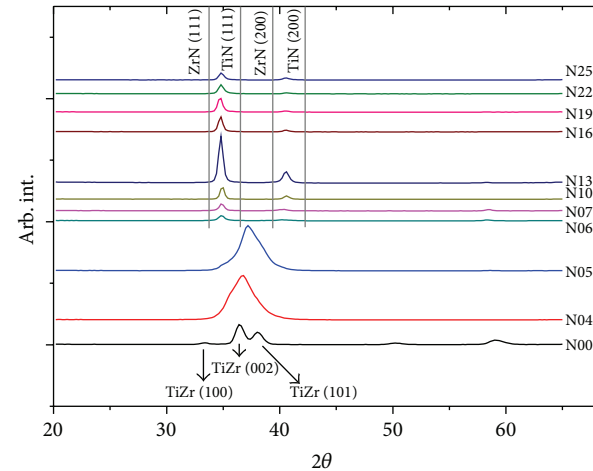


FIGURE 1: XRDs pattern of TiZrN films deposited at different various flow rates.

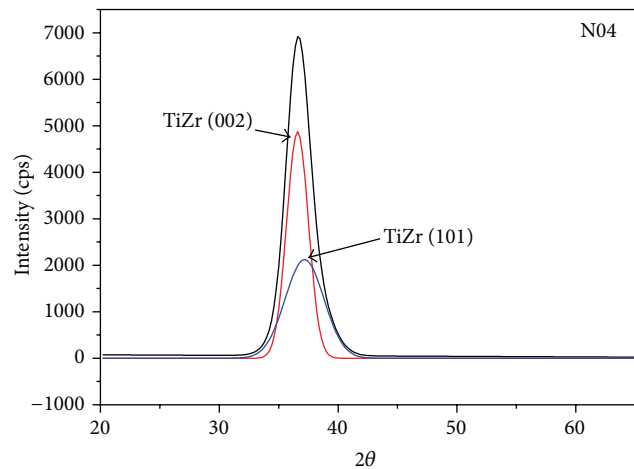


FIGURE 2: Deconvolution patterns of the N04 specimen.

All reflection peaks of TiZr were observed between the Ti and Zr peaks in the XRD patterns. Similarly, all reflection peaks of TiZrN were observed between the peaks of TiN and ZrN. Figure 1 shows the XRD patterns of the films deposited at different nitrogen flow rates.

The (100), (002), and (101) crystalline planes of TiZr were found in specimen N00, and the (111) and (200) plane of TiZrN were observed in specimens N06 to N25. Only one broad peak appeared in the spectra of specimens N04 and N05. This unsymmetrical peak can be deconvoluted into two peaks—TiZr (002) and TiZr (101) peaks—as shown in Figures 2 and 3. The XRD results indicate that the phase transition of films occurred as the nitrogen flow rate increased from 0 to 0.6 sccm.

The texture coefficients of films N06 to N25 were calculated from the integrated intensities of the TiZrN (111) and TiZrN (200) peaks (Table 2). The intensity of the (111) peak was stronger than that of the (200) peak; thus, the preferred orientation of specimens N06 to N25 was (111). Figure 4 shows the variation in texture coefficient with nitrogen flow

TABLE 2: Summary of the properties of films deposited at various nitrogen flow rates.

Sample numbers	Nitrogen flow rate (sccm)	Thickness (nm)	N/(Ti + Zr) ratio ( $\pm 10\%$ )	Ti/(Ti + Zr) ratio ( $\pm 10\%$ )	FWHM ( $2\theta$ ) TiZr (002) (111)	FWHM ( $2\theta$ ) TiZrN (002) (002)	Grain size (nm) TiZr (111)	Grain size (nm) TiZrN (111)	Texture coefficient	Lattice parameter (Å)
N00	0	690	0	0.41	0.89	—	9	—	—	—
N04	0.4	641	0.50	0.44	3.72	—	4	—	—	—
N05	0.5	611	0.61	0.43	1.77	—	5	—	—	—
N06	0.6	622	0.71	0.41	—	0.59	—	14	0.61	* 4.45
N07	0.7	625	0.81	0.38	—	0.46	—	18	0.61	* 4.45
N10	1	532	0.93	0.41	—	0.42	—	20	0.74	4.43
N13	1.3	413	0.96	0.40	—	0.47	—	18	0.75	4.44
N16	1.6	381	1.05	0.37	—	0.45	—	19	0.86	4.44
N19	1.9	331	0.98	0.40	—	0.48	—	17	0.89	4.44
N22	2.2	277	0.96	0.42	—	0.54	—	15	0.86	4.43
N25	2.5	240	1.03	0.40	—	0.52	—	16	0.71	4.43

\*The lattice parameters of N06 and N07 were calculated from TiZrN peaks, although those films contained two phases.

TABLE 3: Colorations, residual stresses, and hardness values of films deposited at various nitrogen flow rates.

Sample numbers	Nitrogen flow rate (sccm)	Coloration			Residual stress (GPa) (±2%)	Hardness (GPa) (±8%)	Resistivity ( $\mu\Omega\cdot\text{cm}$ )
		$L^*$	$a^*$	$b^*$			
N00	0	82.3	1.6	3.8	0.56	6	$110.9 \pm 1.18$
N04	0.4	79.1	1.7	4.2	-0.60	19	$217.9 \pm 6.14$
N05	0.5	79.7	1.9	4.4	-1.63	18	$179.9 \pm 1.39$
N06	0.6	81.2	1.6	5.4	-2.58	27	$132.6 \pm 4.32$
N07	0.7	83	1.6	8.14	-2.97	33	$78.5 \pm 1.11$
N10	1	83.7	3.3	28.6	-5.17	35	$34.8 \pm 1.73$
N13	1.3	84	3.1	28.9	-5.42	33	$35.4 \pm 0.35$
N16	1.6	84.1	3.5	29.4	-5.53	37	$35.7 \pm 0.36$
N19	1.9	83.7	3.3	29.6	-5.21	38	$37.8 \pm 0.42$
N22	2.2	82.6	4.3	30.5	-4.22	38	$38.0 \pm 0.4$
N25	2.5	82.4	4.4	30.1	-3.93	38	$39.7 \pm 0.53$

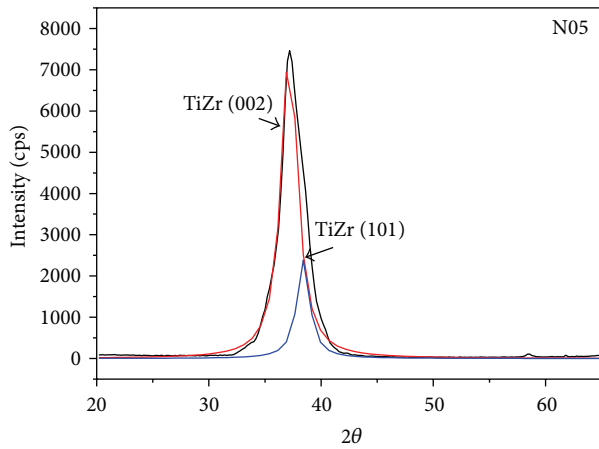


FIGURE 3: Deconvolution patterns of the N05 specimen.

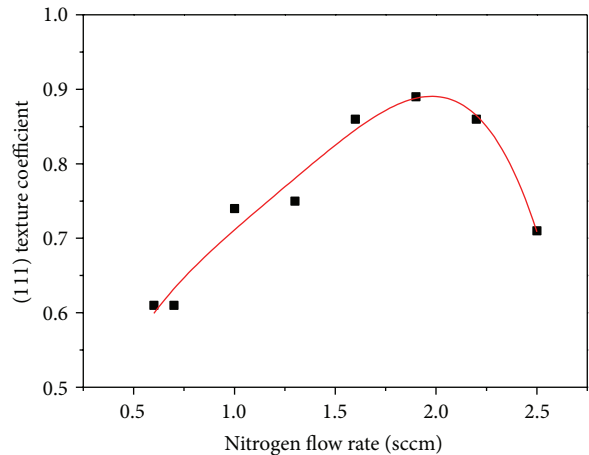


FIGURE 4: Texture coefficient of the TiZrN films with respect to nitrogen flow rate.

rate. The texture coefficient of (111) increased from 0.6 to 0.9 with increasing nitrogen flow rate from 0.6 to 1.9 sccm; as nitrogen flow rates increased from 1.9 to 2.5 sccm, the texture coefficient decreased to 0.7.

The full-width-at-half-maximum (FWHM) values of the TiZr (002) or TiZrN (111) peaks were also calculated from the XRD patterns (Table 2). The FWHM of TiZr (002) for specimen N04 was larger than that of specimen N05, indicating the better crystallinity of N05. This suggests that increasing the nitrogen flow rate can improve the crystalline quality of the TiZr phase in TiZrN films. The FWHM of specimen N06 was larger than those of the films deposited at higher nitrogen flow rates, indicating the poor crystallinity of the N06 TiZrN film.

The grain sizes of the films were obtained from the FWHM values of the TiZr (002) or TiZrN (111) peaks using the Scherrer equation (Table 2). The grain sizes of TiZr (002) in specimens N04 and N05 were less than 10 nm. The grain size of TiZrN (111) in specimen N06 was smaller than those for films deposited at higher nitrogen flow rates; for flow rates above 0.7 sccm, the average grain size was approximately 18 nm.

Figures 5(a), 5(b), 5(c), and 5(d) show the GIXRD patterns of specimens N00, N04, N05, and N06, respectively. The X-ray incident angle was 0.5°, and the 2θ angle scanned from 20° to 100°. The 2θ angles of peaks were obtained by fitting each peak on the basis of the assumption of a Gaussian or Lorentz distribution. The GIXRD patterns did not reveal additional phases that were not observed by XRD. Five major peaks of the TiZr crystalline plane, namely, (100), (101), (102), (103), and (200), were observed in the GIXRD pattern of specimen N00. The patterns of specimens N04 and N05 reveal that there were two phases in these films, that is, TiZr and TiZrN. A single TiZrN phase with five major peaks ((111), (200), (220), (311), and (222)) was observed in the spectrum of specimen N06. The GIXRD patterns of the other specimens were similar to that of N06 at nitrogen flow rates higher than 0.6 sccm.

The lattice parameter from each ( $hkl$ ) plane was calculated by the following equation:

$$a = \frac{\lambda \times \sqrt{h^2 + k^2 + l^2}}{2 \times \sin \theta} \quad (\lambda = 1.5405 \text{ \AA}) \quad (1)$$

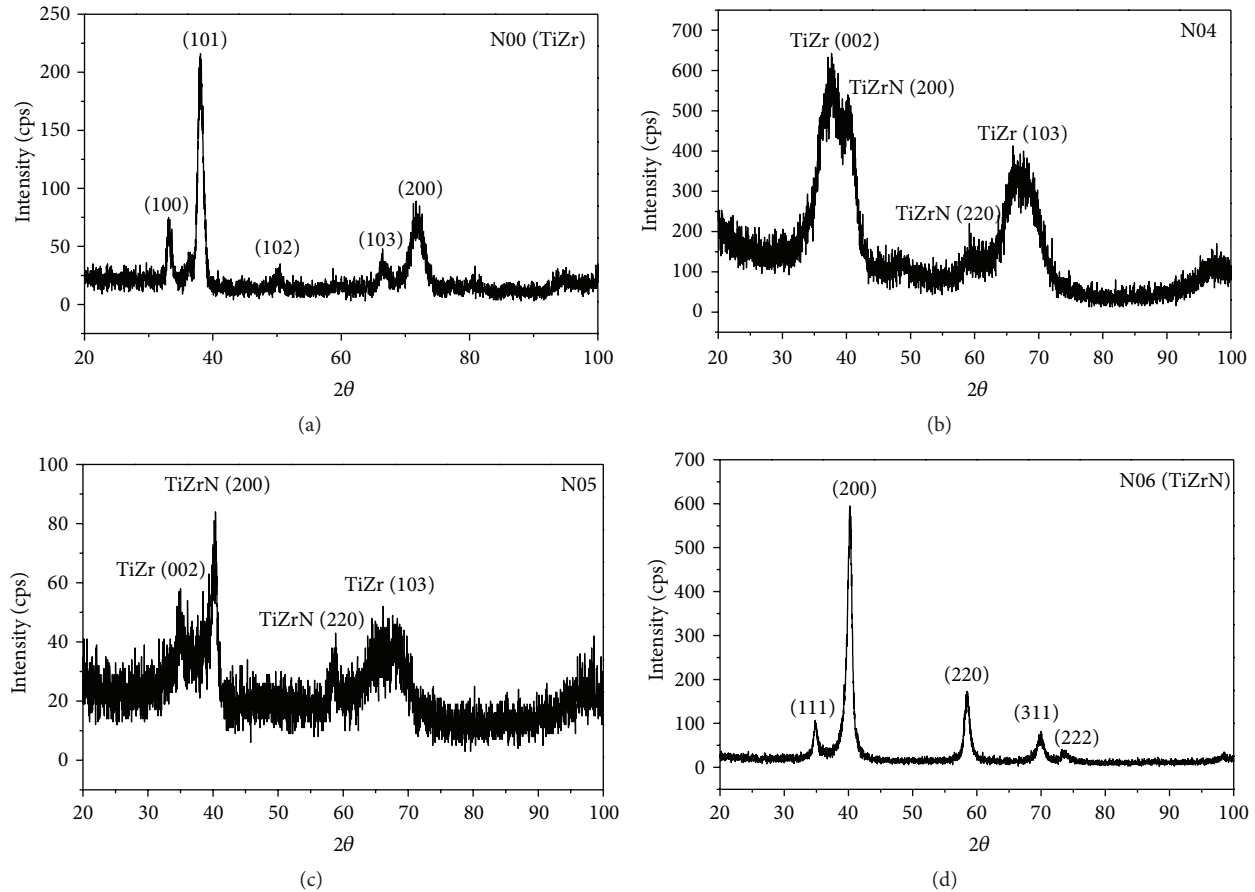


FIGURE 5: GIXRD patterns of specimens (a) N00, (b) N04, (c) N05, and (d) N06.

The lattice parameter of each peak was plotted against  $\cos \theta / \sin \theta$  and linearly fitted. The lattice parameter ( $a_0$ ) was obtained from extrapolation to  $\theta = 90^\circ$  (Table 2). The lattice parameters of specimens N04 and N05 are not listed since there was just one or two diffraction peaks of each phase in the XRD patterns of these mixed-phase films, which is insufficient for meaningful linear regression. The lattice parameters of films deposited at nitrogen flow rates from 1.0 to 2.5 sccm ranged from 4.43 to 4.44 Å with an error below 0.4%. The lattice parameters were not significantly influenced by the nitrogen flow rate.

Figure 6 shows the cross-sectional SEM images of the samples deposited at different nitrogen flow rates. Although the columnar structure was not evident in the sample deposited at a nitrogen flow rate of 0.4 sccm, this structure became more evident with increasing flow rate.

The thicknesses of the TiZrN films ranged from 240 to 690 nm, which decreased with increasing nitrogen flow rate at a constant deposition time of 40 min. The deposition rate was calculated as the thickness divided by the deposition time. The variation in deposition rate with nitrogen flow rate is shown in Figure 7. The deposition rate decreased with increasing nitrogen flow rate, which was likely due to the decrease in the supply of Ti and Zr atoms with increasing nitrogen flow rate, thereby reducing the deposition rate.

Figures 8 and 9 show the deconvoluted XPS Zr-3d and Ti-2p spectra for samples N19 and N04, respectively.

The contents of Ti, Zr, N, and O were calculated from the integrated intensities of the deconvolution XPS spectra. The bonding of TiN, TiNO, TiO<sub>2</sub>, ZrN, ZrNO, and ZrO<sub>2</sub> may have existed in the TiZrN thin films deposited at nitrogen flow rates exceeding 0.7 sccm. When the nitrogen flow rate was less than 0.7 sccm, Ti-Ti and Zr-Zr metal bonds were present in the TiZrN films.

The N/(Ti + Zr) and Ti/(Ti + Zr) ratios were calculated from the integrated areas of each element divided by their sensitive factors (Table 2). All of the Ti/(Ti + Zr) ratios were approximately 0.4. The variation in N/(Ti + Zr) ratio with nitrogen flow rate is shown in Figure 10. The N/(Ti + Zr) ratio increased from 0.6 to 1 as nitrogen flow rate increased from 0.6 to 1.3 sccm and then leveled off at 1 when nitrogen flow rate increased further. According to the binary phase diagram, the N/Ti ratio of the TiN ranged from 0.6 to 1.2 [6], whereas the N/Zr ratio of the ZrN phase ranged from 0.8 to 1.1 [7]. A low N/(Ti + Zr) ratio indicates that the content of nitrogen atoms is insufficient to form a single TiZrN phase; hence, the films with low N/(Ti + Zr) ratios contained both TiZr and TiZrN or TiN and ZrN phases. The GIXRD results also support this argument.

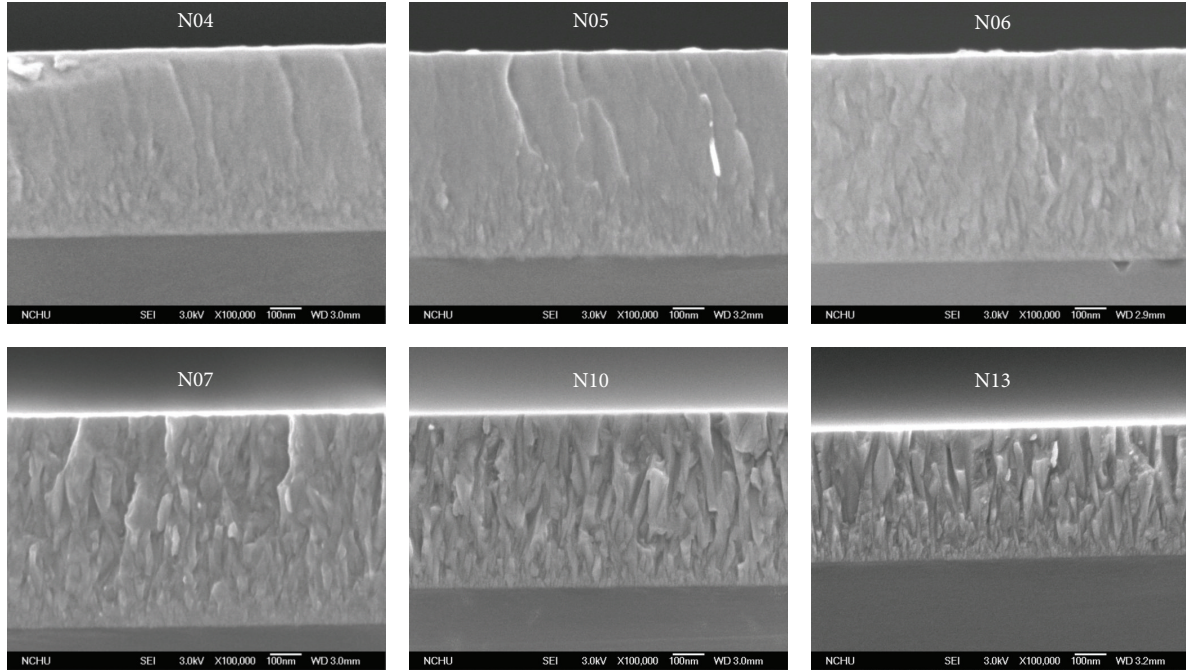


FIGURE 6: Cross-sectional SEM images of the TiZrN films.

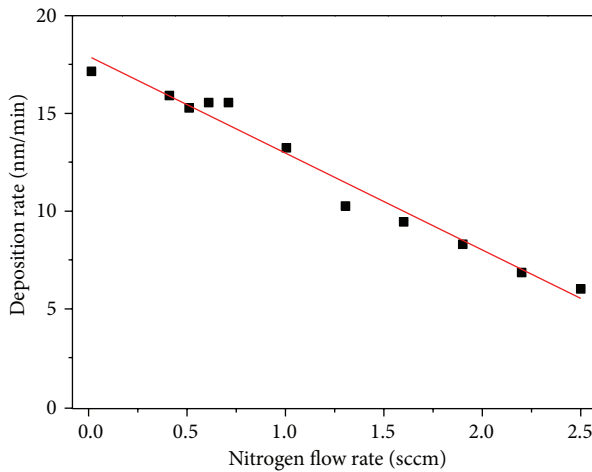


FIGURE 7: Deposition rate as a function of nitrogen flow rate.

The colorations of all samples determined by spectrophotometry are shown in Figure 11. The samples deposited at nitrogen flow rates less than 1 sccm were gray in color, whereas the samples containing higher nitrogen contents exhibited gold coloration. Note that the N06 and N07 specimens were gray, but only TiZrN peaks were observed in their XRD patterns. This indicates that another phase may have existed in the N06 and N07 specimens.

The average values of  $L^*a^*b^*$  located on the color coordinate in the CIELAB 1976 coloration space are listed in Table 3. The relationship between  $L^*a^*b^*$  and  $N_2$  flow rate is shown in Figure 12. Among the gold-colored samples, the colorations of samples N22 and N25 were slightly different from those of the others. The  $a^*$  value, which represents the

level of red color, increased with increasing nitrogen flow rate. The  $L^*$  value represents the brightness of the film. The  $L^*$  values of samples N22 and N25 were smaller than those of the other gold-colored samples, whereas the  $a^*$  values of these samples were larger. These results indicate that the colorations of samples N22 and N25 were darker gold compared to the other samples.

According to abovementioned results, those specimens can be divided into three zones based on the XRD patterns. Zone 1 is the film with a single TiZr phase at a nitrogen flow rate of 0 sccm. Zone 2 is the mixed-phase film; the nitrogen flow rate range of zone 2 was 0.4 to 0.7 sccm. Zone 3 is the film containing only the TiZrN phase (nitrogen flow rate > 0.7 sccm).

The residual stresses of the TiZrN films were determined using an optical method (Table 3). Tensile stress was observed only in sample N00, whose XRD pattern exhibited TiZr peaks, whereas compressive stress was found in all other films. Figure 13 shows the variation in residual stress with nitrogen flow rate. The compressive stress initially increased with increasing  $N_2$  flow rate in zone 2. In zone 3, the stress stabilized as nitrogen flow rate further increased and decreased when nitrogen flow rate exceeded 1.9 sccm.

Figure 14 shows the variation in electrical resistivity with nitrogen flow rate. The resistivity rapidly increased to  $217.9 \mu\Omega\cdot\text{cm}$  as nitrogen flow rate increased from 0 to 0.4 sccm. In zone 2, the resistivity decreased to  $34.8 \mu\Omega\cdot\text{cm}$  with increasing nitrogen flow rate. The resistivity was not significantly influenced by nitrogen flow rate in zone 3, and the average resistivity was approximately  $35 \mu\Omega\cdot\text{cm}$ .

The hardness values of the TiZrN films were measured using a nanoindenter. Figure 15 shows the variation in hardness with nitrogen flow rate. In zone 2, the hardness

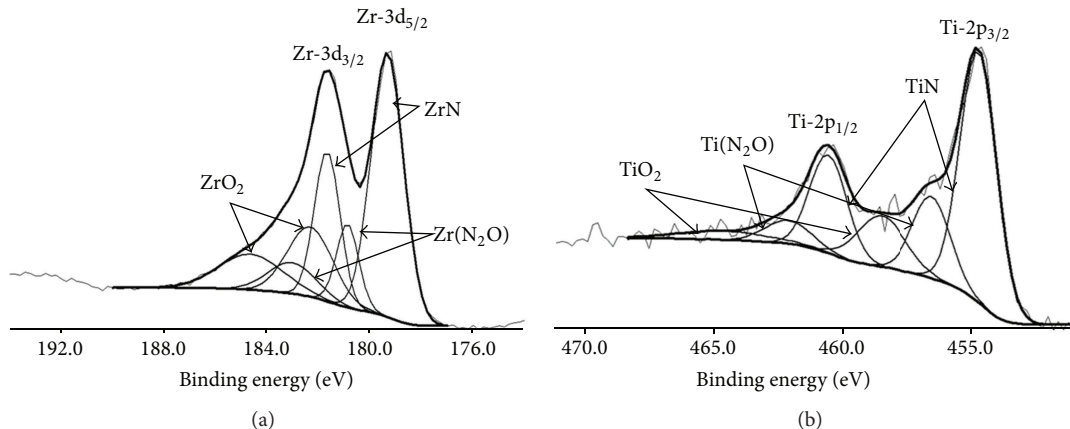


FIGURE 8: Deconvolution spectra of samples deposited at a nitrogen flow rate of 1.9 sccm: (a) Zr-3d and (b) Ti-2p peaks.

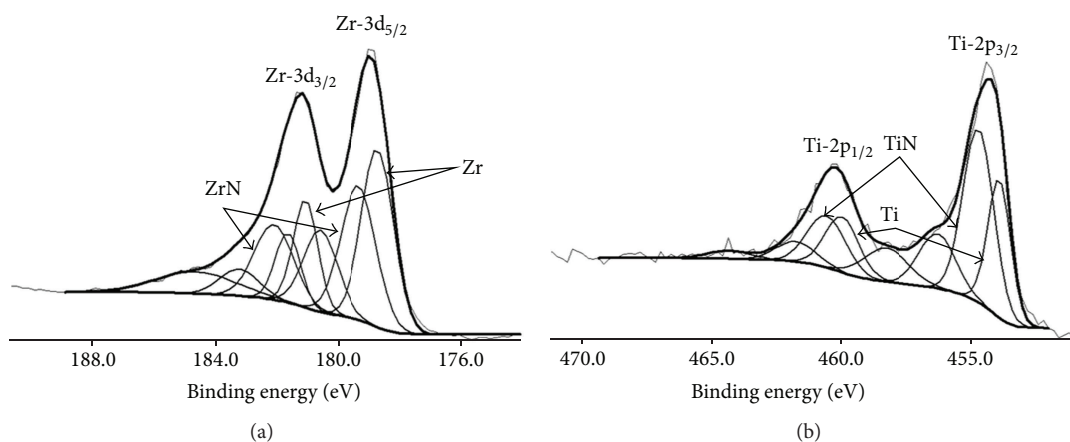


FIGURE 9: Deconvolution spectra of sample N06: (a) Zr-3d and (b) Ti-2p.

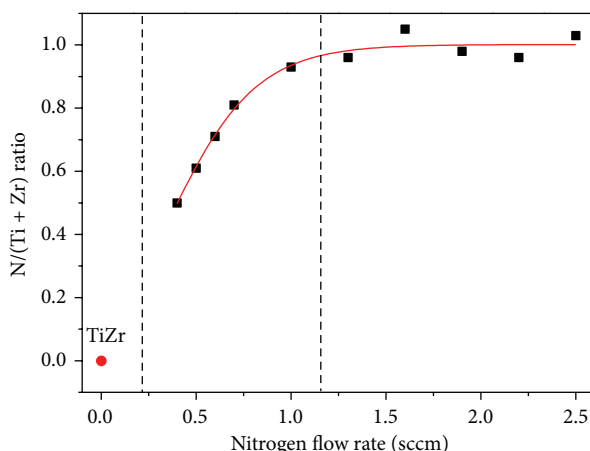


FIGURE 10: Variation in N/(Ti + Zr) with nitrogen flow rate.

increased from 15 to 33 GPa with increasing nitrogen flow rate. In zone 3, the variation in hardness with nitrogen flow rate was not evident, and the average hardness was approximately 36 GPa.

Note that the hardness of the N07 specimen was similar to that of the TiZrN film; however, the N07 specimen was gray in color.

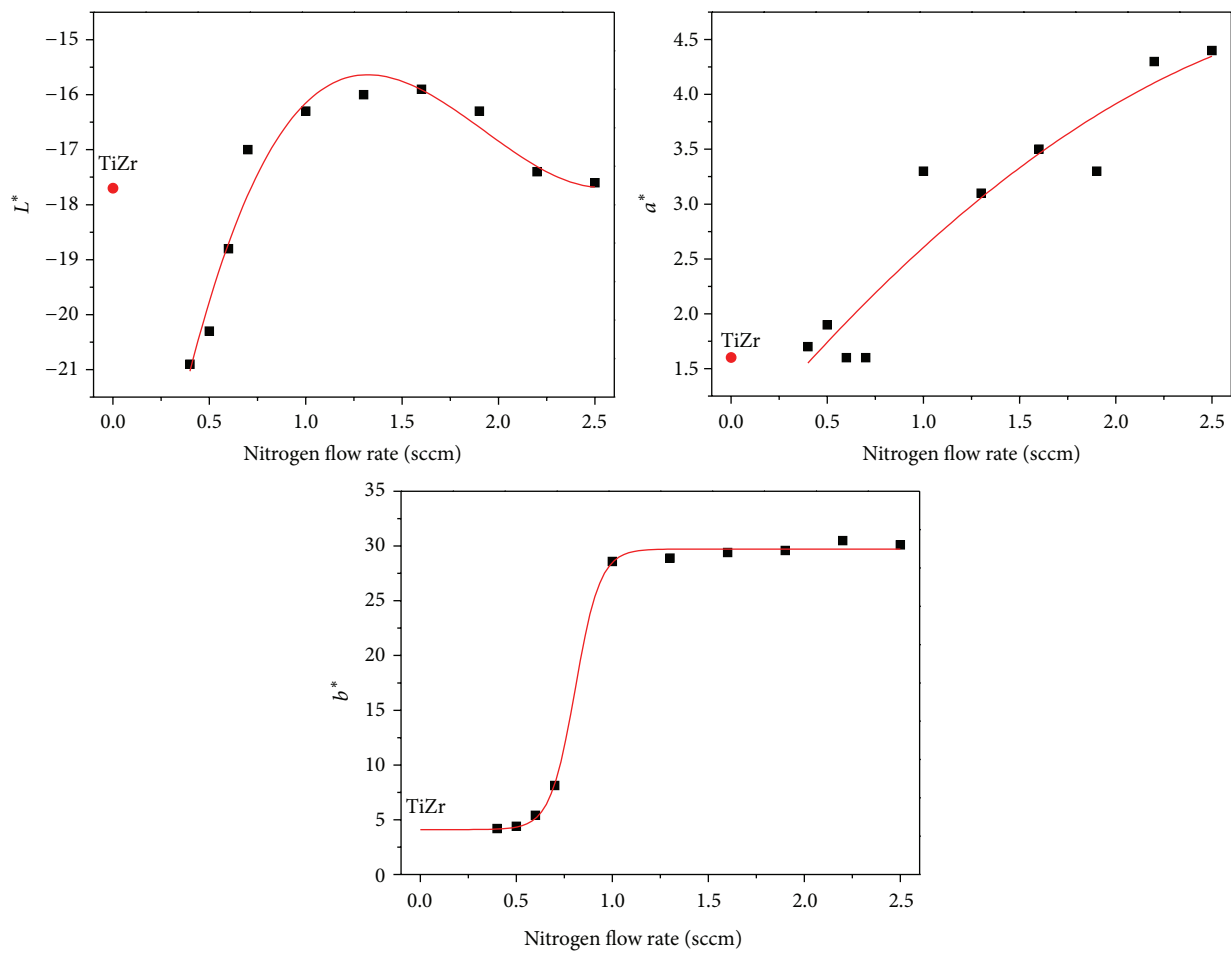
#### 4. Discussion

**4.1. Nanocomposite.** As shown in Figure 1, the XRD peak of TiZr was observed only in specimens N04 and N05 herein; this was not observed in the patterns of specimens N06 and N07. However, the colors of the N04, N05, N06, and N07 films were similar, indicating that the TiZr grains may have been embedded in the TiZrN matrix in specimens N06 and N07. The second phase of TiZr may have been an amorphous phase in N06 and N07; the amorphous phase would not have been found by XRD and GIXRD. Furthermore, the XPS Ti- $2p_{3/2}$  and Zr- $3d_{5/2}$  deconvolution spectra (Figure 8) indicated that pure Ti and Zr metal bonds existed in specimen N06, further supporting the idea that TiZr was present in the films. According to the phases of TiZrN thin films, the films can be separated into three zones:

- (1) Single phase with HCP structure TiZr; N/(Ti + Zr) = 0 (sample N00).



FIGURE 11: Coloration of all samples used in this study.

FIGURE 12: Variation in the  $L^*$ ,  $a^*$ ,  $b^*$  value with nitrogen flow rate.

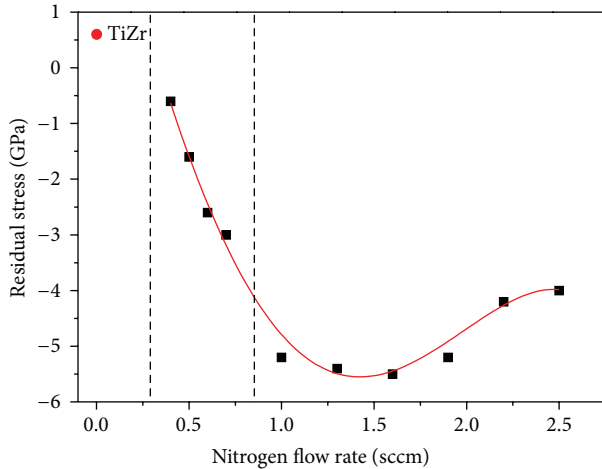


FIGURE 13: Residual stress of TiZrN films as a function of nitrogen flow rate.

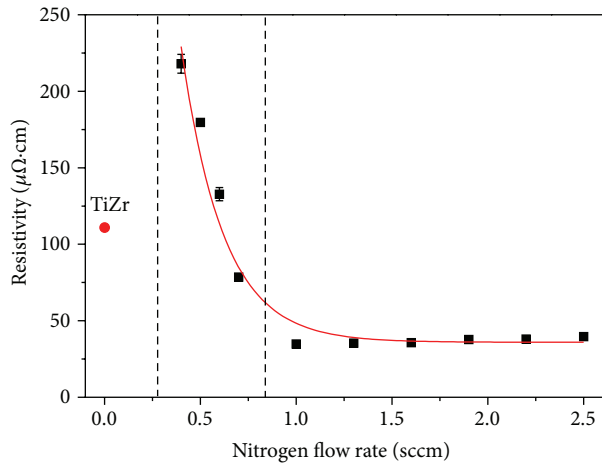


FIGURE 14: TiZrN resistivity as a function of nitrogen flow rate.

- (2) Multiphase with HCP structure TiZr, FCC structure TiZrN, and other uncertain phases;  $N/(Ti + Zr) < 0.9$  (samples N04 to N07).
- (3) Single phase with FCC structure TiZrN;  $N/(Ti + Zr) > 0.9$  (samples N10 to N25).

On the basis of this classification scheme, it can be found that the multiphase appeared in the (Ti, Zr)N as the  $N/(Ti + Zr)$  was less than 0.9 on one hand. On the other hand, the  $N/(Ti + Zr)$  ratio of the stable TiZrN must have been larger than 0.9. The stable composition of (Ti, Zr)N should consider the contribution of TiN and ZrN phases. Based on the N-Ti and N-Zr phase diagrams [6, 7], the N/Ti composition range of TiN is 0.6–1.2 and the N/Zr composition range of ZrN is 0.8–1.1. In the (Ti, Zr)N system, the addition of Zr to TiN (or the addition of Ti to ZrN) causes the lattice strain and destroys the stable structure. This lattice strain affects the extent of nitrogen solvation in the solid solution of (Ti, Zr)N; thus, the extent of solvation of the stable (Ti, Zr)N films is lesser than those of TiN and ZrN. The  $N/(Ti + Zr)$  ratio of

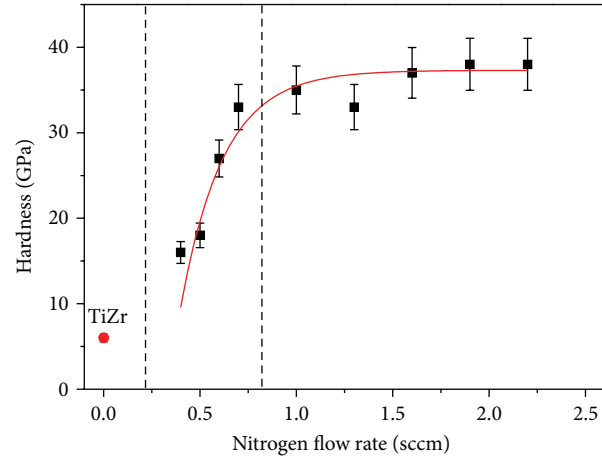


FIGURE 15: TiZrN film hardness as a function of nitrogen flow rate.

stable (Ti, Zr)N is between 0.8 and 1.1. Nitrogen content of plays an important role in the phase transition. At nitrogen flow rates less than 0.7 sccm, the  $N/(Ti + Zr)$  values of the TiZrN films were less than 0.9, and there were insufficient nitrogen atoms to bond with the Ti and Zr atoms that arrived at the substrate surface; the excess Ti and Zr atoms formed the metallic TiZr phase. Thus, the TiZrN film with low  $N/(Ti + Zr)$  ratio was basically composed of TiZrN and TiZr with a nanocomposite structure. In a previous study, the secondary phase TiZr appeared in TiZrN films with low  $N/(Ti + Zr)$  ratios [8].

**4.2. Hardness.** As shown in Figure 15, the hardness of TiZr film was the lowest among all samples, and that of TiZrN films increased with nitrogen flow rate until 0.7 sccm; above this value, the hardness leveled off at approximately 36 GPa. Many factors might affect film hardness, such as preferred orientation, grain size, stoichiometry, and residual stress.

Several studies have reported that the (111) texture coefficient is an important factor affecting the hardness of TiN films because  $\langle 111 \rangle$  is the hardest orientation in TiN [9, 10]. Since the Schmid factor for the (111) direction of TiN is zero in all slip systems, hardness increases with increasing (111) texture coefficient. TiZrN has the same NaCl crystal structure as TiN, (111), which is supposed to be the hardest orientation of the TiZrN film. However, the effect of the (111) texture coefficient on the hardness of the TiZrN film was not significant herein.

In this study, the relationship between grain size and hardness was insignificant. At low nitrogen flow rate, both crystalline and amorphous phases may have formed in the film. Therefore, it was difficult to determine whether the grain size affected film hardness since grain size was measured from XRD patterns, reflecting only crystalline phases.

Differences in composition can significantly affect film hardness. Among the films used herein, the film containing only the metallic TiZr phase, which was deposited without nitrogen, had the lowest hardness. The hardness values of metallic materials are generally lower than those of ceramic materials because ionic and covalent bonds are stronger than

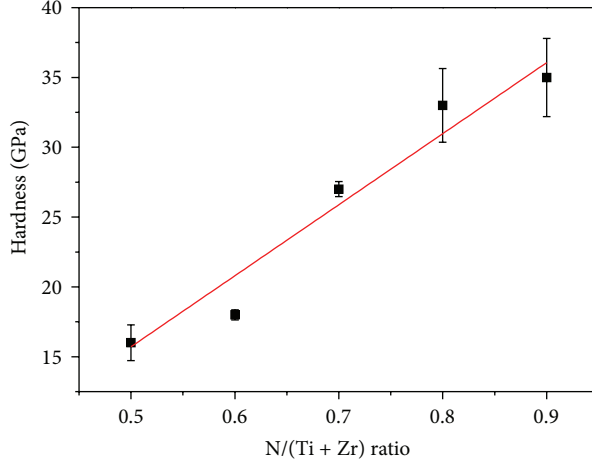


FIGURE 16: Hardness values of TiZrN films (N04–N10) with respect to N/(Ti + Zr) ratio.

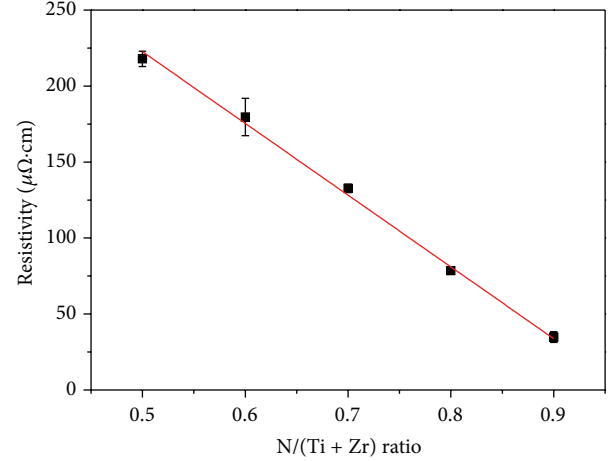


FIGURE 17: TiZrN film (N04–N10) resistivity with respect to the N/(Ti + Zr) ratio.

metallic bonds. Therefore, the hardness of the TiZr film was lower than that of the TiZrN film. The hardness values of TiZrN films were higher than those of TiN and ZrN due to solid-solution hardening. The addition of Zr to TiN (Ti to ZrN) induced the lattice distortion of the matrix; hence, it is necessary to apply more force for dislocation slip. Moreover, film hardness is related to the fraction of the TiZrN phase. When nitrogen atoms are introduced during the deposition process, the nitrogen atoms combine with Ti and Zr atoms to form the TiZrN phase in the films. In a previous study, the lattice parameter was found to be proportional to the atomic fraction  $x$  in  $\text{Ti}_{1-x}\text{Zr}_x\text{N}$  [11]. The lattice parameters of the TiZrN films used herein were almost identical, even for the films deposited at low nitrogen flow rates of 0.6 and 0.7 sccm. This result indicates that the compositions of the TiZrN phases in the films were identical. In this case, the overall compositional change comes from the surrounding TiZr phase. Therefore, we can assume that the increase in N/(Ti + Zr) ratio is equivalent to increase in the TiZrN fraction. As the nitrogen flow rate increased, more nitrogen atoms bonded with Ti and Zr atoms to form the high-hardness TiZrN phase. In other words, the N/(Ti + Zr) ratio increased with increasing nitrogen flow rate from 0.4 to 1.0 sccm, and the TiZrN film hardness increased with increasing TiZrN fraction (Figure 16).

In zone 3, the N/(Ti + Zr) ratios of the TiZrN films were larger than 0.8 and were with stable nitrogen flow rate; thus, the TiZrN film hardness did not vary with nitrogen flow rate. The averaged hardness was approximately 36 GPa at high nitrogen flow rates ranging from 1.0 to 2.5 sccm. Notably, although the N/Zr ratio was below 0.9 in specimen N07 with a nanocomposite structure, its high hardness was similar to that of the TiZrN film. It is possible that the structure of specimen N07 was composed of uniform composite phases.

**4.3. Resistivity.** The resistivity of TiZr is approximately  $126 \mu\Omega\cdot\text{cm}$ . TiZrN can be used as a diffusion barrier due to its low resistivity ( $60\text{--}100 \mu\Omega\cdot\text{cm}$ ) [12, 13].

Resistivity depends on lattice defects and impurity atoms in the film; increases in lattice defects and impurity atoms increase the scattering of conductive free electrons and decrease the mean free path of conductive free electrons. Thus, more lattice defects and impurity atoms may increase the resistivity. Herein, the resistivities of the nanocomposite films deposited at low nitrogen flow rates (0.4 to 0.7 sccm) are higher than those of the single-phase TiZr and TiZrN films (Figure 14). This may indicate that more lattice defects and impurity atoms were present at the TiZr/TiZrN interfaces in the nanocomposite films, resulting in higher resistivities compared to the single-phase films. The FWHM from XRD patterns represents the crystallinity of the crystal plane in the films, and the FWHM of each specimen was calculated from different peaks. Therefore, we could not confirm if the crystallinity was related to TiZrN film resistivity.

The TiZrN film resistivity decreased with increasing nitrogen flow rate to 0.9 sccm (Figure 14). TiZrN resistivity may have depended upon of N/(Ti + Zr), as shown in Figure 17. The films deposited at low nitrogen flow rates (0.4 to 0.7 sccm) exhibited nanocomposite structures; hence, the resistivities of these films were higher than those of the films deposited at high nitrogen flow rates. The fraction of TiZrN phase was also related to TiZrN film resistivity. As nitrogen flow rate increased from 0.4 to 1.0 sccm, the N/(Ti + Zr) ratio increased accordingly, and the structures of TiZrN films became uniform. Therefore, the resistivity decreased with increasing N/(Ti + Zr) ratio at low nitrogen flow rate. The lowest TiZrN film resistivity values were observed at nitrogen flow rates above 1.0 sccm, which may be attributed to the single-phase TiZrN film.

Comparing the results of a previous study with those herein indicates that low resistivity and high hardness can be obtained at high nitrogen flow rates. This may be due to the high crystallinity of the TiZrN structure.

**4.4. Residual Stress.** The residual stress in the TiZr film was tensile stress, whereas compressive stress was observed

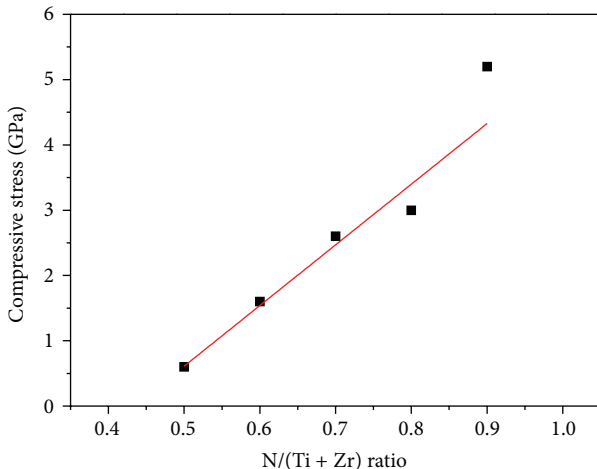


FIGURE 18: Residual stress of the TiZrN films (N04–N10) as a function of N/(Ti + Zr).

in TiZrN films. Residual stress comes from thermal stress and grown-in stress. Herein, the major contribution was grown-in stress. Substrate temperature, gas pressure, and substrate bias are known to be the main parameters affecting grown-in stress. Herein, the substrate temperature and bias were fixed at 400°C and –80 V, respectively. There was an evident relationship between the residual stress of TiZrN and nitrogen flow rate.

Figure 13 shows that the compressive stress of the TiZrN films decreased with increasing nitrogen flow rate from 0.4 to 1.0 sccm. The N/(Ti + Zr) ratio increased as the nitrogen flow rate increased, whereas the residual stress decreased because the stress was released with the appearance of the TiZr phase. Therefore, the fraction of TiZr phase in the films decreased with increasing N/(Ti + Zr) ratio, and the compressive stress in the film consequently increased. As shown in Figure 18, the compressive stress increased with increasing N/(Ti + Zr) ratio for the films deposited at nitrogen flow rates ranging from 0.4 to 1.0 sccm.

The residual stress in the TiZrN films increased to –5 GPa as nitrogen flow rate increased to 1.0 sccm and then stabilized. However, the residual stress decreased as nitrogen flow rate increased from 0.22 to 0.25 sccm. There was no significant relationship between residual stress and any structural properties.

## 5. Conclusions

- (1) Nanocrystalline TiZrN thin films were successfully prepared by DC unbalanced magnetron sputtering with different nitrogen flow rates ranging from 1.0 to 2.5 sccm. The hardness and resistivity stabilized when nitrogen flow rate increased above 1.0 sccm.
- (2) According to the phases of the TiZrN thin films, three zones were defined. The film exhibited a single phase with TiZr HCP structure at nitrogen flow rate of zero. As the nitrogen flow rate increased from 0.4 to 0.7 sccm, the films were two-phase with TiZr of

HCP structure and TiZrN of NaCl structure. When nitrogen flow rate was higher than 1.0 sccm, the films were single-phase with TiZrN of NaCl structure.

- (3) The N/(Ti + Zr) ratio of the TiZrN single-phase film must be larger than 0.8, and the N/(Ti + Zr) ratio did not change with nitrogen flow rate when the flow rate exceeded 1.0 sccm.
- (4) The hardness and residual stress of the TiZrN films increased with increasing N/(Ti + Zr) ratio when the nitrogen flow rate increased from 0.4 to 1.0 sccm. In contrast, the resistivity of the TiZrN films decreased with increasing N/(Ti + Zr) ratio.

## Conflict of Interests

The authors declare that there is no conflict of interests regarding the publication of this paper.

## References

- [1] A. S. Korhonen, J. M. Molarius, I. Penttinen, and E. Harju, “Hard transition metal nitride films deposited by triode ion plating,” *Materials Science and Engineering*, vol. 105–106, no. 2, pp. 497–501, 1988.
- [2] L. P. Ward, K. N. Strafford, C. Subramanian, and T. P. Wilks, “Observations on the structure, hardness and adhesion properties of a selection of multicomponent refractory element nitride coatings,” *Journal of Materials Processing Technology*, vol. 56, no. 1–4, pp. 375–384, 1996.
- [3] L. A. Donohue, J. Cawley, and J. S. Brooks, “Deposition and characterisation of arc-bond sputter Ti<sub>x</sub>Zr<sub>y</sub>N coatings from pure metallic and segmented targets,” *Surface and Coatings Technology*, vol. 72, no. 1–2, pp. 128–138, 1995.
- [4] V. V. Uglov, V. M. Anishchik, V. V. Khodasevich et al., “Structural characterization and mechanical properties of Ti-Zr-N coatings, deposited by vacuum arc,” *Surface and Coatings Technology*, vol. 180–181, pp. 519–525, 2004.
- [5] P. J. Kelly and R. D. Arnell, “Magnetron sputtering: a review of recent developments and applications,” *Vacuum*, vol. 56, no. 3, pp. 159–172, 2000.
- [6] H. A. Wriedt and J. L. Murray, “The N-Ti (Nitrogen-Titanium) system,” *Bulletin of Alloy Phase Diagrams*, vol. 8, no. 4, pp. 378–388, 1987.
- [7] H. Okamoto, “N-Zr (Nitrogen-Zirconium),” *Journal of Phase Equilibria and Diffusion*, vol. 27, no. 5, p. 551, 2006.
- [8] Y.-W. Lin, J.-H. Huang, and G.-P. Yu, “Microstructure and corrosion resistance of nanocrystalline TiZrN films on AISI 304 stainless steel substrate,” *Journal of Vacuum Science and Technology A*, vol. 28, article 774, 2010.
- [9] H. Ljungcrantz, M. Odén, L. Hultman, J. E. Greene, and J.-E. Sundgren, “Nanoindentation studies of single-crystal (001)-, (011)-, and (111)-oriented TiN layers on MgO,” *Journal of Applied Physics*, vol. 80, no. 12, pp. 6725–6733, 1996.
- [10] W.-J. Chou, G.-P. Yu, and J.-H. Huang, “Deposition of TiN thin films on Si(100) by HCD ion plating,” *Surface and Coatings Technology*, vol. 140, no. 3, pp. 206–214, 2001.
- [11] Q. Y. Chen, *Characterization of structure and mechanical properties of nano-crystalline TiZrN films deposited by unbalanced magnetron sputtering: the effect of Ti and Zr target current [M.S. thesis]*, National Tsing Hua University, Hsinchu, Taiwan, 2012.

- [12] C. Lee and Y.-L. Kuo, "The evolution of diffusion barriers in copper metallization," *JOM*, vol. 59, no. 1, pp. 44–49, 2007.
- [13] Y. L. Kuo, F. C. Kung, and T. L. Su, "Superior stability of ultrathin and nanocrystalline TiZrN films as diffusion barriers for Cu metallization," *Nanoscience and Nanotechnology Letters*, vol. 1, no. 1, pp. 37–41, 2009.